INVESTIGATION OF NO_2 AND SO_2 ADSORPTION/DESORPTION PROPERTIES OF ADVANCED TERNARY AND QUATERNARY MIXED OXIDES FOR DENO$_X$ CATALYSIS

A DISSERTATION SUBMITTED TO

THE GRADUATE SCHOOL OF ENGINEERING AND SCIENCE

OF BILKENT UNIVERSITY

IN PARTIAL FULFILLMENT OF THE REQUIREMENTS FOR

THE DEGREE OF

DOCTOR OF PHILOSOPHY

IN CHEMISTRY

By

ZAFER SAY

November, 2015

INVESTIGATION OF NO_2 AND SO_2 ADSORPTION/DESORPTION PROPERTIES OF ADVANCED TERNARY AND QUATERNARY MIXED OXIDES FOR $DENO_X$ CATALYSIS

By Zafer Say

November, 2015

We certify that we have read this dissertation and that in my opinion is it is fully adequate, in scope and quality, as a dissertation of the degree of Doctor of Philosophy.

_____

Prof. Dr. Ömer Dağ

_____

Prof. Dr. Timur Doğu

_____

Asst. Prof. Dr. Ferdi Karadaş

_____

Prof. Dr. Saim Özkar

_____

Assoc. Prof. Dr. Emrah Özensoy (Advisor)

Approved for the Graduate School of Engineering and Science:

_____

Prof. Dr. Levent Onural

Director of the Graduate School

ABSTRACT

INVESTIGATION OF NO_2 AND SO_2 ADSORPTION/DESORPTION PROPERTIES OF ADVANCED TERNARY AND QUATERNARY MIXED OXIDES FOR $DENO_X$ CATALYSIS

ZAFER SAY

Doctor of Philosophy in Chemistry
Supervisor: Assoc. Prof. Dr. Emrah Özensoy
November, 2015

The main premise of the current study is the design, synthesis and functional characterization of novel catalytic materials with superior resistance against sulfur poisoning without compromising NO_x storage capacity (NSC) in their NO_x Storage Reduction (NSR) catalytic applications. BaO/TiO_2-based materials are well known systems in $deNO_x$ catalysis, exhibiting promising performance towards sulfur poisoning. However, they suffer from limitations due to poor NSC and high affinity towards unwanted solid state interactionsbetweenTiO_2 and BaO storage domains leading to the formation of $BaTiO_x$.The main emphasis of the current work is the design of a novel catalytic system where ZrO_2 and Al_2O_3 act as diffusion barriers between BaO and TiO_2 domains while allowing good dispersion and preservation of the individual characteristicsof these active sites within a wide operational temperature window. Along these lines, binary and ternary mixed oxide materials, ZrO_2/TiO_2 (ZT) and $Al_2O_3/ZrO_2/TiO_2$ (AZT), and their Pt, BaO and/or K_2O

functionalized counterparts in the form of Pt/ZT, Pt/AZT, Pt/BaO/AZT, Pt/K_2O/AZT and Pt/K_2O-BaO/AZT with different mass loadings (i.e. 8 and 20 wt. % 20 BaO and 2.7, 5.4 and 10 wt. % K_2O) were synthesized via sol-gel synthesis.

Surface structure and catalytic properties of the synthesized materials were comprehensively investigated at the molecular level as a function of calcination temperature, catalyst composition, nature of the gas phase adsorbates (e.g. NO_2, SO_2, O_2, H_2, N_2, N_2O C_5H_5N *etc.*) interacting with the catalyst surface at various operational temperatures by means of XRD, Raman spectroscopy, BET analysis, *in-situ* FTIR and TPD. Current results indicate no evidence for the formation of undesired $BaTiO_x$ and/or $KTiO_x$. NSC of fresh monolithic catalysts was also quantitatively measured under realistic operational conditions in a tubular flow reactor system. These flow reactor measurements indicated that Pt/8BaO/AZT and Pt/20BaO/AZT materials revealed promising NO_x storage and sulfur regeneration performance at low (*i.e.* 473 K) and moderate (*i.e.* 573 K) temperatures in comparison to the conventional Pt/20Ba/Al_2O_3 benchmark catalyst. However, they were found to be surpassed by the conventional Pt/20BaO/Al_2O_3 benchmark catalyst at higher operational temperatures (*i.e.* 673 K). Therefore, activity loss at high temperatures was alleviated by incorporating a high-temperature storage functionality (*i.e.* K_2O) to the catalyst structure. Upon this structural enhancement, Pt/5.4K_2O/AZT catalyst was found to reveal much higher NSC at high temperatures (*i.e.* 673 K) as compared to BaO-based materials. An overall assessment of the results presented in the current study suggests that there exists a delicate trade-off between NO_x Storage Capacity (NSC) and sulfur uptake/poisoning in NSR systems

which is strongly governed by the BaO and K_2O loading/dispersion as well as the surface structure of the support material.

Keywords: NSR/LNT, $Al_2O_3/ZrO_2/TiO_2$, Pt, NO_x, SO_x, NSC, FTIR, TPD

ÖZET

SO_2 VE NO_2 MOLEKÜLLERİNİN $DENO_x$ KATALIZÖRÜ OLARAK KULLANILAN ÜÇLÜ VE DÖRTLÜ KARMAŞIK OKSİT YAPILAR ÜZERİNDEKİ EMİLİM VE SALINIM ÖZELLİKLERİNİN İNCELENMESİ

ZAFER SAY

Kimya, Doktora
Danışman: Doç.Dr. Emrah Özensoy
October, 2015

Bu çalışmanın temel amacı, NOx Depolama ve İndirgeme (NDI) uygulamalarında kullanılmak üzere sülfür zehirlenmesine dayanıklı yeni nesil katalizörler sentezlemek ve bu katalizörlerin focksiyonel ve karakteristik özelliklerini incelemektir. TiO_2-temelli malzemeler, sülfüre karşı göstermiş oldukları üstün direnç ile NDI katalizör literatüründe hatırı sayılır bir yere sahiptir. Fakat, bu özelliğine istinaden NO_x depolama görevini yeteri kadar yerine getirememekle birlikte, BaO (NO_x depolayıcı oksidik yapı) ile kuvvetli bir etkileşime girerek, yapıda bulunmasını istemediğimiz düşük yüzey alana sahip $BaTiO_x$ gibi türler oluşturmaktadır. Bu çalışmanın genelinde vurgulamak istenen nokta, BaO ve TiO_2 arasındaki etkileşimi engelleyecek yeni bir katalitik malzeme sentezi ve bu amaçla ZrO_2 ve Al_2O_3 oksitlerini iki taraf arasında bir set olarak kullanıp, geniş bir sıcaklık aralığında aktif bir katalizör ortaya konulmaktadır. Bu amaçlar doğrultusunda, ikili ve üçlü metal oksit malzemeler, ZrO_2/TiO_2 (ZT) ve $Al_2O_3/ZrO_2/TiO_2$(AZT), sol-gel yöntemi ile

sentezlendi ve bu yapılar daha sonra ıslak emdirme yöntemi ile kütlece farklı oranlarda Pt, BaO ve K_2O (%1 Pt; % 8 ve 20 BaO; %2.7, 5.4 ve 10.0 K_2O) ile zenginleştirilerek; Pt/ZT, Pt/AZT, Pt/BaO/AZT, Pt/K_2O/AZT ve Pt/BaO-K_2O/AZT katalizörleri elde edildi.

Sentezlenen bütün taban/altaş/destek malzemeleri ve NO_x Depolama İndirgeme (NDİ) katalizörlerinin yüzey yapıları, katalitik özellikleri ve farklı gaz türlerinin yüzeye bağlanma geometrileri, sıcaklığa ve malzemelerin kompozisyonlarına bağlı olarak XRD, Raman specktroskopisi, BET, TPD ve Infrared Specktoskopisi yöntemleri ile detaylı ve sistematik bir şekilde incelendi. Elde ettiğimiz sonuçlar doğrultusunda, TiO_2 içeren katalizörlerin bünyesinde $BaTiO_x$ ve/veya $KTiO_x$ türü istenmeyen yapılar gözlenmemiştir.Son olarak, gerçekçi operasyonel şartlara benzer ortamlarda ve akış reaktörleri kullanılarak, mevcut çalışma kapsamında sentezlenen katalizörlerin, NO_x depolama kapasitelerinin nicel analizi gerçekleştirilmiştir. Bu ölçümlerde elde edilen sonuçlar, Pt/8BaO/AZT, Pt/20BaO/AZT ve Pt/5.4K_2O/AZT katalizörlerinin 473 ve 573 K' de, referans katalizör olarak kullanılan Pt/20BaO/Al'dan fazla NO_x depolama kapasitesine sahip olduğunu göstermektedir. Spektroskopik ölçümler, sentezlenen yeni nesil katalizörlerin sülfüre karşı gösterdikleri direncin de ticari katalizörden çok daha yüksek olduğu gerçeğini ortaya koymaktadır.Bu çalışmalar, NO_x depolama kapasitesi ve sülfür direnci arasında ince bir dengenin varlığına işaret etmektedir.Bu dengenin, katalizör yapısında mevcut bulunan BaO ve K_2O miktarları ve bu türlerin yüzey dağılımı ile yakından ilgili olduğu görülmektedir.Elde edilen bu olumlu ve ümit verici sonuçlar, pridin ve amonyak emilim deneyleri ile de

desteklenmektedir.Bu deneyler, AZT-temelli katalizörlerin yüzey asitliklerinin ticari katalizörden daha fazla olduğunu göstermektedir.

Anahtar Kelimeler: NSR/LNT, $Al_2O_3/ZrO_2/TiO_2$, Pt, NO_x, SO_x, NSC, FTIR, TPD

Acknowledgement

First, I would like offer my sincere thanks to Assoc. Prof. Dr. Emrah Özensoy for his endless support, patience, motivation and supervision throughout my entire academic career. He does not only behave as a supervisor, but more like a real brother. It was a wonderful experience to be a part of his research group. Moreover, it was a great privilege to be the first PhD student in his research group. I will always keep your contribution to whole part of my life in my mind. Thank you so much 'Hocam'.

On the other side, I would like to thank to Merve Tohumeken for her collaboration and unlimited support. She has provided cooperation throughout my studies, for which I am thoroughly grateful and can never forget. Thank you so much 'The Kunt'.

I also would like to acknowledge my Thesis Progress Committee members Prof. Ömer Dağ and Prof. Saim Özkar for their valuable contributions during my entire PhD study. I also would like to thank my PhD Dissertation Committee Members, Prof. Timur Doğu and Assistant Prof. Ferdi Karadaş for their time and consideration.

I would also like to thank Prof. Louise Olsson and Dr. Oana Mihai of Chalmers University of Technology, Department of Chemical Engineering for their valuable contribution and fruitful discussions.

I also wish to acknowledge Merve Doğaç Kurt, Pelin Altay, Kerem Emre Ercan, Zehra Aybegüm Samast, Elif Perşembe, Mustafa Karatok and Emrah Parmak for their scientific contribution and friendship.

I also acknowledge to TUBITAK for financial support.

I am ever grateful to my Uncle Sami Say for being there whenever I am in need. He was always like more than a *'father'* with his great support and encouragement all throughout my life. I really owe my sincerest and earnest gratitude to SAY family!

The most special thanks go to my Mother. You gave me all the time I ask. It was really a great comfort to know that you support all my decisions and moves with no doubt.

♥***Finally, to my wife, Yasemin SAY: my deepest love and endless gratitude*** ♥

“Dedicated to my endless love Yasemin”

Contents

Chapter 1 1

Introduction 1

1.1 Air Pollution Caused by Exhaust Emissions 1

1.2 Operational Principles of NSR Catalysts 3

1.3 Mechanistic View of NO_x Sorption and Reduction 5

1.4 Critical Aspects of NSR/LNT Catalysis 7

1.4.1 NO_x Storage Capacity (NSC) 7

1.4.2 SO_x Poisoning 10

1.5 Structural Properties of Metal Oxides in the NSR/LNT Support Framework 14

1.5.1 TiO_2 14

1.5.2 ZrO_2 14

1.5.3 Al_2O_3 15

1.6 Coordination Chemistry of Nitrate (NO_3^-) Ion 15

1.7 Coordination Chemistry of Sulfate (SO_4^{2-}) Ion 16

Chapter 2 18

Experimental 18

2.1 Material Synthesis 18

2.1.1 Synthesis of Binary Oxide ZrO_2/TiO_2 Materials 18

2.1.2 Synthesis of Ternary Oxide $Al_2O_3/ZrO_2/TiO_2$ Materials 19

2.1.3 Synthesis of $Pt/Al_2O_3/ZrO_2/TiO_2$ Materials 19

2.1.4 Synthesis of $Pt/BaO/Al_2O_3/ZrO_2/TiO_2$ Materials 20

2.1.5 Synthesis of $Pt/K_2O/Al_2O_3/ZrO_2/TiO_2$ Materials 20

2.1.6 Synthesis of $Pt/BaO/\gamma\text{-}Al_2O_3$ Materials 21

2.2 Instrumentation: 23

2.2.1 Experimental Setup 23

2.2.2 Characterization Techniques 24

2.2.2.1 X-ray Diffraction (XRD) Patterns 24

2.2.2.2 Raman Spectroscopy 25

2.2.2.3 BET Surface Area Analysis 26

2.2.2.4 FTIR Spectroscopy 26

2.2.2.5 Temperature Programmed Desorption (TPD) 30

2.2.3 Experimental Procedures 32

2.2.3.1 NO_x adsorption *via* FTIR 32

2.2.3.2 NO_x Desorption and Reduction *via* FTIR 32

2.2.3.3 SO_x adsorption *via* FTIR 33

2.2.3.4 SO_x desorption *via* FTIR 33

2.2.3.5 NO_x desorption *via* TPD 34

2.2.3.6 SO_x desorption *via* TPD 34

2.2.3.7 Pyridine Adsorption *via* FTIR 34

2.2.3.8 Ammonia Adsorption *via* TPD 34

2.2.3.9 Monolith Preparation for Flow Mode Catalytic Performance Tests 35

2.2.3.10 Flow Reactor Measurements 36

Chapter 3 38

Results and Discussion 38

3.1 Structural Characterization 38

3.1.1 X-Ray Diffraction Analysis 38

3.1.1.1 Binary Support Oxides 38

3.1.1.2 Ternary Support Oxides: 39

3.1.1.3 Pt-supported NSR/LNT Catalysts 40

3.1.2 Raman Spectroscopy 43

3.1.2.1 Binary Oxide Materials 43

3.1.2.2 Ternary Oxide Materials: 45

3.1.3 BET Specific Surface Area (SSA) Analysis 46

3.1.3.1 Binary Oxide Materials 46

3.1.3.2 Ternary Oxide Materials 47

3.1.3.3 Pt-supported NSR/LNT Catalysts 48

3.1.4 Pore Size Analysis *via* N_2 Sorption 50

3.2 *in-situ* FTIR Analysis 52

3.2.1 NO_x Adsorption Properties 52

3.2.1.1 NO_x Adsorption on Binary and Ternary Support Oxides 52

3.2.1.2 NO_x Adsorption on Pt-Supported Binary and Ternary Oxides 53

3.2.1.3 NO_x Adsorption on Pt-Supported NSR/LNT Catalyst with Basic Storage Domains 54

3.2.2 NO_x Reduction *via* H_2(g) 60

3.2.2.1 NO_x Reduction *via* H_2(g) on Binary and Ternary Support Oxides 60

3.2.2.2 NO_x Reduction *via* H_2(g) on Pt-Functionalized Binary and Ternary Oxides 62

3.2.2.3 NO_x Reduction *via* H_2(g) on Pt and Basic Oxide-Functionalized AZT Catalysts 66

3.2.3 SO_x Adsorption Properties. 79

3.2.3.1 SO_x Adsorption on Binary and Ternary Support Oxides 79

3.2.3.2 SO_x Adsorption on Pt-functionalized Binary and Ternary Oxides 81

3.2.3.3 SO_x Adsorption on Pt-functionalized Ternary Oxides with Basic Storage Domains 82

3.2.4 SO_x Reduction Properties 88

3.2.4.1 SO_x Reduction on Pt-functionalized Binary and Ternary Oxides 88

3.2.4.2 SO_x Reduction on Pt-functionalized Binary and Ternary Oxides with Basic Storage Domains 90

3.3 Temperature Programmed Desorption (TPD) Analysis 97

3.3.1 NO_x Adsorption and Desorption Properties*via* TPD 97

3.3.1.1 NO_x TPD on Binary and Ternary Oxides 97

3.3.1.2 NO_x TPD on Pt-Functionalized Binary and Ternary Oxides 101

3.3.1.3 NO_x TPD on Pt-functionalized Binary and Ternary Oxides with Basic Oxides 104

3.3.2 SO_x Adsorption and Desorption Properties*via* TPD 112

3.3.2.1 SO_x TPD on Pt-functionalized Binary and Ternary Oxides 112

3.3.2.2 SO_x TPD on Pt-functionalized Ternary Oxides Containing Basic Storage Domains 114

Chapter 4 127

Flow Reactor Measurements 127

4.1 NO_x Storage Capacity of BaO-based NSR/LNT Catalysts 127

Chapter 5 133

Conclusion 133

References 140

APPENDIX 151

List of Figures

Figure 1: Fuel consumption and three-way performance of gasoline engines. Reprinted with permission from ref. 4. Copyright 2000 CATTECH [4]..... 3

Figure 2: Types of Infrared Spectroscopy. Copyright Wiley-VCH Verlag GmbH & Co. [91] 27

Figure 3: Potential energy change as a function of the interatomic distance in a harmonic oscillator..... 29

Figure 4: Potential energy change as a function of interatomic distance in anharmonic oscillator..... 30

Figure 5: Experimental Setup for TPD Experiments. Copyright Wiley-VCH Verlag GmbH & Co.[91]. 31

Figure 6: XRD patterns corresponding to (a) ZT30 and (b) ZT70 binary oxide materials as a function of calcination temperature within 323 and 1173 K..... 38

Figure 7: XRD patterns corresponding to (a) AZT30 and (b) AZT70 ternary oxide materials as a function of calcination temperature within 323 and 1173K..... 39

Figure 8: XRD patterns corresponding to Pt/AZT, Pt/8BaO/AZT, Pt/20BaOAZT, Pt/20BaO/Al and Pt/20BaO/ZTmaterials upon calcination at 973 K. 41

Figure 9: XRD patterns corresponding to Pt/AZT, Pt/2.7K_2O/AZT, Pt/5.4K_2O/AZT, Pt/10K_2O/AZT and Pt/20BaO/Almaterials upon calcination at 973 K..... 42

Figure 10: Ex-situ Raman spectra corresponding to (a) ZT30 and (b) ZT70 materials upon calcination at temperatures within 773-1173 K. 43

Figure 11: Ex-situ Raman spectra corresponding to (a) AZT30 and (b) AZT70 materials upon calcination at temperatures within 973-1173 K..... 45

Figure 12: Specific surface area (SSA) values corresponding to (a) binary and (b) ternary materials upon calcination at temperatures within 773-1173 K. 47

Figure 13: BET specific surface area values for BaO-supported materials after calcination at 973 K for 150 min. 48

Figure 14: BET specific surface area values for the K_2O-supported materials in comparison to benchmark Pt/20BaO/Al_2O_3 after calcination at 973 K for 150 min. 49

Figure 15: N_2 adsorption(black)/desorption(red) isortherms of (a) mesoporous binary and (b) mesoporous-ternary oxides and pore size distribution of corresponding metarials of (c) mesoporous binary and (d) mesoporous-ternary oxides. Both materials were calcined at 973 K for 150 min. 51

Figure 16**:** FTIR spectra corresponding to the stepwise NO_2(g) adsorption at 323 K on (a) ZT and (b) AZT surfaces. The bold (red) spectrum in each panel corresponds to the NO_x-saturated (5.0 Torr NO_2(g) for 10 min. at 323 K) surface. Copyright 2014 Elsevier B.V. [67]. 52

Figure 17: FTIR spectra corresponding to the stepwise NO_2(g) adsorption at 323 K on (a) Pt/ZT and (b) Pt/AZT surfaces. The bold (red) spectrum in each panel corresponds to the NO_x-saturated (5.0 Torr NO_2(g) for 10 min. at 323 K) surface… 53

Figure 18: FTIR spectra corresponding to the stepwise NO_2(g) adsorption at 323 K on (a) Pt/AZT, (b) Pt/8BaO/AZT, (c) Pt/20BaO/AZTand Pt/20BaO/Al_2O_3surfaces. The bold (red) spectrum in each panel corresponds to the NO_x-saturated (5.0 Torr NO_2(g) for 10 min. at 323 K) surface. 55

Figure 19: FTIR spectra corresponding to the stepwise NO_2(g) adsorption at 323 K on (a) Pt/AZT, (b) Pt/2.7K_2O/AZT, (c) Pt/5.4K_2O/AZT and (d) Pt/10K_2O/AZTsurfaces. The bold (red) spectrum in each panel corresponds to the NO_x-saturated (5.0 Torr NO_2(g) for 10 min. at 323 K) surface. 57

Figure 20: FTIR spectra corresponding to the temperature-dependent nitrate reduction *via* 15.0 Torr of H_2(g) on (a) ZT and (b) AZT surfaces. The topmost spectrum in each panel corresponds to the NO_x-saturated (5.0 Torr NO_2(g) for 10 min. at 323 K) surface. The series of black spectra in each panel were collected at different temperatures within 323-723 K. The bottommost (red) spectrum in each panel corresponds to the highest reduction temperature exploited (i.e. 623 K for ZT and 723 K for AZT). Copyright 2014 Elsevier B.V.[67]..... 60

Figure 21: FTIR spectra corresponding to the temperature-dependent nitrate reduction *via* 15.0 Torr of H_2(g) on (a) AZT and (b) AZT surfaces. The topmost spectrum in each panel corresponds to the NO_x-saturated (5.0 Torr NO_2(g) for 10 min. at 323 K) surface. The series of black spectra in each panel were collected at different temperatures within 323-723 K. The bottommost (red) spectrum in each panel corresponds to the highest reduction temperature exploited (i.e. 623 K for ZT and 723 K for AZT). Copyright 2014 Elsevier B.V.[67]..... 62

Figure 22: FTIR spectra corresponding to the time-dependent nitrate reduction *via* 15.0 Torr of H_2(g) on Pt/AZT, (b) Pt/8BaO/AZT (c) Pt/20BaO/AZT and (d) Pt/20BaO/Al surfaces. The topmost spectrum (*i*) in each panel corresponds to the NO_x-saturated (5.0 Torr NO_2(g) for 10 min. at 323 K) surface. The series of spectra (*ii), (iii), (iv) and (v)* were collected as a function of time at 3th, 10th, 30th and 120th min of reduction at 323 K; respectively. The bottom set of FTIR spectra in each panel were collected after the initial 120 min reduction at 323 K by increasing to temperature to 373, 423 and 473 K in the presence of H_2(g)..... 68

Figure 23: –OH/–NH stretching region of the in-situ FTIR spectra corresponding to NO_2 saturation *(i)* (5.0 Torr NO_2(g) for 10 min. at 323 K) followed by subsequent reduction with 15.0 Torr of H_2(g) on (a) Pt/AZT, (b) Pt/8BaO/AZT, (c) Pt/20BaO/AZT and (d) Pt/20BaO/Al_2O_3 at 323 K. The series of spectra *(ii), (iii), (iv) and (v)* were collected as a function of time at 3th, 10th, 30th and 120th min of reduction at 323 K; respectively. 70

Figure 24: FTIR spectra corresponding to the time-dependent nitrate reduction *via* 15.0 Torr of H_2(g) on (a) Pt/AZT, (b) Pt/2.7K_2O/AZT (c) Pt/5.4K_2O/AZT and (d) Pt/10K_2O/AZT surfaces. The topmost spectrum (*i*) in each panel corresponds to the NO_x-saturated (5.0 Torr NO_2(g) for 10 min. at 323 K) surface. The series of spectra (*ii), (iii), (iv) and (v)* were collected as a function of time at 3th, 10th, 30th and 120th min of reduction at 323 K; respectively. The bottom set of FTIR spectra in each panel were collected after the initial 120 min reduction at 323 K followed by increasing to temperature to 473 and 573 K in the presence of H_2(g). 74

Figure 25: –OH/–NH stretching region of the in-situ FTIR spectra corresponding to NO_2 saturation *(i)* (5.0 Torr NO_2(g) for 10 min. at 323 K) followed by subsequent

reduction with 15.0 Torr of H_2(g) on (a) Pt/AZT, (b) Pt/2.7K_2O/AZT, (c) Pt/5.4K_2O/AZT and (d) Pt/10K_2O/AZT at 323 K. The series of spectra *(ii), (iii), (iv) and (v)* were collected as a function of time at 3th, 10th, 30th and 120th min of reduction at 323 K; respectively. 76

Figure 26: Time-dependent *in-situ* gas phase FTIR spectra corresponding to nitrate reduction via 15.0 Torr of H_2(g) on Pt/Al_2O_3/ZrO_2/TiO_2 at 323 K for 120 min. Red spectrum in each panel corresponds to the last spectrum obtained at the end of the given time interval..... 78

Figure 27: FTIR spectra corresponding to SO_x uptake/adsorption properties of (a) ZT and (b) AZT. Bottom black set of spectra in each panel were acquired after SO_x exposure (2.0 Torr, SO_2:O_2 = 1:10) at 323 K, followed by annealing at 373, 473, 573 K (black spectra) and 673 K (red spectra) in the SO_x gas mixture for 5 min. All spectra were recorded at 323K. 79

Figure 28: FTIR spectra corresponding to SO_x uptake/adsorption properties of (a) Pt/ZT and (b) Pt/AZT. Black set of spectra in each panel were acquired after SO_x exposure (2.0 Torr, SO_2:O_2 = 1:10) at 323 K, followed by annealing at 373, 473, 573 K (black spectra) and 673 K (red spectra) in the SO_x gas mixture for 5 min. All spectra were recorded at 323 K. 81

Figure 29:FTIR spectra corresponding to SO_x uptake/adsorption properties of (a) Pt/AZT, (b) Pt/8BaO/AZT, (c) Pt/20BaO/AZT and (d) Pt/20BaO/Al. Black set of spectra in each panel were acquired after SO_x exposure (2.0 Torr, SO_2:O_2 = 1:10) at 323 K, followed by annealing at 373, 473, 573 K (black spectra) and 673 K (red spectra) in the SO_x gas mixture for 5 min. All spectra were recorded at 323 K. 83

Figure 30: FTIR spectra corresponding to SO_x uptake/adsorption properties of (a) Pt/AZT, (b) Pt/2.7K_2O/AZT(c) Pt/5.4K_2O/AZT and (d) Pt/10K_2O/AZT surfaces. Black set of spectra in each panel were acquired after SO_x exposure (2.0 Torr, SO_2:O_2 = 1:10) at 323 K, followed by annealing at 373, 473, 573 K (black spectra) and 673 K (red spectra) in the SO_x gas mixture for 5 min. All spectra were recorded at 323 K. 85

Figure 31: FTIR spectra corresponding to SO_x release/desorption properties of (a) Pt/ZT and (b) Pt/AZT. Catalystswere initially pre-sulfated (2.0 Torr, SO_2:O_2 = 1:10 for 5 min at 673 K) and then exposed to H_2(g) (15.0 Torr), at 323, 473, 673, 773 K for 5 min. All spectra were recorded at 323 K. 88

Figure 32: FTIR spectra related to SO_x release/desorption properties of (a) Pt/AZT, (b) Pt/8BaO/AZT, (c) Pt/20BaO/AZT and (d) Pt/20BaO/Al. Catalystswere initially pre-sulfated (2.0 Torr, SO_2:O_2 = 1:10 for 5 min at 673 K) and then exposed to H_2(g) (15.0 Torr), at 323, 473, 673, 773, 873 and 973 K for 5min. All spectra were recorded at 323 K. 91

Figure 33: FTIR spectra corresponding to Pt/20BaO/Al (red spectra) and Pt/AZT (black spectra) catalysts after 5.0 Torr NO_2 exposure at 573 K for 10 min and subsequent evacuation. All spectra were recorded at 323 K. 93

Figure 34: FTIR spectra related to SO_x release/desorption properties of (a) Pt/AZT, (b) Pt/2.7K_2O/AZT (c) Pt/5.4K_2O/AZT and (d) Pt/10K_2O/AZTmaterials. Catalystswere initially pre-sulfated (2.0 Torr, SO_2:O_2 = 1:10 for 5 min at 673 K) and then exposed to H_2(g) (15.0 Torr), at 323, 473, 673, 773, 873 and 973 K for 5 min. All spectra were recorded at 323 K. 95

Figure 35: TPD profiles obtained from (a) ZT and (b) AZTsamples after saturation with 5 Torr NO_2(g) at 323 K for 10 min. The inset in each panel presents the FTIR spectra of the surfaces before (black) and after (red) TPD analysis. Copyright 2014 Elsevier B.V. [67]. 98

Figure 36: TPD profiles obtained from (a) Pt/ZT and (b) Pt/AZTsamples after saturation with 5 Torr NO_2(g) at 323 K for 10 min. The inset in each panel presents the FTIR spectra of the surfaces before (black) and after (red) TPD analysis. Copyright 2014 Elsevier B.V.[67]. 101

Figure 37: TPD profiles obtained from (a) Pt/AZT, (b) Pt/8BaO/AZT, (c) Pt/20BaO/AZT and (d) Pt/20BaO/Al_2O_3 samples after saturation with 5 Torr NO_2(g) at 323 K for 10 min. The inset in each panel shows the FTIR spectra of the surfaces before (black) and after (red) TPD analysis. 105

Figure 38: (a) Integrated NO_x TPD desorption signals and (b) corresponding SSA-normalized values..... 107

Figure 39: TPD profiles obtained from (a) Pt/AZT, (b) Pt/2.7K_2O/AZT, (c) Pt/5.4K_2O/AZT and (d) Pt/10K_2O/AZTsamples after saturation with 5 Torr NO_2(g) at 323 K for 10 min. The inset in each panel shows the FTIR spectra of the surfaces before (black) and after (red) TPD analysis. 109

Figure 40: (a) Integrated values regarding relative NO_x adsorption capabilities derived from TPD analysis and (b) their SSA normalized values. 111

Figure 41: TPD profiles for (a) Pt/ZT and (b) Pt/AZT after 2.0 Torr SO_x (2.0 Torr SO_2+O_2, SO_2:O_2 = 1:10) adsorption at 673 K for 30 min. 112

Figure 42: TPD profiles for (a) Pt/AZT, (b) Pt/8BaO/AZT, (c) Pt/20BaO/AZT and (d) Pt/20BaO/Al catalysts after 2.0 Torr SO_x (2.0 Torr SO_2+O_2, SO_2:O_2 = 1:10) adsorption at 673 K for 30 min. 115

Figure 43: FTIR spectra corresponding to residual sulfur content on (a) Pt/AZT, (b) Pt/8BaO/AZT, (c) Pt/20BaO/AZT and (d) Pt/20BaO/Al catalysts before (black) and after (red) SO_x-TPD analysis. 117

Figure 44: In-situ FTIR spectra corresponding to pyridine adsorption on (a) Pt/AZT, (b) Pt/8BaO/AZT, (c) Pt/20BaO/AZT and (d) Pt/20BaO/Al catalysts at 298 K. 119

Figure 45: NH_3 TPD profiles of Pt/AZT, Pt/8BaO/AZT, Pt/20BaO/AZT and Pt/20BaO/Al catalysts. The samples were exposed to 2000 ppm NH_3 at 323 K for 8 h during adsorption. After the samples were treated with argon for 30 min, the temperature was increased to 1073 K in argon and the ammonia desorption occurs. 121

Figure 46: Integrated TPD signals obtained *via* NH_3-TPD experiments. 121

Figure 47: TPD profiles for (a) Pt/AZT, (b) Pt/2.7K_2O/AZT, (c) Pt/5.4K_2O/AZT and (d) Pt/10K_2O/AZT catalysts after 2.0 Torr SO_x (2.0 Torr SO_2+O_2, SO_2:O_2 = 1:10) adsorption at 673 K for 30 min. 122

Figure 48: FTIR spectra corresponding to residual sulfur content on (a) Pt/AZT, (b) Pt/2.7K_2O/AZT, (c) Pt/5.4K_2O/AZT and (d) Pt/10K_2O/AZT catalysts before (black) and after (red) SO_x-TPD analysis. 126

Figure 49: NO_x concentration profiles during last two lean/rich cycles over synthesized Pt-based catalysts. The samples were exposed to lean mixture of either

(a) NO, CO_2, O_2 and H_2O or (b) NO_2, CO_2, O_2 and H_2O at different temperatures of 473, 573 and 673K. The experimental details are described in the experimental section. 127

Figure 50: Total amount of NO_x stored on fresh (i) Pt/AZT, (ii) Pt/8BaO/AZT, (iii) Pt/20BaO/AZT and (iv) Pt/20BaO/Al_2O_3 catalysts obtained under lean mixture of either (a) NO, CO_2, O_2 and H_2O or (b) NO_2, CO_2, O_2 and H_2O at different temperatures of 473, 573 and 673K. 128

Figure 51: Initial NO_x adsorption rates for each catalyst at 573K in FM^1 mixture. This Figure was derived from the Figure 49a and also valid for all other temperatures and feed mixtures. 130

List of Tables

Table 1: European exhaust emission regulations for diesel passenger cars. 2

Table 2: European exhaust emission regulations for gasoline passenger cars. 2

Table 3: Nominal loadings of the individual components in the synthesized catalysts. 22

Table 4: Classification of Infrared Radiation Frequencies [91] 27

Table 5: Gas concentrations for different feed mixtures 37

List of Schemes

Scheme 1: NO emission contribution in 15 EU countries for the last two decades [1]. 1

Scheme 2: Illustration of the cyclic operational principle of a typical NSR catalyst. . 4

Scheme 3: Reaction pathway for NO_x adsorption over supported Pt–Ba catalysts. Reprinted with permission from ref. 14. Copyright 2006 Elsevier B.V. [14]..... 6

Scheme 4: Point group symmetries and different coordination schemes of NO_3^- ion. 16

Scheme 5: Point group symmetries and different coordination of free sulfate ion.... 17

Scheme 6: Schematics of the *in-situ* FTIR and TPD experimental setup [90]. 23

Scheme 7: Schematic illustration of nitrate reduction mechanism. 65

Scheme 8: Schematic illustration of sulfur adsorption desorption performance of AZT and γ-Al_2O_3 supported materials. 132

List of Abbreviations

BET: Brunauer-Emmett-Teller

EDX: Energy-Dispersive X-ray spectroscopy

FTIR: Fourier Transform Infrared Spectroscopy

ICDD: International Center for Diffraction Database

IR: Infrared

JCPDS: Joint Committee on Powder Diffraction Standards

NIST: National Institute of Standards and Technology

NO_x: Nitrogen Oxides (e.g. N_2O, NO, NO_2)

NSR: NO_x Storage and Reduction

NSC: NO_x Storage Capacity

PGM: Platinum Group Metal

PID: Proportional Integral Derivative

RT: Room Temperature

QMS: Quadruple Mass Spectrometer

SCR: Selective Catalytic Reduction

$SO_{x:}$ Sulfur Oxides (e.g. SO_2, SO_3)

SSA: Specific Surface Area

TPD: Temperature Programmed Desorption

TPR: Temperature Programmed Reduction

XRD: X-Ray Diffraction

Chapter 1

Introduction

1.1 Air Pollution Caused by Exhaust Emissions

The growth in worldwide population and industrialization causes an increase in the energy demand of almost all sectors. Air pollution is one of the most challenging problems of our ecosystem and the industrialized world. Atmosphere is an extremely complex system where numerous chemical, physical and biological processes take place simultaneously. NO_x emission from mobile sources has serious destructive effects on the atmosphere, global ecosystem and especially on the human health. About one half of the total NO_x emissions results from mobile sources as illustrated in Scheme 1 [1]. For example, NO_x emissions due to mobile sources makes almost 80% of the total NO_x emissions in Buenos Aires [2].

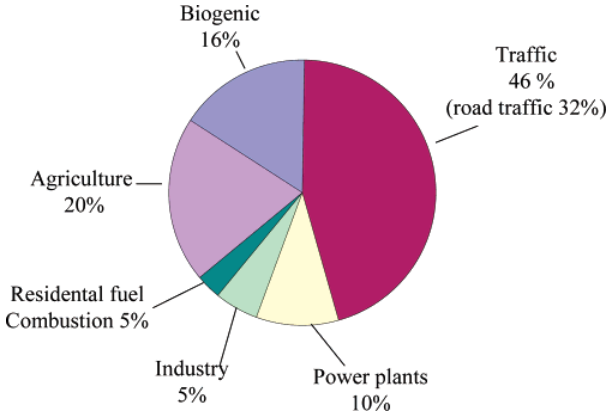

Scheme 1: NO emission contribution in 15 EU countries for the last two decades [1].

While the earlier regulations in 1988 for diesel engines were only concerned with particle emissions, other hazardous pollutants such as CO, SO_2, NO_x and unburned hydrocarbons from stationary and mobile sources are also being regulated with increasingly stringent limitations [3]–[5]. Concentrations of these hazardous

gases are highly dependent on the type of engine, fuel and driving conditions (e.g. highway vs. urban driving cycles). These concentration values are found to be higher in heavier vehicles and trucks. European exhaust emission standards for diesel and gasoline engines are listed in detail in Table 1 and Table 2; respectively [6].

Diesel	Date	CO (g/km)	NO_x (g/km)	HC+NO_x (g/km)	PM (g/km)	Total HC (g/km)
Euro 1	1992	2.72	-	0.97	0.14	-
Euro 2	1996	1.0	-	0.7	0.08	-
Euro 3	2000	0.64	0.50	0.56	0.05	-
Euro 4	2005	0.50	0.25	0.30	0.025	-
Euro 5	2009	0.50	0.180	0.23	0.005	-
Euro 6	2014	0.50	0.080	0.17	0.005	-

Table 1: European exhaust emission regulations for diesel passenger cars.

Gasoline	Date	CO (g/km)	NO_x (g/km)	HC+NO_x (g/km)	PM (g/km)	Total HC (g/km)
Euro 1	1992	2.72	-	0.97	-	-
Euro 2	1996	2.2	-	0.5	-	-
Euro 3	2000	2.3	0.15	-	-	0.20
Euro 4	2005	1.0	0.08	-	-	0.10
Euro 5	2009	1.0	0.06	-	0.005	0.10
Euro 6	2014	1.0	0.06	-	0.005	0.10

Table 2: European exhaust emission regulations for gasoline passenger cars.

Since the environmental regulations become highly rigorous, automotive industry is being forced to innovate new technologies to meet the legislations by lowering the exhaust emission levels. Three-way catalysts (TWC) have been used for the reduction of CO, NO_x, and hydrocarbon (HC) emissions in gasoline powered engines operating under air to fuel ratios (A/F) equal to 14.5 as shown in Figure 1.

On the other hand, lean burn and diesel engines have significant benefits associated with the fuel economy and combustion efficiency as they operate at A/F = 24. However, under such oxidizing (i.e. lean) conditions, hydrocarbons and NO_x cannot be effectively reduced via conventional TWC systems.

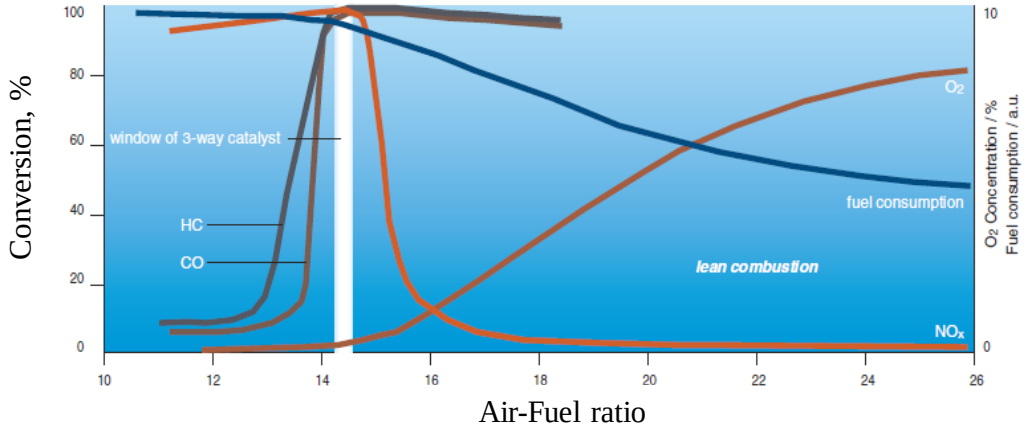

Figure 1: Fuel consumption and three-way performance of gasoline engines. Reprinted with permission from ref. 4. Copyright 2000 CATTECH [4].

For lean burn engines, a promising after treatment method for the catalytic NO_xreduction from mobile sources is the NO_xstorage/reduction (NSR) catalyst technology which was innovated by Toyota Motor Corporation [7], [8].

1.2 Operational Principles of NSR Catalysts

NSR catalysts, which are also called as Lean-NO_x Traps (LNT), operate under lean (oxygen rich) and rich (reductant rich/oxygen deficient) cyclic conditions as demonstrated in Scheme 2. Cyclic NSR/LNT operation takes place via four different steps summarized as follow:

- NO is produced as the primary gas among other NO_x species upon fuel combustion. NO(g) is initially oxidized to nitrogen dioxide NO_2 on PGM sites.
- Both NO and NO_2 gas species are stored/trapped by the NO_x storage domainsin the form of metal nitrites and/or nitrates.
- As the exhaust gas composition is switched to the rich cycle, catalyst is exposed to these additional reductants (e.g. CO, hydrocarbons and H_2)

and majority of the trapped nitrites and nitrates are released from the NO_x storage domains in the form of N_2, NH_3, and N_2O.

- These released NO_x species are subsequently reduced to harmless N_2 on the PGM sites.

After the completion of the rich period, resultant catalyst is regenerated and adsorption sites become available for the next lean period (see reaction sequence 1.1 and 1.2 below [4]).

$$NO \xrightarrow{Pt} NO_2 \xrightarrow{BaO} Ba(NO_3)_2 \qquad 1.1$$

$$Ba(NO_3)_2 \rightarrow BaO + NO_2 \xrightarrow{HC_x} N_2 + CO_2 + H_2O \qquad 1.2$$

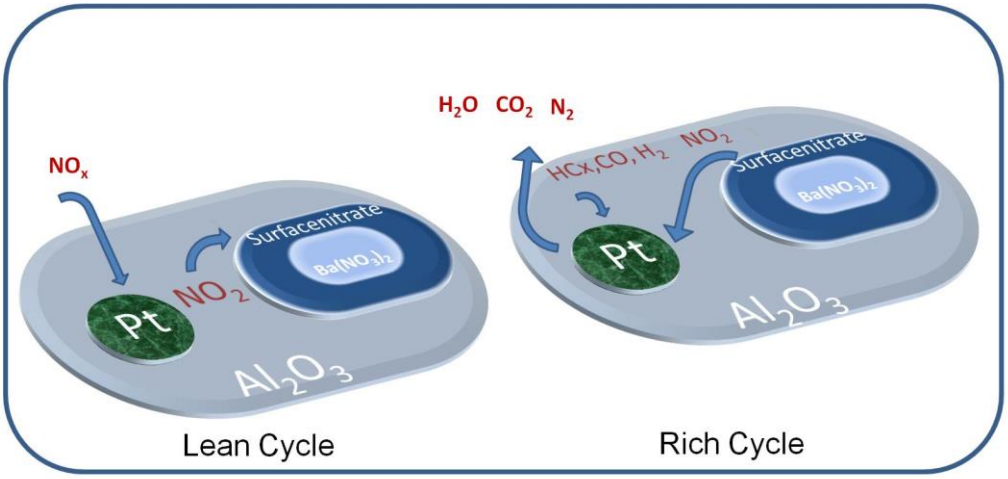

Scheme 2: Illustration of the cyclic operational principle of a typical NSR catalyst.

It is worth mentioning that the most commonly utilized catalyst formulation in NSR systems is $Pt/BaO/Al_2O_3$.

1.3 Mechanistic View of NO_x Sorption and Reduction

Adsorption of NO_2 on basic metal oxides are generally more effective as compared to NO [9], [10]. Therefore, NO_2 formation as a result of NO oxidation is one of the critical steps. This oxidation process is primarily driven by the precious metals suggested by following steps [11]:

$$NO + Pt \rightarrow NO\text{-}Pt \quad 1.3$$

$$NO\text{-}Pt + Pt \rightarrow N\text{-}Pt + O\text{-}Pt \quad 1.4$$

$$NO\text{-}Pt + O\text{-}Pt \rightarrow NO_2 + 2Pt \quad 1.5$$

Several reports suggested that the adsorption of NO_2 molecules on storage domains (*i.e.* BaO) is a sequential process where nitrite formation is followed by the nitrate formation [12], [13]. A three-step mechanism for the NO_x sorption was proposed by Fridell and co-workers as follows [12]:

$$BaO + NO_2 \rightarrow BaO\text{-}NO_2 \quad 1.6$$

$$BaO\text{-}NO_2 \rightarrow BaO_2 + NO \quad 1.7$$

$$BaO_2 + 2NO_2 \rightarrow Ba(NO_3)_2 \quad 1.8$$

On the other hand, Forzatti and co-workers proposed two different NO_x sorption routes [14], [15]. The first route was called the ‘’nitrate route’’ where NO is initially oxidized to NO_2 with the help of the precious metal, followed by the NO_2 spillover onto the BaO storage sites, forming barium nitrates together with the evolution of NO into the gas phase. The second route is known as the ‘’nitrite route’’. In this pathway, NO is oxidized on the Pt sites and directly stored on

adjacent BaO storage domains in order to form nitrites which are subsequently oxidized to barium nitrates. These two different routes are summarized as follows [14].

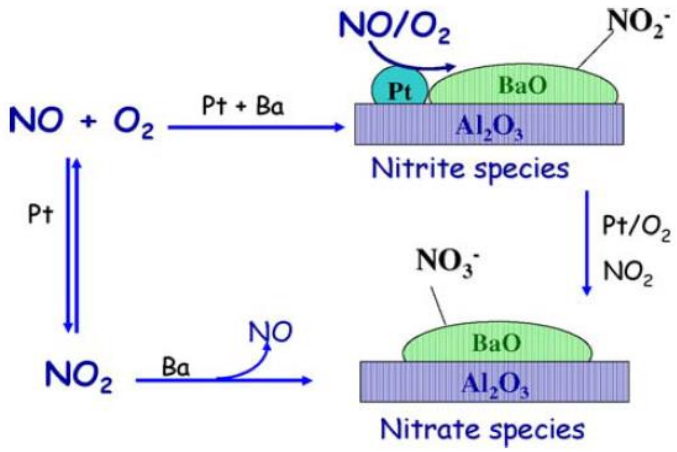

Scheme 3: Reaction pathway for NO_x adsorption over supported Pt–Ba catalysts. Reprinted with permission from ref. 14. Copyright 2006 Elsevier B.V. [14]

On the other hand, trapped NO_x species are reduced upon the introduction of the reducing agents as the engine operates in rich conditions in order to regenerate the catalyst for the next lean cycle. Some of the possible products generated upon nitrate/nitrite reduction in catalytically relevant temperature window (473-673 K) are listed below [14], [16]:

$$Ba(NO_3)_2 + 5H_2 \rightarrow BaO + N_2 + 5H_2O \quad 1.9$$

$$Ba(NO_3)_2 + 3H_2 \rightarrow BaO + 2NO + 3H_2O \quad 1.10$$

$$Ba(NO_3)_2 + 4H_2 \rightarrow BaO + N_2O + 4H_2O \quad 1.11$$

$$Ba(NO_3)_2 + 8H_2 \rightarrow BaO + 2NH_3 + 5H_2O \quad 1.12$$

1.4 Critical Aspects of NSR/LNT Catalysis

1.4.1 NO_x Storage Capacity (NSC)

As mentioned above, typical NSR/LNT catalysts are composed of basic metal oxides (i.e. BaO, K_2O, etc.), red-ox PGM sites (i.e. Pt, Pd, Rh) supported on a high surface area matrix (i.e. γ-Al_2O_3) [3], [4], [9]. There exist numerous studies on NSR applications, using BaO-based materials where the basic oxide loadings vary in between 8 and 20 wt. %. While 8 wt. % BaO loading leads to a nominal surface coverage of *ca.* 1.0 monolayer (ML) on γ-Al_2O_3, higher BaO loadings (i.e. 20 wt. %) causes the formation of bulk like structures (with a nominal surface coverage greater than a monolayer)[17]. Moreover, Lietti and co-workers reported that three different types of Ba-domains may exist on the Pt/BaO/Al_2O_3 catalyst prepared via wetness impregnation. These components are BaO, $Ba(OH)_2$ and $BaCO_3$. NO_x adsorption capacity of these species decreases in the following order: BaO, $Ba(OH)_2$ and $BaCO_3$ due to the decreasing basicity of the Ba-salts [18]. Baiker *et al.* reported a comprehensive study regarding the effect of BaO loading on the NO_x storage capacity (NSC). They found that NSC gradually increases up to a BaO loading of 16.7 wt.% and starts to decrease beyond this particular loading [19]. Also, it was shown that the traditional/conventional Pt/BaO/γ-Al_2O_3 NSR catalyst, exhibited an optimum NO_x conversion and storage performance within the temperature window of 473-673 K [20]–[28].

However, recent engine technologies including lean burn gasoline direct injection (GDI) systems providing high fuel economy require catalytic solutions that can efficiently operate at a temperature above 673 K where conventional catalysts cannot effectively function [29]. Toyota Motor Company has previously stated that

K_2O and BaO are two of the most promising NO_x storage domains to be used in NSR catalysts in terms of NO_x storage and hydrocarbon (HC) reduction [30]. Use of K_2O-based NSR materials attracted great interest due to their higher NSC at elevated temperatures as opposed to BaO [31]. Other advantages of K_2O storage domains are associated with their strong basicity and the lack of significant solid-state interactions between K_2O and γ-Al_2O_3 (i.e. absence of the existence of undesired $BaAl_2O_4$ phases) [32]. Luo *et al*. thoroughly studied the effect of K_2O loading (i.e. 2 – 20 wt. %) on NSC of $Pt/K_2O/\gamma$-Al_2O_3. It was found out that catalyst with 10 wt.% K_2O loading resulted in the highest NSC within the temperature window of 250-550 ^oC [32]. NSC of other alkaline earth metals (i.e. Mg, Sr, Ca) as well as alkali metals (i.e. Na, K) were also studied. These studies revealed that NSC was directly correlated to the basicity of the storage oxide where NSC increased in the order of K > Ba > Sr ≥ Na > Ca > Rb> Cs ≥ Li ≥ Mg [33]–[36].

On the other hand, as well as medium and high temperature deNO_x activities, conventional NSR materials are known to exhibit fairly low deNO_x efficiency in the temperature range of 373 and 473 K. Particularly, "The New European Driving Cycle" (NEDC) indicates that for short driving cycles (e.g. ~20 min), catalyst temperature remains below 423 K for almost 70 % of the driving cycle. Therefore, the 'passive NO_x traps' are utilized to handle NO_x species at low temperatures. Ag-supported materials reveal promising activity for NO oxidation and NO_x trapping at low temperatures [37]. Moreover, Tanaka *et al*. [38] performed a detail analysis on highly active Ag/Al_2O_3 and Ti-modified Ag/Al_2O_3 (*i.e.* $Ag/Ti/Al_2O_3$) catalysts as passive NO_x traps. Olsson *et al*. [39] stated that use of small concentration (*i.e.* 1500 ppm) of H_2 (g) during the lean stage yielded much better NO_x trapping ability for

Ag/Al_2O_3 at 473 K as compared to $Pt/BaO/Al_2O_3$[40]. On the other hand, ZrO_2 and TiO_2 based oxide catalysts have been also studied for low-temperature LNT applications. Machida *et al.* [41] illustrated that $Pt/ZrO_2/TiO_2$ exhibited best deNO_x activity at 373 K and lost its efficiency at higher temperatures.

Platinum Group Metals (PGM) are other key components of NSR applications, which are typically loaded to the catalyst within 1-2 wt. %. Pt, Pd and Rh are commonly used PGM in NSR formulations [42], [43]. While Pt is the most active metal for NO oxidation reactions, Pd and Rh metals are more effective in terms of NO_x reduction activity [3]. Ollson *et al.* has performed a comparative mechanistic investigation on $Pt/BaO/Al_2O_3$, $Rh/BaO/Al_2O_3$, Pt/Al_2O_3 andRh/Al_2O_3 catalysts. These results indicated that Rh-based materials had relatively lower NSC as compared to those of Pt-based counterparts due to the lower NO oxidation capability of the later materials [43]. On the other hand, Fridell *et al.* investigated $Pt/BaO/Al_2O_3$ and $Pd/BaO/Al_2O_3$ catalysts in order to compare their NSC and NO oxidation ability at different temperatures [44]. While $Pd/BaO/Al_2O_3$ had the highest NSC at 300 ^oC, $Pt/BaO/Al_2O_3$ had higher NSC at 400 ^oC along with higher NO oxidation activities at all of the investigated temperatures. Amiritis and coworkers also conducted similar experiments, reporting a higher NO_x reduction activity for $Pd/BaO/Al_2O_3$ within the temperature window of 250-350^oC [45]. Bi-metallic PGM systems were also studied in the literature in order to enhance the overall NSR activity [46]–[49]. For example, NO_x storage capacities and NO oxidation capabilities of a selected set of bimetallic systems were found to increase in the following order under lean conditions: $Pt/BaO/Al_2O_3$> $Pt\text{-}Rh/BaO/Al_2O_3$> $Rh/BaO/Al_2O_3$[47].

1.4.2 SO_x Poisoning

NSR catalysts have significant challenges associated with sulfur poisoning and thermal aging leading to the deterioration of active sites, sintering of PGM species and the formation of unwanted phases such as $BaAl_2O_4$ or $BaCeO_3$[24], [50]–[53]. Sulfur is an impurity present both in the fuel as well as in engine lubricants. Although sulfur concentration in diesel fuel has been significantly reduced over the recent years (*e.g.* Ultra Low Sulfur Diesel, ULSD has only 15 ppm of total sulfur content), complete removal of sulfur is still a technological and financial challenge for the petroleum refining industry.

Fuel combustion in the engine leads to the conversion of sulfur containing compounds into SO_2 which may also be subsequently oxidized into SO_3 upon interaction with tailpipe catalysts. These sulfur-related species gradually accumulate over the BaO storage components and form $BaSO_4$ [54]. Since the formation of $BaSO_4$ is thermodynamically more stable than those of $Ba(NO_3)_2$ and $BaCO_3$, it is not easy to regenerate the NSR/LNT catalyst at operational temperatures and the catalyst is poisoned due to the loss of available adsorption sites [18], [55]. Therefore, regeneration of NSR catalysts typically requires high temperatures (*e.g.* $T > 1000$ K). However, high temperature processes cause both sintering of PGM species and the formation $BaAl_2O_4$ domains with a low SSA [50], [52]. Regeneration duration and the type of reducing agents are other key parameters for sulfur regeneration and PGM sintering [56]. Poulston and Anderson investigated the influence of the reductant type on the catalyst regeneration and found out that H_2 is the most effective reducing agent as compared to CO and C_3H_6[57], [58].

Since both NO_2(g) and SO_2(g) are acidic adsorbates toward the basic oxides, they compete for the same adsorption sites on the catalyst surface. Therefore, improvement of the sulfur tolerance of an NSR/LNT system needs to be accomplished without compromising the NO_x storage capacity. Along these lines, numerous studies have been performed in order to develop an optimal catalytic material, which is resistant to sulfur poisoning [59]–[62]. Ozensoy *et al.* also worked on the design, synthesis and characterization of a variety of binary and ternary mixed metal oxide systems, which are promoted with reducible oxides such as Fe_2O_3/Fe_3O_4[63], TiO_2[22], [53], [64]–[66], CeO_2[23], [24] and ZrO_2[67]. For instance, they have demonstrated that CeO_2 is an effective promoter enabling a significant improvement in the NO_x reduction and sulfur regeneration of NSR/LNT catalysts.

Recent studies in the literature demonstrated that TiO_2 is a promising metal oxide support/promoter against sulfur deactivation of LNT catalysts, enabling much lower temperatures for sulfur removal due to its high surface acidity[50], [68]. In the field of automotive catalysis, TiO_2 was initially used by Toyota Motor Company in Corona Premio in 1992 as a TWC promoter. However, TiO_2 alone exhibits limited NO_x storage capacity as compared to that of γ-Al_2O_3 owing to its high surface acidity and low specific surface area [69]–[71]. Moreover, in spite of the promising activity of TiO_2 in sulfur regeneration, BaO can diffuse into the TiO_2 lattice, leading to the formation of complex mixed oxides such as $BaTiO_x$ and causes thermal deterioration due loss of active BaO sites [70], [71]. However, there exists opportunities to design novel mixed oxide systems that can simultaneously exhibit high NSC, thermal stability and sulfur tolerance. In order to explore such prospects, ZrO_2 and TiO_2

containing complex oxide architectures can be utilized. By altering the composition and crystal structure of such mixtures as well as by utilizing the well-known stabilizing influence of ZrO_2 on TiO_2[71], [72] and by increasing the surface acidity [73]–[75], promising alternative materials can be synthesized. The preferential choice of ZrO_2 as promoter is based on its reducibility and strong metal support interaction (SMSI) which prevents PGM sintering [76]. Moreover, zirconia is a good catalyst for on-board steam reforming reactions producing H_2 (i.e. most effective reducing agent) by utilizing C_3H_6 and H_2O in the exhaust pipeline [68].

Although, recent studies reported a higher sulfur resistance for $Pt/K/ZrO_2/TiO_2$ than that of $Pt/BaO/Al_2O_3$, one of the critical aspects to be considered in such efforts is the relatively low thermal stability of ZrO_2/TiO_2 binary mixed oxides [60], [61]. In one of our recent reports, the structural evolution of ZrO_2/TiO_2 and $Al_2O_3/ZrO_2/TiO_2$ mixed oxides was followed as a function of temperature by means of x-ray diffraction (XRD), Raman spectroscopy and N_2 sorption analysis techniques [67]. While the amorphous ZrO_2/TiO_2 material obtained after the synthesisreadily crystallizes at temperatures higher than 773 K to form ordered and low surface area structures such as $ZrTiO_4$ and t-ZrO_2, disordered (amorphous-like) structure of $Al_2O_3/ZrO_2/TiO_2$ persists even at 1173 K revealing a relatively higher NO_x uptake as compared to binary ZrO_2/TiO_2[67]. ZrO_2/TiO_2 and $Al_2O_3/ZrO_2/TiO_2$-based materials were also investigated in terms of their composition, thermal stability, NO_x storage capability and sulfur uptake/regeneration characteristics by Toyota Motor Company [77]–[79]. ZrO_2/TiO_2 with a mass ratio of 70:30 was claimed to have the highest tolerance against sulfur poisoning [80] and the influence of the Al_2O_3 on NO_x storage capacity, structural integrity, sintering

resistance, and thermal deterioration has been thoroughly illustrated [77]. Studies on the Pt/Rh/Ba/K/AZT catalyst which was comprised of a nano-composite ternary oxide $Al_2O_3/ZrO_2/TiO_2$-support showed excellent NSC than that of γ-$Al_2O_3/ZrO_2/TiO_2$-support, where the γ-Al_2O_3 was physically mixed with the ZrO_2/TiO_2 [77], [78]. Besides, Meng *et al.* [81] performed a detailed analysis on the effect of Al_2O_3 doping into the ZrO_2/TiO_2 matrix and indicated that an Al:(Ti+Zr) atomic ratio of 3:1 exhibited the highest NSC for fresh and sulfur-regenerated catalysts.

However, most of these comprehensive studies included a limited number of spectroscopic investigations on the interaction between SO_x and NO_x molecules and NSR/LNT catalyst surfaces. In the scope of current work, we comprehensively investigate the qualitative and quantitative NO_x and SO_x adsorption/uptake as well as nitrate and sulfate reduction/regeneration/release properties of the $Al_2O_3/ZrO_2/TiO_2$ (AZT)-supported Pt/BaO/AZT and Pt/K_2O/AZT NSR/LNT catalysts in comparison to a benchmark NSR/LNT catalyst (*i.e.* Pt/BaO/Al_2O_3). Generation of surface functional groups and their release/transformation behavior as a function of temperature and BaO/K_2O loading are systematically monitored by using *in-situ* Fourier Transform Infrared Spectroscopy (*in-situ* FTIR) and temperature programmed desorption (TPD). Moreover, the NSC of each investigated material was further investigated under flow conditions at different temperatures. Discussion in the current study provides a valuable molecular level insight regarding the adsorption/desorption characteristics of NO_x and SO_x species and detailed information regarding the delicate trade-off between NSC and sulfur poisoning phenomena under realistic flow mode conditions.

1.5 Structural Properties of Metal Oxides in the NSR/LNT Support Framework

1.5.1 TiO_2

In TiO_2, Ti^{4+} cations are coordinated to six O^{2-} atoms leading to the formation of TiO_6 octahedra. This arrangement yields three major TiO_2 polymorphs namely anatase, rutile and brookite [82]. These three different crystal structures differ by the distortions in the TiO_6 octahedra and the interatomic distances between Ti-Ti and Ti-O. Moreover, upon thermal annealing and possible phase transformations can occur between these polymorphs such as: anatase → brookite → rutile, anatase → rutile and brookite → rutile [82]. TiO_2 is an n-type semiconductor due its lattice oxygen deficiencies. Electronic band gap of each individual structures are 3.3, 3.1 and 3.2 eV for anatase, rutile and brookite; respectively, and TiO_2 is widely considered as indirect band gap material [83].

1.5.2 ZrO_2

ZrO_2 has three primary phases namely, monoclinic, tetragonal and cubic. ZrO_2 monoclinic phase can be transformed into other phases upon increase in temperature such as: monoclinic → tetragonal → cubic. Tetragonal phase of ZrO_2 structure can be stabilized by Yb_2O_3 and CeO_2 [84]. Unlike TiO_2, cations in zirconia (i.e. Zr^{4+}) are coordinated to seven and eight O^{2-} anions in the monoclinic and tetragonal/cubic structure; respectively which can partly be attributed to the larger ionic radius of Zr^{4+} relative to that of Ti^{4+}[85]. Electronic band gap of ZrO_2 depends strongly on the lattice structure, defects and synthesis protocols and vary between 5-7 eV [86].

1.5.3 Al_2O_3

γ-Al_2O_3 is the most commonly used oxide support in NSR formulations due to its porous structure, high surface area, high catalytic surface activity, distinct chemical, mechanical and thermal properties [3]. γ-Al_2O_3 has a defective spinel structure (space group F_d3_m) where the aluminum cations are located in the octahedral (O_h) and tetrahedral (T_d) interstitial sites identified by the face-centered-cubic (*fcc*) oxygen anion sublattice [87]. At elevated temperatures, γ-Al_2O_3 can go through polymorphic phase transitions to form other crystal structures, which are commonly called as the transitional alumina and eventually forms the thermodynamically stable α-Al_2O_3 (corundum) phase. This process is accompanied by a severe loss of porosity and sintering.

1.6 Coordination Chemistry of Nitrate (NO_3^-) Ion

Under oxidizing conditions, NO_2(g) molecules can oxidize upon interaction with the metal oxide surfaces by coordinating to the metal center and the oxide ions which can result in the formation of $Ba(NO_3)_2$, KNO_3, and $Al(NO_3)_3$. Free nitrate ion, NO_3^-, has the principal symmetry operators of *E*, C_3, C_2, σ_h, $S_3$and σ_v, generating D_{3h} symmetry point group. The vibrational modes of the free nitrate ion are A_1', A_2'', *E*', *E*''. These vibrational modes represented as υ_1, υ_2, υ_3 and υ_4 having IR frequencies located at 1050, 830, 1350 and 715 cm^{-1}; respectively. While the A_1' and A_2'' are non-degenerate, *E*' and *E*'' modes are doubly degenerate leading to 6 vibrational modes satisfying the expected total number of modes of a nonlinear molecule (*i.e. 3N-6* total number of modes, where *N* is the total number of atoms in the structure). Of the four fundamental vibrations, only two of them (A_2'', *E*') are IR active and A_1' and *E*'' are IR inactive.

Free nitrates can coordinate to a metal center as monodentate, bidentate and bridging nitrates as illustrated in scheme 4.

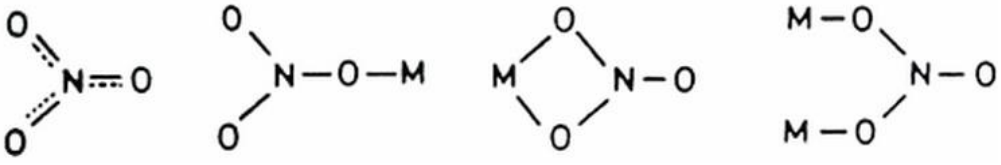

Free Nitrate	Monodentate Nitrate	Bidentate Nitrate	Bridging Nitrate
D_{3h}	C_{2v}	C_{2v}	C_{2v}

Scheme 4: Point group symmetries and different coordination schemes of NO_3^- ion.

Upon coordination, free nitrate ion lowers its point group symmetry from D_{3h} to $C_{2v,}$ which is accompanied by the splitting of doubly degenerate *E*'mode into non-degenerate A_1 and B_1; respectively. Of the six vibrational modes, A_1, B_1, B_2 are the only IR active modes [88].

1.7 Coordination Chemistry of Sulfate (SO_4^{2-}) Ion

Oxidation of SO_2(g) molecules on the metal oxide surfaces may form $BaSO_4$, K_2SO_4, and $Al_2(SO_4)_3$. Free sulfate ion, SO_4^{2-}, has the principal symmetry operators of *E*, C_3, C_2, σ_d, and S_4, generating the T_d symmetry point group. The stretching modes are A_1 (non-degenerate) and T_2 (triply degenerate). IR active irreducible representations of the free sulfate ion is T_2 mode. These vibrational modes are also represented as υ_1 and υ_3 having IR frequencies located at 980 and 1105 cm^{-1}[89]. However, only υ_3 modes (T_2) are IR active.

The SO_4^{2-} ion can coordinate to catalyst surfaces in the form of monodentate, tri-coordinated, bidentate and bridging sulfates as illustrated in Scheme 5.

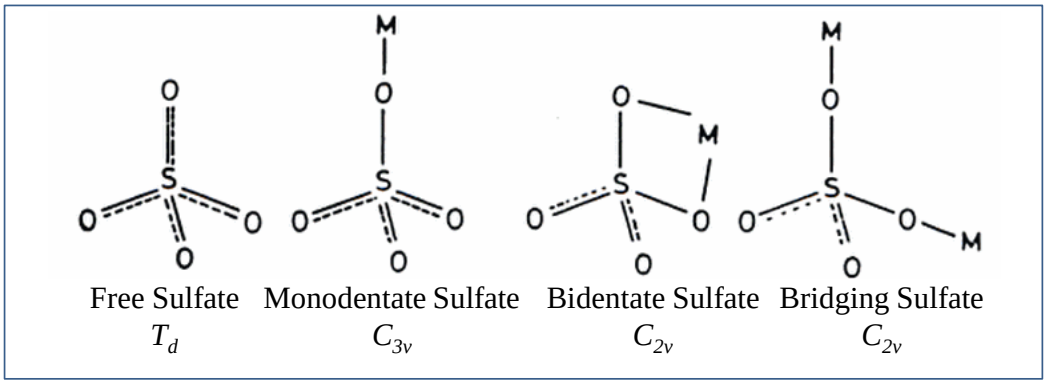

Scheme 5: Point group symmetries and different coordination of free sulfate ion.

Upon coordination in the form of monodentate sulfate, free sulfate ion lowers its symmetry from T_d to C_{3v}along with the splitting of the triply degenerate T_2 mode into $A_1 + E$ modes; respectively. On the other hand, upon coordination in the form of bidentate and bridging sulfates, the symmetry is further lowered to C_{2v} and the doubly degenerate E' modes split into A_1 and B_2 modes [88].

Chapter 2

Experimental

2.1 Material Synthesis

2.1.1 Synthesis of Binary Oxide ZrO_2/TiO_2 Materials

The ZrO_2/TiO_2 binary oxides were synthesized using a conventional sol-gel method. For the synthesis of the binary oxides, zirconium (IV) propoxide (Sigma Aldrich, ACS Reagent, 70 wt. % in 1-propanol) and titanium (IV) isopropoxide (Sigma Aldrich, ACS Reagent, 97%) precursors were initially dissolved in 100 mL of 2-propanol (Sigma Aldrich, ACS Reagent >99.5%) and stirred for 40 min under ambient conditions. This step was followed by the drop-wise addition of 3 mL of 0.5 M nitric acid solution (Sigma Aldrich, ACS Reagent, 65%) in order to obtain a gel. In the binary oxide materials, the composition ratio of ZrO_2:TiO_2 was adjusted as 70:30 and 30:70 by mass and these materials will be abbreviated as ZT70 and ZT30 throughout the text; respectively. ZrO_2:TiO_2 mass ratio of 70:30 has been reported as the optimum composition for the highest NO_x removal ability and the highest tolerance against sulfur-poisoning [61]. Corresponding amounts of precursors were calculated in order to synthesize batches of 6 g of each catalyst. The amounts of precursors used during the synthesis of ZT70 were 15.27 mL and 6.86 mL of Zr- and Ti-precursors; respectively. On the other hand, the amounts of precursors used during the synthesis of ZT30 were 6.55 mL and 16.05 mL of Zr- and Ti-precursors; respectively.

2.1.2 Synthesis of Ternary Oxide $Al_2O_3/ZrO_2/TiO_2$ Materials

Similarly, the synthesis of the ternary oxide was carried out by mixing zirconium isopropoxide, titanium isopropoxide and aluminum sec-butoxide (Sigma Aldrich, ACS Reagent, 97%) followed by the addition of 100 mL of 2-propanol. Next, the slurry was stirred for 60 min under ambient conditions and gel formation was achieved by drop-wise addition of 9 mL of 0.5 M nitric acid solution. Finally, the materials were dried under ambient conditions for 48 h followed by calcination in air within 323-1173 K. Relative nominal compositions of the ternary oxide systems (i.e. $Al_2O_3/ZrO_2/TiO_2$) by mass were 50:35:15 and 50:15:30 [23]. These materials will be abbreviated as AZT70 and AZT30 throughout the text; respectively. Corresponding amounts of precursors were calculated in order to synthesize batches of 6 g of each catalyst. The amounts of precursors used during the synthesis of AZT70 were 14.94 g, 7.64 mL, and 3.44 mL of Al-, Zr-, and Ti-precursors; respectively.

2.1.3 Synthesis of $Pt/Al_2O_3/ZrO_2/TiO_2$ Materials

1 wt. % platinum-incorporated ternary oxide materials were synthesized by wetness impregnation method using a solution of $Pt(NH_3)_2(NO_2)_2$ (Aldrich, diamminedinitritoplatinum(II), 3.4 wt. % solution in dilute NH_3(aq)). Prior to the Pt addition, $Al_2O_3/ZrO_2/TiO_2$ were initially calcined in air at 973 K for 150 min in order to remove the organic functionalities in the precursors. Then, 50 mL of deionized water was added onto 3g of AZT support and stirred over 8 hours at *ca.* 340K. Finally, material was subsequently calcined in air at 973 K for nitrite/nitrate content elimination and structural stabilization. Corresponding amounts of precursors were

calculated in order to synthesize batches of 3 g of each catalyst. The amount of Pt-precursor used during the synthesis was 1.43 mL.

2.1.4 Synthesis of $Pt/BaO/Al_2O_3/ZrO_2/TiO_2$ Materials

Pt/BaO/AZT catalysts with 8 or 20 wt. % BaO loading (*i.e.* Pt/8BaO/AZT and Pt/20BaO/AZT; respectively) were prepared by wetness impregnation of $Al_2O_3/ZrO_2/TiO_2$ support (which was initially calcined at 973 K for 150 min) with an aqueous solution of barium nitrate ($Ba(NO_3)_2$, ACS Reagent, ≥99%, Riedel-de Häen, Germany). The amounts of barium nitrate reagent used for the synthesis of 3 g of Pt/8BaO/AZT and Pt/20BaO/AZT were 0.44 g and 1.28 g; respectively. Then, 50 mL of deionized water was added and stirred for 8 hours at *ca.* 340K. This step was followed by calcination at 873 K in air for 150 min to remove nitrate/nitrite content by thermal decomposition. Next, these materials, $BaO/Al_2O_3/ZrO_2/TiO_2$, were impregnated with the $Pt(NH_3)_2(NO_2)_2$ precursor depending on the mass of BaO/AZT structure in order to have 1 wt.% nominal precious metal loading. Finally, obtained samples were calcined in air at 973 K for structural stabilization as well as the elimination of nitrate/nitrite and organic functionalities. In the text, the synthesized ZrO_2/TiO_2, $Al_2O_3/ZrO_2/TiO_2$, $Pt/ZrO_2/TiO_2$, $Pt/Al_2O_3/ZrO_2/TiO_2$ samples will be abbreviated as ZT, AZT, Pt/ZT and Pt/AZT; respectively.

2.1.5 Synthesis of $Pt/K_2O/Al_2O_3/ZrO_2/TiO_2$ Materials

Similar to the BaO-based NSR/LNT materials, the K_2O-based catalysts were prepared by wetness impregnation as well. The $Pt/K_2O/Al_2O_3/ZrO_2/TiO_2$ catalysts with 2.7, 5.4 and 10.0 wt. % K_2O loading (*i.e.* $Pt/2.7K_2O/Al_2O_3/ZrO_2/TiO_2$, $Pt/5.4K_2O/Al_2O_3/ZrO_2/TiO_2$ and $Pt/5.4K_2O/Al_2O_3/ZrO_2/TiO_2$; respectively) were

prepared via impregnation of $Al_2O_3/ZrO_2/TiO_2$ support (which was initially calcined at 973 K for 150 min) with an aqueous solution of potassium nitrate ($KNO_3 \cdot 6H_2O$, >99.0%, Fluka, France). The amounts of potassium nitrate reagent used for the synthesis of 3 g of $Pt/2.7K_2O/AZT$, $Pt/5.4K_2O/AZT$, and $Pt/5.4K_2O/AZT$ were 0.174 g, 0.347 g, and 0.644 g; respectively. Then, 50 mL of deionized water was added and stirred for 8 hours at *ca.* 340 K. This step was followed by calcination at 873 K in air for 150 min to remove nitrate/nitrite content by thermal decomposition. Finally, $K_2O/Al_2O_3/ZrO_2/TiO_2$ structure was impregnated with the $Pt(NH_3)_2(NO_2)_2$ precursor depending on the mass of K_2O/AZT structure in order to have 1 wt.% nominal precious metal loading and calcined at 973 K for 150 min under ambient conditions. Throughout the current text, synthesized Pt/ $K_2O/Al_2O_3/ZrO_2/TiO_2$ catalysts with 2.7, 5.4 and 10.0 wt.% K_2O loading will be abbreviated as $Pt/2.7K_2O/AZT$, $Pt/5.4K_2O/AZT$ and $Pt/5.4K_2O/AZT$; respectively.

2.1.6 Synthesis of Pt/BaO/γ-Al_2O_3 Materials

For the synthesis of the Pt/20BaO/Al benchmark catalyst, 2.4 g of γ-Al_2O_3 support (*i.e.* SASOL Puralox, 210 m^2/g) was impregnated with an aqueous solution of 1.02 g of barium nitrate ($Ba(NO_3)_2$,ACS Reagent, ≥99%, Riedel-de Häen, Germany). Then, 50 mL of deionized water was added and stirred for 8 hours at *ca.* 340 K. This step was followed by calcination at 873 K in air for 150 min. Finally, $20BaO/Al_2O_3$ was impregnated with the $Pt(NH_3)_2(NO_2)_2$precursor (Aldrich, diammine dinitritoplatinum(II), 3.4 wt.% solution in dilute NH_3(aq)) to obtain 1 wt. % nominal precious metal loading, followed by calcination at 973 K for 150 min.

Catalysts and their abbreviations together with the nominal mass percentiles of particular components are listed in Table 3.

Materials	Abbreviations	wt. % Pt	wt. % BaO	wt. % K_2O	wt. % AZT
$Al_2O_3/ZrO_2/TiO_2$	AZT	0	0	0	100
$Pt/Al_2O_3/ZrO_2/TiO_2$	Pt/AZT	1	0	0	99
$Pt/8BaO/Al_2O_3/ZrO_2/TiO_2$	Pt/8BaO/AZT	1	8	0	91
$Pt/20BaO/Al_2O_3/ZrO_2/TiO_2$	Pt/20BaO/AZT	1	20	0	79
$Pt/2.7K_2O/Al_2O_3/ZrO_2/TiO_2$	$Pt/2.7K_2O$/AZT	1	0	2.7	96.3
$Pt/5.4K_2O/Al_2O_3/ZrO_2/TiO_2$	$Pt/5.4K_2O$/AZT	1	0	5.4	93.6
$Pt/10K_2O/Al_2O_3/ZrO_2/TiO_2$	$Pt/10K_2O$/AZT	1	0	10	89

Table 3: Nominal loadings of the individual components in the synthesized catalysts.

2.2 Instrumentation:

2.2.1 Experimental Setup

The IR spectroscopic measurements were carried in transmission mode in a batch-type spectroscopic reactor. FTIR spectrometer (Bruker Tensor 27) and customized batch mode catalytic reactor is combined with a quadruple mass spectrometer (QMS, Stanford Research Systems, RGA 200) for temperature programmed desorption (TPD) and residual gas analysis (RGA) experiments as illustrated in Scheme 6.

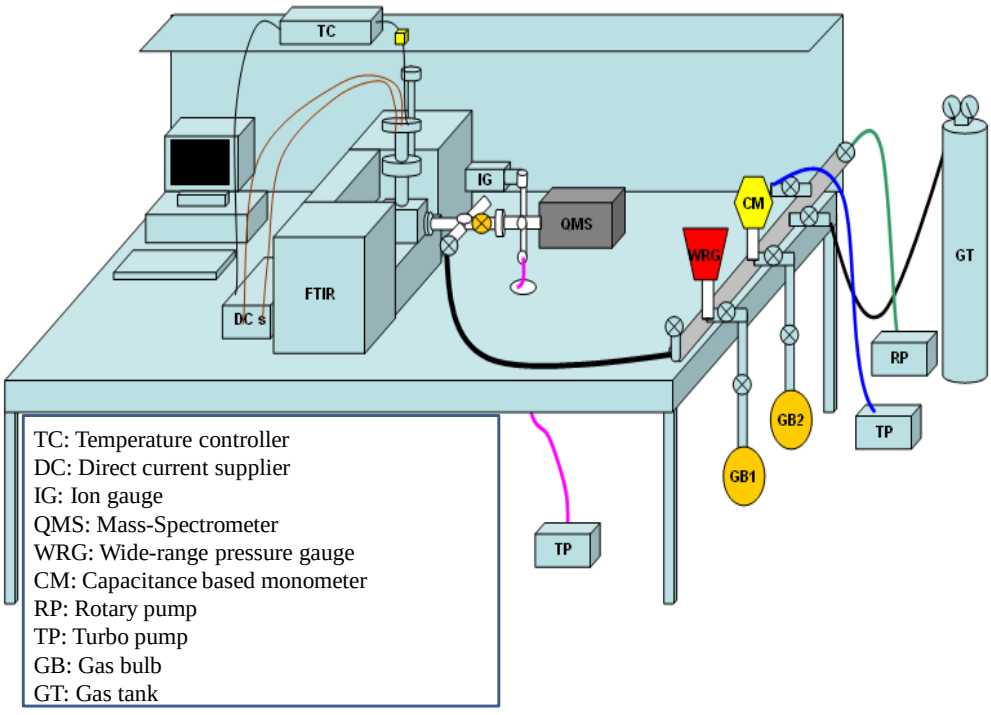

Scheme 6: Schematics of the *in-situ* FTIR and TPD experimental setup [90].

In-situ FTIR data were collected using a high sensitivity Hg-Cd-Te (MCT) mid-IR (MIR) detector operating via liquid nitrogen (LN_2) cooling at 77 K. Each spectrum was obtained by averaging 128 scans with a 4 cm^{-1} spectral resolution.

Powder samples were pressed onto a high conductance and lithographically-etched tungsten grid (TechEtch, USA, P/N PW10379-003) by applying ~3 tons of pressure. W-grid is attached to copper sample holder legs mounted to an electrical vacuum feedthrough. Sample pressed onto W-grid can be linearly heated in vacuum as well as in the presence of gas mixtures between 300 - 1173 K via adjustable DC power supply and a computer-controlled PID controller (Gefran 600-DRRR). In order to monitor the temperature, a K-type thermocouple (chromel and alumel having thickness of 0.015", Omega Engineering, Inc.) was spot-welded onto a tantalum foil which was attached on the W-grid.

Prior to the experiments, the samples were mounted into batch-mode customized reactor and outgassed at 403 K for *ca.* 12 h together while baking the reactor walls in order to get rid of water on the catalyst surfaces as well as on the reactor walls.

2.2.2 Characterization Techniques

Bulk/surface properties of the synthesized powder materials were investigated by means of a multitude of characterization techniques. In this section, we will highlight some of the primary fundamental aspects of these experimental methods.

2.2.2.1 X-ray Diffraction (XRD) Patterns

X-ray diffraction (XRD) is one of the most common techniques in structural characterization of heterogeneous catalysts, allowing the identification of crystalline phases and average particle sizes. X-ray diffraction originates from the elastic scattering of X-ray photons from lattice planes and a constructive interference of the scattered photons via Bragg's Equation:

$$n\lambda = 2d \sin\theta \qquad 2.1$$

where: 'λ' is the wavelength of the X-rays; 'd' is the distance between the repeating lattice planes; 'θ' is the angle between the incoming X-rays and the normal to the reflecting lattice plane and 'n' is the order of X-ray and positive integer.

Before the XRD measurements herein, powder samples were packed into a glass holder and the XRD patterns were collected using a Rigaku diffractometer, equipped with a Miniflex goniometer and an X-ray source (Cu$K\alpha$ radiation, at λ = 1.54 Å, 30 kV and 15 mA) The patterns were collected between 2θ = 10–80° with a scan rate of $2\ ^{\circ}\ \mathrm{min}^{-1}$.

2.2.2.2 Raman Spectroscopy

Raman spectroscopy is a vibrational spectroscopic technique which relies on the inelastic scattering of a monochromatic light. In this vibrational method, as the laser photon interacts with the material, various vibrational modes are excited to a virtual state upon deformation of the electrical field as a function of molecular polarizability. As the photons from the monochromatic laser are scattered by the sample, they lose (stokes Raman shift) or gain (anti-stokes Raman shift) energy during this excitation. This energy lost is considered as a change in wavelength of incident beam. This energy loss is characteristic for a particular bond in the Raman active modes.

The spectroscopic Raman analysis of the investigated materials were carried out by using a HORIBA Jobin Yvon LabRam HR 800 instrument. This instrument was equipped with a confocal Raman BX41 microscope, including a CCD detector. The Raman spectrometer has a Nd:YAG laser which had a wavelenght of λ = 532.1 nm. Throughout the Raman measurements, laser power was fine-tuned to 20 mW in

order to minimize the sample damage caused by sample heating. The diffraction grating of a spectrometer determines the wavelength range and the optical resolution. In our setup, the incident light source was dispersed by a holographic grating with a 600 grooves/mm. The groove frequency of the grating (1800 grooves/mm) determines the spectrometer's wavelength coverage and the spectral resolution. Incident laser beam was focused onto the sample by using a 50X objective.

Prior to analysis, calibration of the equipment has been made by calibration of the grating to 'zero' or using benchmark Si as the reference, 520.7 cm^{-1}. The powder samples were physically dispersed onto a single-crystal Si holder for the Raman measurements and all Raman spectra were acquired within 100-4000 cm^{-1} using an acquisition time of 100 s and a spectral resolution of 4 cm^{-1}. The confocal hole and the slit entrance were set at 1100 μm and 200 μm; respectively, in order to achieve optimum optical settings, which determine the quantity of incident photon flux.

2.2.2.3 BET Surface Area Analysis

Specific surface area measurements of the samples (which were initially dehydrated at 573 K for 2 h in vacuum) were determined by N_2 adsorption at 77 K via conventional 5-point BET (Brunauer, Emmett, and Teller) method by using a N_2 sorption analyzer (Micromeritics TriStar Surface Area and Porosity Analyzer).

2.2.2.4 FTIR Spectroscopy

Infrared spectroscopy is one of the most popular spectroscopic techniques used in catalysis research. Infrared radiation falls into three different categories depending on the IR photon frequency as illustrated in Table 4.

Region	Wavelength (μm)	Energy (meV)	Energy (meV)	Detection of
Far	1000-50	1.2-25	10-200	Lattice Vibrations
Mid	50-2.5	25-496	200-4000	Molecular Vibrations
Near	2.5-1	496-1240	4000-10000	Overtones

Table 4: Classification of Infrared Radiation Frequencies [91]

While lattice vibrations fall into 'Far' infrared range, molecular vibrations and overtones fall into 'Mid' and 'Near' infrared regions; respectively. There are various types of IR spectroscopic acquisition/excitation methods as demonstrated in Figure 2. Transmission IR spectroscopy is one of the most commonly used techniques among others.

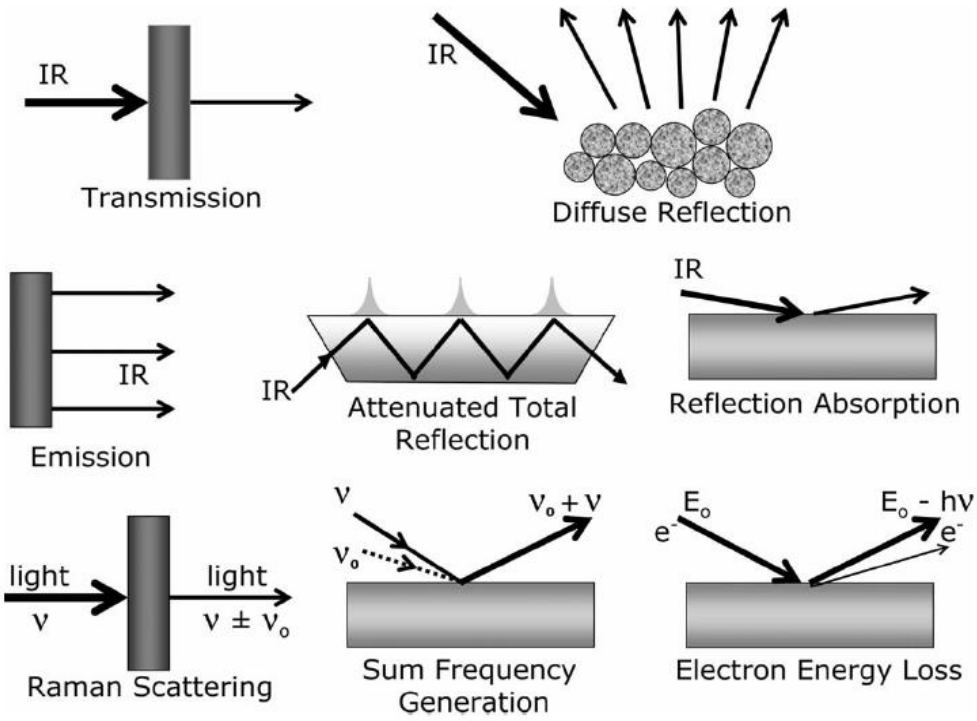

Figure 2: Types of Infrared Spectroscopy. Copyright Wiley-VCH Verlag GmbH & Co. [91]

Vibrational and rotational energy levels are discrete in a molecule. Transitions in between these energy levels take place upon absorption of photons

with frequency in the MIR range. Vibrational potential energy in a chemical oscillator can be approximated using the harmonic oscillator. This model is acceptable for small deviations around the equilibrium distance where the corresponding energies are given by equation 2.2:

$$E = \frac{1}{2}k(r - r_0)^2 \qquad 2.2$$

Here, k is force constant and r_o is equilibrium internuclear distance. This equation implies that the potential energy symmetrically increases irrespective of the distance between two atoms.

In classical mechanics, vibration frequency of a diatomic molecule can be expressed in equation 2.3:

$$v_{vib} = \frac{1}{2\pi}\sqrt{\frac{k}{\mu}} \qquad 2.3$$

where 'μ' is reduced mass and equals to (m_1.m_2)/(m_1+m_2). This equation indicates that the vibrational frequency of the harmonic oscillator increases linearly with the square root of the force constant and inverse of the square root of the reduced mass.

On the other hand, unlike in classical harmonic oscillator, vibrational energies in a molecule are quantized and expressed via the following equation corresponding to a quantum mechanical oscillator:

$$E = \left(n + \frac{1}{2}\right) + h\upsilon \qquad 2.4$$

where '*n*' is an integer (*i.e.* vibrational quantum number). The lowest vibrational energy is equal to E = ½hν for n=0 which is also called the zero-point energy. The relationship between quantized energy levels and distance for a quantum mechanical harmonic oscillator is illustrated in Figure 3.

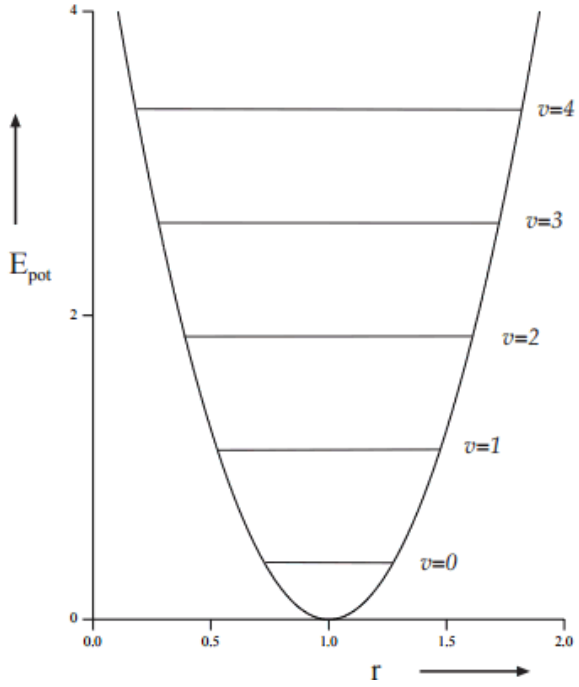

Figure 3: Potential energy change as a function of the interatomic distance in a harmonic oscillator.

It should be noted that, molecules do not exactly behave like two masses connected by a spring as described by a harmonic oscillator and can be modelled more successfully using an anharmonic oscillator model. This anharmonic oscillator model also allows bonds to be broken upon stretching beyond a limiting distance. Morse potential can be utilized to mathematically define an anharmonic oscillator potential:

$$V(r) = D\left(1 - e^{-a(r-r_0)}\right)^2 - D \qquad 2.5$$

where '*r*' is the interatomic distance, '*r*' is the equilibrium separation, '*D*' is the bond dissociation energy and '*a*' is a parameter associated with the steepness or depth of the potential well [91].

In this potential, energy levels are no longer equidistant and overtones become allowed as illustrated in Figure 4.

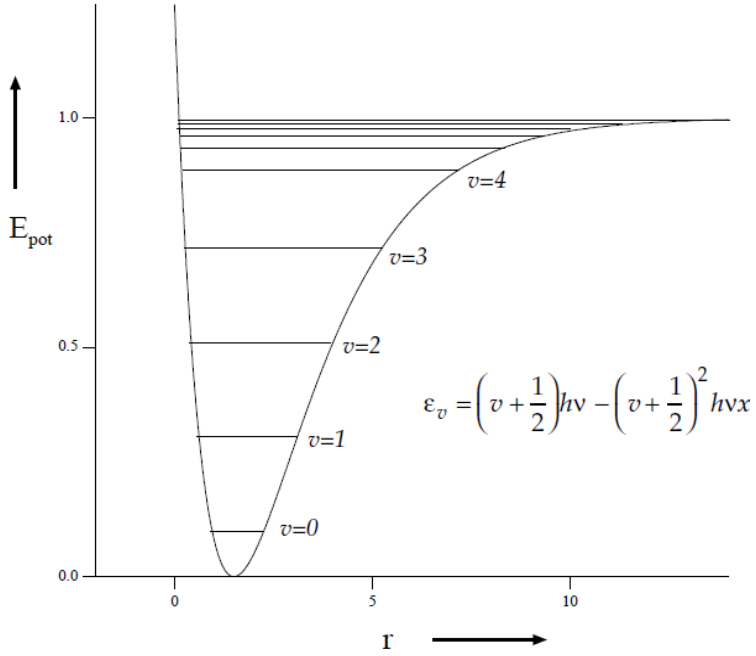

Figure 4: Potential energy change as a function of interatomic distance in anharmonic oscillator.

2.2.2.5 Temperature Programmed Desorption (TPD)

TPD is another commonly used technique in heterogeneous catalyst investigations where desorbing gas molecules from single or polycrystalline samples are collected by a mass spectrometer. In the typical TPD analysis of powder catalysts, the sample is heated with a linear ramp rate of 5-30 K/min and

concentrations of desorbing species are analyzed *via* a quadrupole mass spectrometer (QMS). Heating rate plays a significant role in the characteristics of the desorption line shape. As the heating rate increases, peak width of the desorption signals become narrower. Moreover, pumping speed is also an important parameter. Pumping of the desorbing species should be sufficiently rapid in order to prevent re-adsorption of the gas phase species back to the catalyst surface. Low pumping speeds cause a broadening of the desorption lines towards higher temperatures. Finally, mass spectrometer should be mounted directly in front of the catalyst. A typical schematic illustration of a conventional TPD set-up is demonstrated in Figure 5.

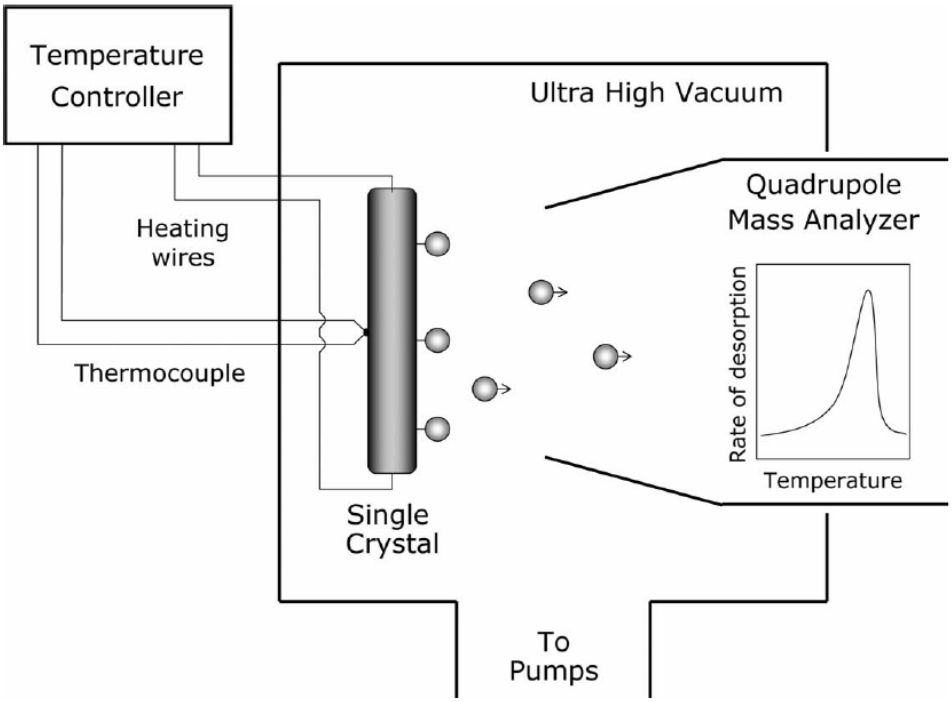

Figure 5: Experimental Setup for TPD Experiments. Copyright Wiley-VCH Verlag GmbH & Co.[91].

2.2.3 Experimental Procedures

2.2.3.1 NO_x adsorption *via* FTIR

NO_2(g) was prepared by mixing NO(g) (Air Products, 99.9%) and excess O_2(g) (Linde GmbH, Germany, 99.999%). Freeze-thaw-pump cycles were applied for the removal of contaminations and unreacted gases in NO_2(g). Before the FTIR experiments, material surfaces were initially flushed with 1.0 Torr of NO_2(g) for 5 min and subsequently annealed to 973 K with a 12 K/min heating rate under vacuum. Then, for the FTIR analysis, material surfaces were exposed to NO_2(g) at 323 K in a stepwise fashion from low to higher pressures where each exposure (0.1 torr) took 1 min. Finally, a surface saturation was achieved by the introduction of 5.0 Torr NO_2(g) over the samples for 10 min at 323 K followed by evacuation to a pressure lower than 10^{-2} Torr.

2.2.3.2 NO_x Desorption and Reduction *via* FTIR

Nitrate reduction experiments for the Pt-free materials were carried out by exposing the NO_2(g)-saturated material surface to 15.0 Torr of H_2(g) (Linde GmbH, Germany, >99.9%) at 323 K, followed by gradual heating at a constant rate of 12 K/min until a desired temperature. For the Pt-containing materials, 15.0 Torr of H_2(g) was introduced over the NO_2-saturated material at 323 K and the time-dependent FTIR spectra were acquired for 2 h. After 2 h of reduction at 323 K, sample was heated to 473 K in the presence of H_2(g) for the complete reduction and removal of adsorbed NO_x. All of the FTIR spectra given in this study were obtained at 323 K.

2.2.3.3 SO_x adsorption *via* FTIR

Sulfur adsorption/poisoning characteristics of each material was investigated by exposing the catalyst surfaces to a 2.0 Torr SO_2+O_2 gas mixture (SO_2:O_2 = 1:10) at 323 K (SO_2 purity >99%, Air Products, O_2 purity > 99.999%, Linde GmbH). After the introduction of SO_x mixture at 323 K, samples were annealed to different temperatures, such as 373, 473, 573 and 673 K for 5 min. FTIR spectra of these sulfated surfaces were acquired after cooling to 323 K in the presence of the gas mixture. After the acquisition of the FTIR spectra for the annealing at 673 K, SO_x mixture in the reactor was evacuated to a pressure lower than 10^{-3} Torr. Here, it should be specified that the concentration of SO_2 content in 2.0 Torr SO_2+O_2 gas mixture is roughly equal to 270 ppm which is significantly higher compared to the sulfur content (15 ppm) in Ultra Low Sulfur Diesel (ULSD). Therefore, sulfur poisoning experiments performed herein correspond to severe and accelerated poisoning experiment where the catalysts can reveal their utmost sulfur uptake and release characteristics.

2.2.3.4 SO_x desorption *via* FTIR

Prior to SO_x desorption experiments, materials were sulfated as mentioned above by collecting a series of spectra in the presence of the aforementioned SO_x mixture as a function of temperature until 673 K. After the sulfur poisoning, gases in the reactor were evacuated to a pressure lower than 10^{-2} Torr, followed by the introduction of 15.0 Torr of H_2(g) (H_2 purity > 99.999%, Linde GmbH) at 323 K. Subsequently, sulfated materials were annealed under hydrogen atmosphere at 473, 673, 773, 873 and 973 K for 5 min.

2.2.3.5 NO_x desorption *via* TPD

In NO_x-TPD experiments, each material was initially saturated by 5.0 Torr NO_2(g) for 10 min. After the saturation of the catalysts, gases in the reactor were evacuated to a pressure lower than 10^{-3} Torr. Subsequently, materials were heated in vacuum with a constant rate of 12 K/min to 973 K. In-situ FTIR spectra were acquired before and after TPD analysis.

2.2.3.6 SO_x desorption *via* TPD

In SO_x-TPD experiments, material surfaces were initially exposed to a 2.0 Torr SO_2+O_2 gas mixture (SO_2:O_2 = 1:10) at 673 K for 30 min. Then the IR spectroscopic reactor was evacuated to a pressure lower than 10^{-3} Torr followed by heating under vacuum to 1173 K with a linear heating rate of 12 K/min. In the TPD experiments, m/z= 32 (corresponding to O_2(g) desorption and S(g) formation due to the impact ionization-induced fragmentation of desorbed SO_2(g) species in QMS) and m/z = 64 (corresponding to SO_2(g) desorption) channels were monitored *via* QMS.

2.2.3.7 Pyridine Adsorption *via* FTIR

Pyridine adsorption experiments were carried out by vapor adsorption at 298 K for 15 min, followed by subsequent evacuation to a pressure less than $5x10^{-2}$ Torr in order eliminate gas phase and weakly adsorbed species. In these experiments, self-supported pellets on W-grids were used.

2.2.3.8 Ammonia Adsorption *via* TPD

In order to obtain a deeper understanding of the overall basicity of the Pt-based catalysts, NH_3-TPD measurements were performed in a Setaram Sensys DSC

(Digital Scanning Calorimeter). Two quartz tubes were mounted inside the DSC. In one tube, ca. 60 mg of catalyst powder was placed on a sintered plate, while the other tube was used as a reference. The outlet products were analyzed in the Hiden HPR-20 QUI Mass spectrometer. The total flow used in all experiments was 20 ml/min, which was taken from a larger gas flow and the excess gas was sent to the ventilation. Argon was used as an inert balance gas in all experiments. Catalysts were first de-greened at 923 K, followed by the same experimental de-greening procedure used in the flow reactor system. After de-greening, the catalysts were oxidized and reduced at 873 K by exposing their surfaces to 8% O_2 for 30 min and 0.9 % H_2 for 1 h; respectively. Argon was flushed through the reactor between these two steps. NH_3 TPD experiments were done after the pretreatment and the catalysts were exposed to 2000 ppm NH_3 at 323 K for 8 h. Then, the samples were treated with Argon for 30 min and the temperature was increased to 1073 K with a ramp rate of 5 °C/min under inert conditions.

2.2.3.9 Monolith Preparation for Flow Mode Catalytic Performance Tests

The cordierite monoliths were wash-coated with the calcined powder catalysts for the activity measurements in the flow reactor system. The monoliths (length = 20 mm, diameter = 21 mm and cell density of 400 cells per square inch, cpsi) were cut from a commercial honeycomb cordierite structure and calcined at 773 K for 2 h. Then, the monoliths were immersed into a slurry which consisted of a liquid phase (with equal volumes of distilled water and ethanol) and a solid phase (with 5 wt. % boehmite-Disperal D and 95 wt. % powder catalyst). The solid in the slurry was 20 wt. %. The excess liquid was gently blown away and the monolith was dried at 363 K for 2 min. The immersing, blowing away and drying were repeated

several times until the weight of washcoat was about 700 mg, corresponding to ~20 % w/w of the total monolith followed by their calcination at 823 K for 2 min in air. Finally, the washcoated monoliths were calcined at 873 K for 2 h.

2.2.3.10 Flow Reactor Measurements

NO_x storage capacities of the investigated materials were also quantitatively studied in detail using monolith samples in a flow reactor system. These experiments were carried out in a horizontally mounted quartz tube flow reactor heated by a heating wire controlled by a Eurotherm temperature-controller. The temperature of the reactor was measured and controlled by a thermocouple positioned about 10 mm in front of the monolith, while the catalyst temperature was measured by another thermocouple inserted in a center channel of the monolith. The inlet gas feed was regulated using several Bronkhorst mass flow controllers. The water in the form of steam was introduced into the reactor by a controlled evaporation and mixing system (Bronkhorst Hi-Tech). All lines were heated and maintained at 473 K in order to prevent water condensation. The effluent species from the reactor were analyzed by a gas phase FTIR spectrometer (MKS Instruments, MultiGas 2030) with the gas cell heated to 464 K. The total flow was varied between 3400 to 3500 ml/min during all experiments and argon was chosen as the carrier gas.

Cycling tests for fresh materials were consecutively performed at 673, 573 and 473 K (with a cooling step in between) in the presence of 4.7 % CO_2, 5 % H_2O and Ar. The cycling procedure included seven cycles of alternating lean and rich conditions where NO was dosed into the reactor system and four cycles of lean/rich conditions using NO_2 instead at each target temperature. During the lean step, the samples were exposed to the gas feed containing 480 ppm NO (or 430 ppm NO_2), 9

% O_2, 4.8 % CO_2, 5 % H_2O in Ar (with a duration of 4 min), while the rich conditions consists of 470 ppm NO (or 420 ppm NO_2), 0.9 % H_2, 4.8 % CO_2 and 5 % H_2O in Ar (with a duration of 1 min) as illustrated in Table 5. The results taken from the last two consecutive cycles are shown in the current text.

	Feed Mixture 1 (FM^1)	Feed Mixture 2 (FM^2)
Lean Mixture	480 ppm NO, 9 % O_2, 4.8 % CO_2, 5 % H_2O in Ar	430 ppm NO_2, 9 % O_2, 4.8 % CO_2, 5 % H_2O in Ar
Rich Mixture	470 ppm NO, 0.9 % H_2, 4.8 % CO_2, 5 % H_2O in Ar	420 ppm NO_2, 0.9 % H_2, 4.8 % CO_2, 5 % H_2O in Ar

Table 5: Gas concentrations for different feed mixtures

Chapter 3

Results and Discussion

3.1 Structural Characterization

3.1.1 X-Ray Diffraction Analysis

3.1.1.1 Binary Support Oxides

The XRD of ZrO_2/TiO_2 binary mixed oxides with the ZrO_2:TiO_2 mass ratios of 30:70 and 70:30 are shown in Figure 6a and 6b; respectively. As shown in Figure 6, the amorphous structure of ZrO_2/TiO_2 binary oxide persists up to 773 K irrespective of ZrO_2:TiO_2 mass ratios. This trend in structural evolution as a function of temperature was followed by sudden crystallization at a temperature higher than 773 K.

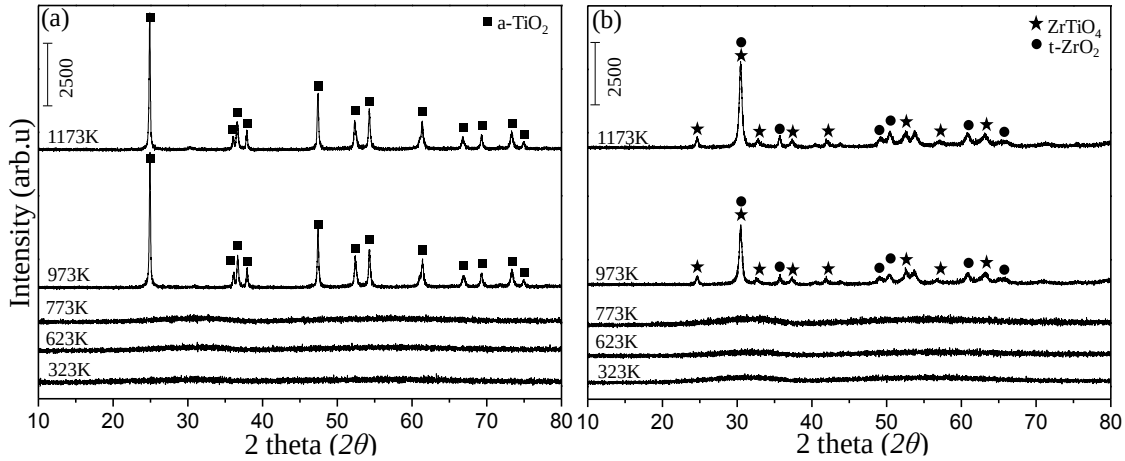

Figure 6: XRD patterns corresponding to (a) ZT30 and (b) ZT70 binary oxide materials as a function of calcination temperature within 323 and 1173 K.

In Figure 6a, it is observed that TiO_2 anatase (JCPDS 21-1272) is the majority structure of crystalline phase in ZT30 at 973 K and 1173 K. On the other hand, structural evolution of ZT70 shown in Figure 6b suggests that the crystallization

takes place quite differently on ZT70, indicating crystalline phases of tetragonal ZrO_2 (JCPDS 80-2155) and $ZrTiO_4$ (JCPDS 34-415) above 773 K. It is worth mentioning that XRD analysis was also performed to investigate the effect of Pt impregnation, where it was observed that Pt did not lead to major crystallographic changes over the ZT30 and ZT70 systems (data not shown here) besides the presence of diffraction signals associated with metallic Pt particles (JCPDS 001-1190).

3.1.1.2 Ternary Support Oxides:

Structural evolution of $Al_2O_3/ZrO_2/TiO_2$ ternary mixed oxides as a function of temperature is also followed using X-ray diffractometer. Figure 7a and Figure 7b illustrate the XRD patterns of ternary oxide systems corresponding to AZT30 and AZT70; respectively.

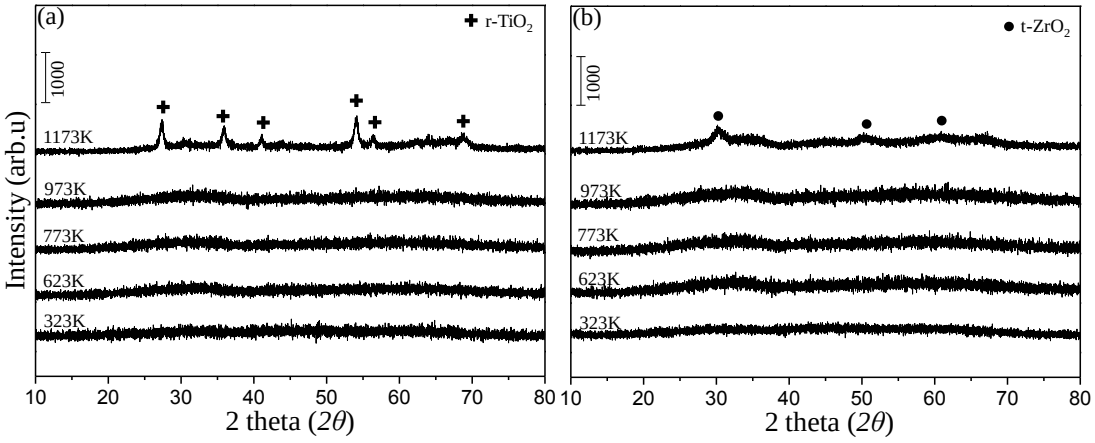

Figure 7: XRD patterns corresponding to (a) AZT30 and (b) AZT70 ternary oxide materials as a function of calcination temperature within 323 and 1173K.

The synthesized ternary oxides have a different behaviour compared to the binary oxide ZrO_2/TiO_2. AZT preserved its amorphous nature up to 973 K without revealing any well-resolved diffraction lines. However, these materials start to exhibit poorly discernible diffraction signals at 1173 K. While these diffraction lines

are corresponding to rutile phase of TiO_2 in the AZT30, the major crystallographic phase was observed to be tetragonal ZrO_2 (JCPDS (80-2155) in the AZT70 material. Along these lines, it can be concluded that presence of Al_2O_3 phase elevates crystallization temperature up to 1173 K, hindering the formation of undesired $ZrTiO_4$ phase with low SSA. It is worth mentioning that XRD patterns were also collected from the Pt/ZT30, Pt/ZT70, Pt/AZT30 and Pt/AZT70 materials, where the Pt addition did not lead to a major crystallographic change over the ZT and AZT materials, besides the presence of diffraction signals associated with the metallic Pt particles.

3.1.1.3 Pt-supported NSR/LNT Catalysts

After the structural analysis of the support materials, we further investigated the LNT catalysts functionalized with storage component (*i.e.* BaO) and precious metal (*i.e.* Pt).

Figure 8 illustrates the XRD patterns of Pt/AZT, Pt/8BaO/AZT, Pt/20BaO/AZT, Pt/20BaO/Al and Pt/20BaO/ZT recorded after calcination at 973 K for 150 min. The Pt/AZT catalyst, in Figure 8, exhibits highly amorphous characteristics except the presence of structurally well-ordered metallic platinum (JCPDS 001-1190). Incorporation of 8 wt. % BaO does not reveal any additional phases except the attenuation of the platinum diffraction features. This trend is also observable for the catalyst with a higher BaO loading, *i.e.* Pt/20BaO/AZT. It is likely that the presence of BaO domains on AZT support hinders the precious metal sintering and facilitates the metal dispersion.

XRD pattern of the benchmark NSR/LNT catalyst (*i.e.* $Pt/20BaO/Al_2O_3$) was also collected that reveals γ-Al_2O_3 (JCPDS 001-1303), $BaAl_2O_4$ (JCPDS 017-0306)

and metallic Pt (JCPDS 001-1190) features. On the Pt/20BaO/Al_2O_3 catalyst, the BaO domains interact with the γ-Al_2O_3 support at elevated temperatures yielding the formation of undesired $BaAl_2O_4$ phase and thermal aging [2–4]. On the other hand, such a phase is not visible in the AZT containing samples (Figure 8). The Pt/20BaO/ZT material reveals various discernible diffraction signals, namely t-ZrO_2 (JCPDS 80-2155), $ZrTiO_4$ (JCPDS 34-415) and $BaTiO_3$ (JCPDS 34-0129). In the light of these findings, it is apparent that alumina acts as a diffusion barrier between BaO and TiO_2 and ZrO_2 domains hindering the formation of $BaTiO_3$, $ZrTiO_4$ and other crystalline phases on the Pt/20BaO/AZT catalyst.

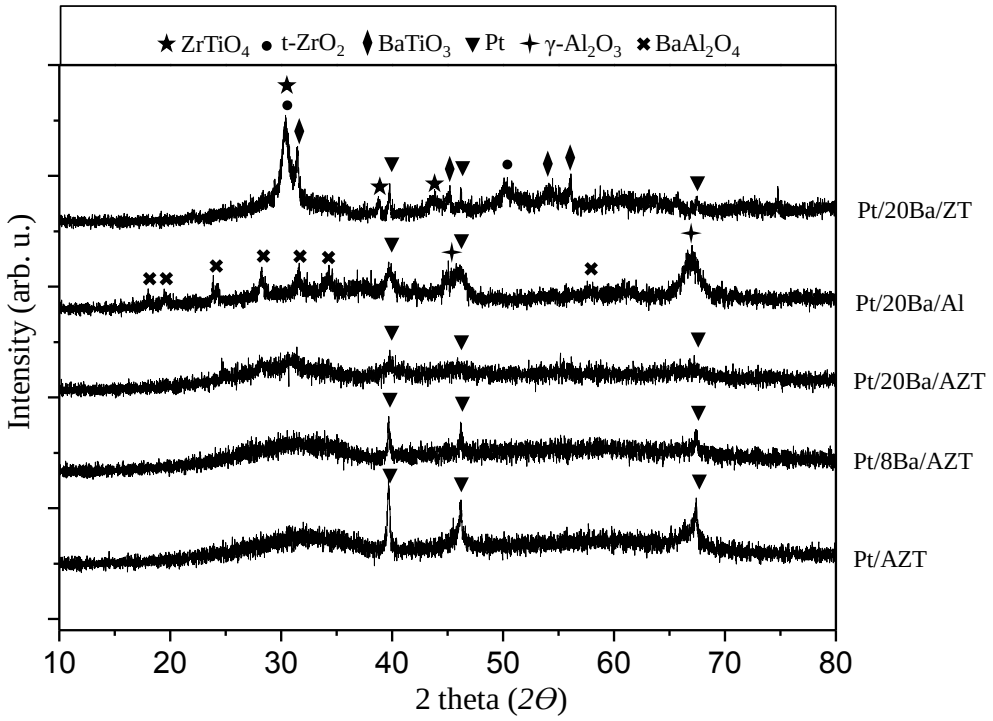

Figure 8: XRD patterns corresponding to Pt/AZT, Pt/8BaO/AZT, Pt/20BaOAZT, Pt/20BaO/Al and Pt/20BaO/ZTmaterials upon calcination at 973 K.

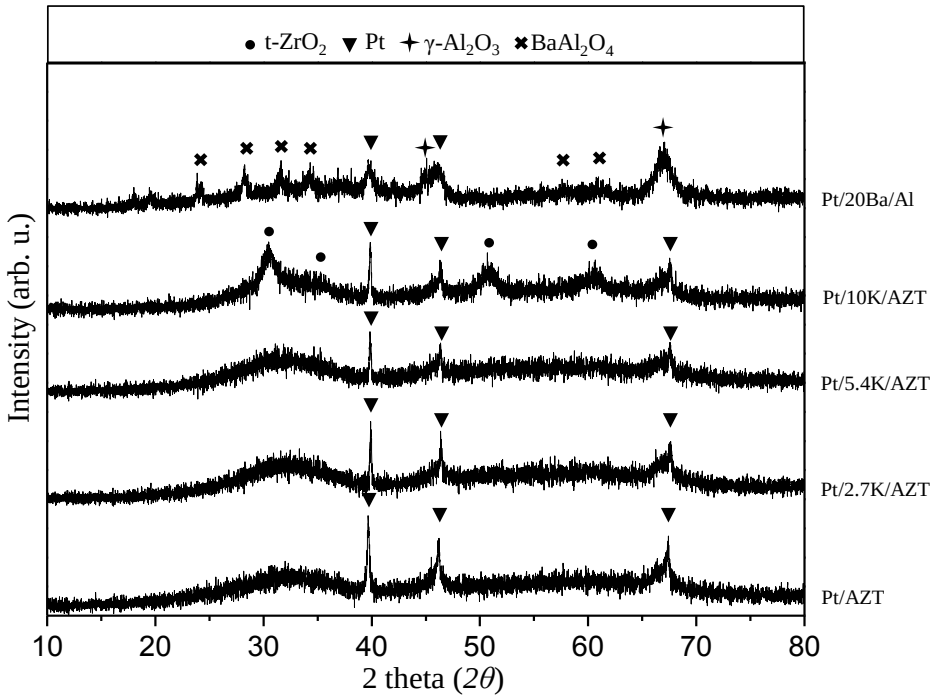

Figure 9: XRD patterns corresponding to Pt/AZT, Pt/2.7K_2O/AZT, Pt/5.4K_2O/AZT, Pt/10K_2O/AZT and Pt/20BaO/Almaterials upon calcination at 973 K.

AZT materials were further functionalized with other oxides (*i.e.* K_2O) and their structural characteristics were investigated by means of XRD analysis. Figure 9 illustrates the XRD patterns of Pt/AZT, Pt/2.7K_2O/AZT, Pt/5.4K_2O/AZT, Pt/10K_2O/AZT and Pt/20BaO/Al collected after calcination at 973 K for 150 min. Except the presence of structurally well-ordered metallic platinum (JCPDS 001-1190), Pt/AZT catalyst in Figure 9 exhibits highly amorphous features. Materials, containing 2.7 and 5.4 wt. % K_2O (*i.e.* Pt/2.7K_2O/AZT and Pt/5.4K_2O/AZT) do not reveal any additional phases except the slight attenuation of the platinum diffraction features.

On the other hand, the material with 10.0 wt. % K_2O (*i.e.* Pt/10.0K_2O/AZT) revealed additional poorly discernible diffraction lines at 2θ=30.48^o, 50.50^o, 60.91^o

corresponding to tetragonal ZrO_2 (JCPDS 80-2155) together with the further suppression of Pt diffraction features.

Average Pt particle sizes for Pt/AZT, Pt/8BaO/AZT/, Pt/20BaO/AZT, and Pt/20BaO/Al were estimated using Schrerrer equation and found to be 34 nm, 31 nm, 10 nm, 12 nm; respectively.

3.1.2 Raman Spectroscopy

3.1.2.1 Binary Oxide Materials

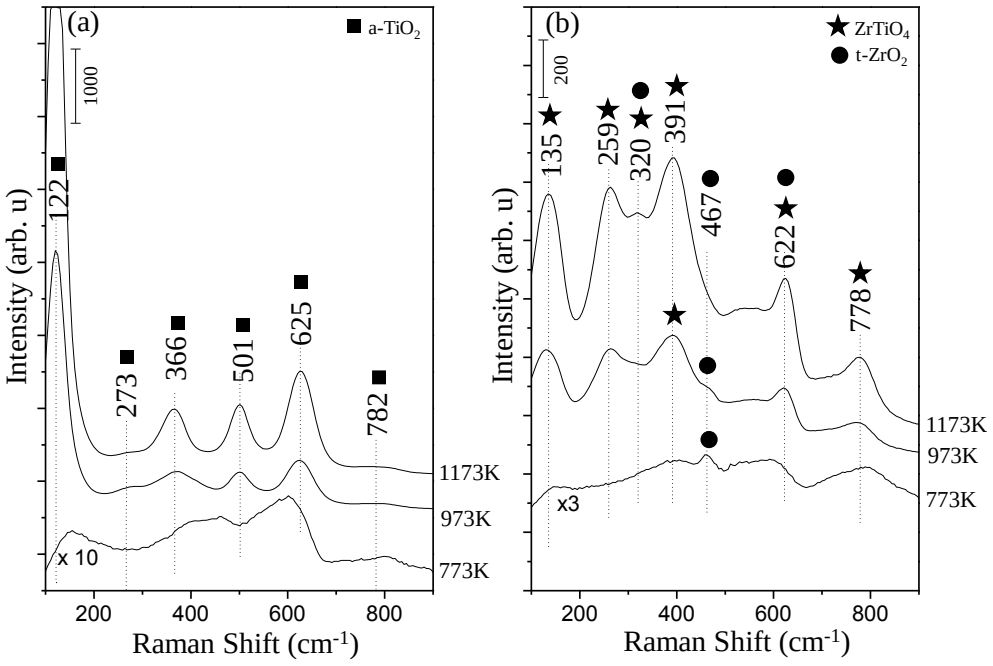

Figure 10: Ex-situ Raman spectra corresponding to (a) ZT30 and (b) ZT70 materials upon calcination at temperatures within 773-1173 K.

Structural evolution of binary (ZrO_2/TiO_2) mixed oxides as a function of temperature and composition were further investigated by using a Raman spectrometer. The temperature-dependent Raman spectra of ZT30 and ZT70 are illustrated in Figure 10a and 10b; respectively. It should be noted that Raman spectra corresponding to materials calcined at temperatures lower than 773K do not exhibit

such features due to poor crystallinity as illustrated in XRD section (Figure 6). ZT30 sample exhibits only six vibrational peaks at 122, 273, 366, 501, 625 and 782 cm^{-1} at temperatures 973 and 1173K as shown in Figure 10a. These features can be readily assigned to the anatase phase of TiO_2 domains [92], [93]. However, ZT70 material shows completely different structural characteristics at all temperatures. While the vibrational features at 135, 259, 320, 391, 622 and 778 cm^{-1} indicate the formation of $ZrTiO_4$ phase, features *ca.* 320, 467 and 622 cm^{-1} can be most likely correlated by the presence of tetragonal ZrO_2 phase. $ZrTiO_4$, one of the main crystalline phases detected for ZT70 sample is known in the literature to have an orthorhombic symmetry with a *Pbcn* space group and a*mmm* point group. This phase has 33 optically active modes and 18 of which are Raman active [92], [93]. However, in the Raman data corresponding to the ZT70 sample presented in Figure 10b, only six of these vibrational features are discernible. This can be associated with the band broadening and signal overlap due to the random distribution of Zr^{4+} and Ti^{4+} ions in the crystal lattice[92], [93].

3.1.2.2 Ternary Oxide Materials:

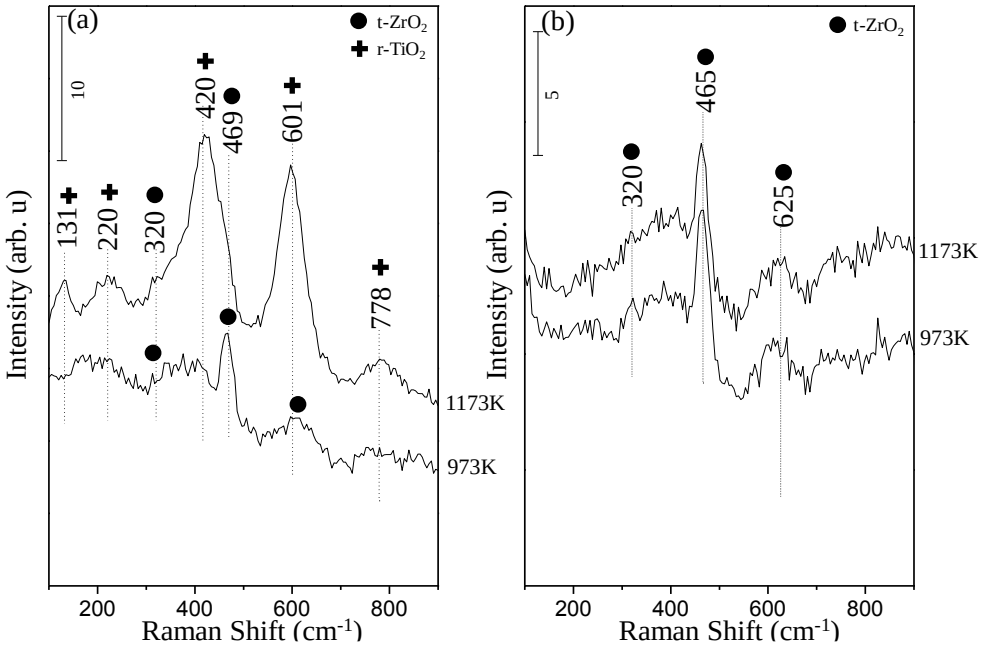

Figure 11: Ex-situ Raman spectra corresponding to (a) AZT30 and (b) AZT70 materials upon calcination at temperatures within 973-1173 K.

Structural evolution of ternary oxides as a function of temperature and composition was investigated by means of Raman spectroscopy as well. The temperature-dependent Raman spectra of AZT30 and AZT70 samples are illustrated in Figure 11a and 11b; respectively. As compared to the ZT30 and ZT70 binary oxides, Raman spectra corresponding to the AZT ternary oxide materials revealed much weaker signals due to the poor crystallinity, as already stated *via* XRD analysis. In Figure 11a, AZT30 revealed seven different weak Raman features, at 1173 K, located at 132, 220, 320, 420, 469, 601 and 778 cm^{-1}. While the features at 131, 220, 420 and 601 cm^{-1} can be attributed to the rutile TiO_2 phase, very weak shoulders at 320 and 469 cm^{-1} are most likely related to tetragonal ZrO_2 phase. On the other hand, there are only three features observed at 320, 465 and 625 cm-1 for

AZT70, indicating the formation of tetragonal ZrO_2 phase AZT70 material as demonstrated in Figure 11b. This reveals that besides the tetragonal ZrO_2 phase, XRD and Raman data do not provide any clear indications for the presence of additional ordered phases in the AZT system, such as $ZrTiO_4$. These observations are in line with studies reported by Escobar *et al.*[94] who suggested that in the ZT binary system ZrO_2 can provide Zr^{4+} ions which may diffuse into the TiO_2 lattice in the absence of aluminum oxide, forming $ZrTiO_4$. However, in the AZT ternary systems, XRD and Raman data given in Figures 2 and 5 suggest that the Al_2O_3 layer acts as a diffusion barrier preventing diffusion of Zr^{4+} ions in to the TiO_2 lattice, preventing the ordering of the crystal lattice and the formation $ZrTiO_4$.

3.1.3 BET Specific Surface Area (SSA) Analysis

3.1.3.1 Binary Oxide Materials

BET specific surface area values for the synthesized binary oxide materials which were calcined at 773, 973 and 1173 K for 150 minutes were illustrated in Figure 12a. SSA values of ZT30 were found to be 97, 10 and 1 m^2/g at 773, 973 and 1173 K; respectively. On the other hand, these SSA values are relatively higher (*i.e.* 177, 26 and 3 m^2/g) for the ZT70 counterpart at the corresponding temperatures; respectively. Temperature-dependent changes in SSA values clearly indicate that calcination at 973 K causes drastic change in structural characteristics. This structural behavior in binary oxide materials can also be explained by the XRD and Raman results, indicating a sudden phase transformation from an amorphous to a crystalline structure. Furthermore, materials were observed to alter their morphology at 1173 K due to thermal aging and particle agglomeration.

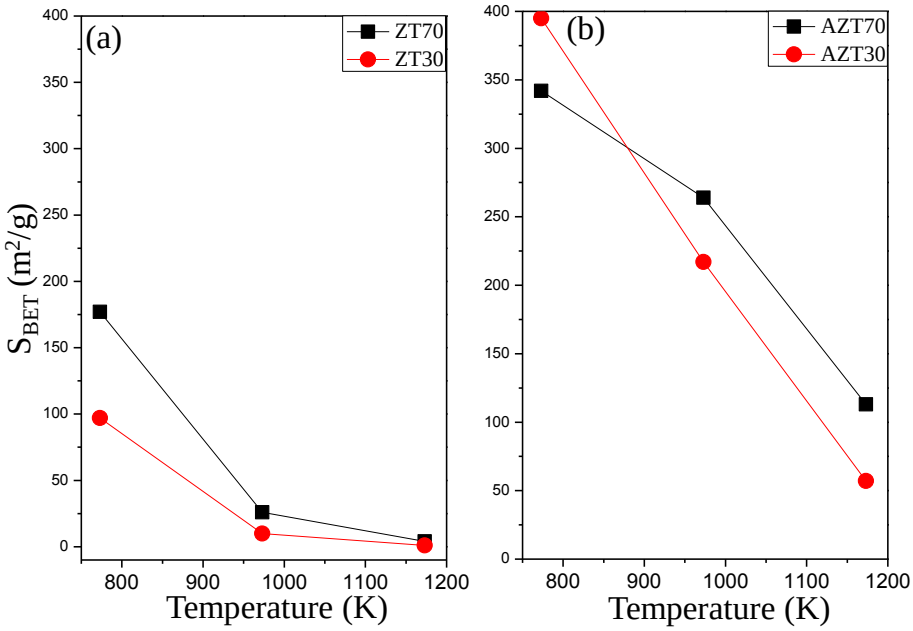

Figure 12: Specific surface area (SSA) values corresponding to (a) binary and (b) ternary materials upon calcination at temperatures within 773-1173 K.

3.1.3.2 Ternary Oxide Materials

Figure 12b presents BET specific surface area (SSA) values for the synthesized ternary oxide materials which were calcined at 773, 973 and 1173 K for 150 minutes. While SSA values for AZT30 were found as 395, 217 and 57 m^2/g at the corresponding temperatures, values regarding AZT70 were observed to be 342, 264 and 113 m^2/g; respetively. Figure 12 indicates that the AZT ternary oxide systems have much higher surface area compared to the ZT binary oxide systems for all calcination temperatures. These results are in perfect agreement with the XRD and Raman results as mentioned in previous sections, suggesting a more disordered structure for the ternary AZT systems. Crystallization of the ZT binary oxide leads to relatively ordered and larger particles at 973 K, while the ternary system preserves its rather amorphous structure and small particle size even at 1173 K.

3.1.3.3 Pt-supported NSR/LNT Catalysts

In this section, SSA values related to different NSR/LNT materials functionalized with a storage component (*i.e.* BaO or K_2O) and precious metal sites (*i.e.* Pt) were analyzed. Figure 13 illustrates specific SSA values of Pt/AZT, Pt/8BaO/AZT, Pt/20BaO/AZT, Pt/20BaO/Al_2O_3 and Pt/20BaO/ZT catalysts. It was found that SSA values of Pt/8BaO/AZT (152 m^2/g) and Pt/20BaO/AZT (132 m^2/g) catalyst are rather comparable to that of the benchmark Pt/20BaO/Al catalyst (134 m^2/g). On the other hand Pt/AZT has a slightly higher SSA (191 m^2/g) which resembles to that of AZT support material (230 m^2/g) due to lack of BaO storage component. This decrease from 230 to 191 m2/g can be correlated by the partial filling of AZT pores with Pt particles. Moreover, since Pt was impregnated in an aqueous solution, water and calcination after Pt addition may lead to further sintering.

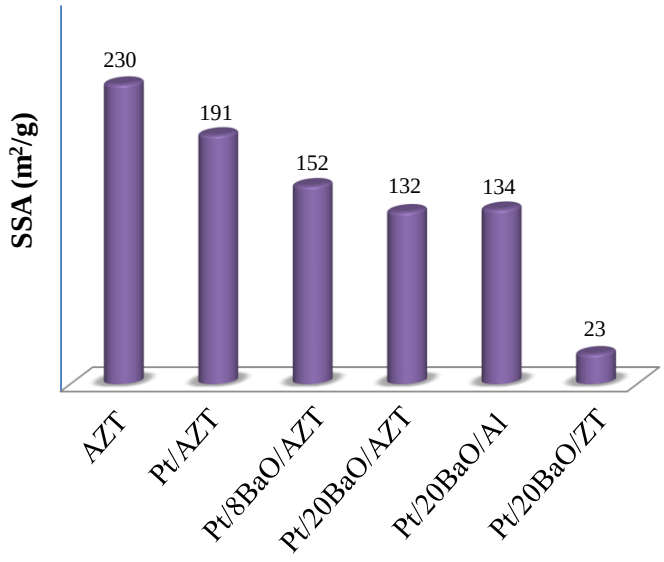

Figure 13: BET specific surface area values for BaO-supported materials after calcination at 973 K for 150 min.

In the absence of the Al_2O_3 component (*i.e.* for the Pt/20BaO/ZT catalyst), the SSA values was found to be significantly lower (23 m^2/g).

In another set of samples, AZT ternary support oxides are enriched by K_2O storage components together with the Pt metals. Figure 14 illustrates SSA values of Pt/AZT, Pt/2.7K_2O/AZT, Pt/5.4K_2O/AZT, Pt/10K_2O/AZT and Pt/20BaO/Al catalysts. These results clearly show that Pt/5.4K_2O/AZT (155 m^2/g) has almost an identical SSA value to that of Pt/8BaO/AZT (152 m^2/g) which is relatively lower than that of Pt/2.7K_2O/AZT (177 m^2/g). Moreover, increase in K_2O loading from 5.4 to 10 wt. % decreases the SSA value of catalysts from 155 to 125 m^2/g.

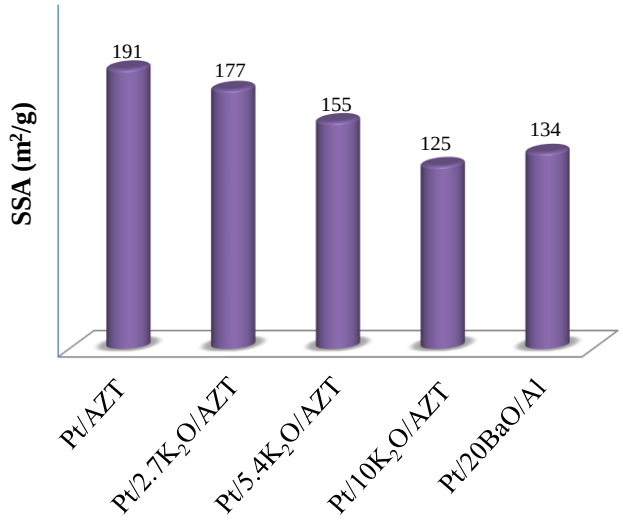

Figure 14: BET specific surface area values for the K_2O-supported materials in comparison to benchmark Pt/20BaO/Al_2O_3 after calcination at 973 K for 150 min.

3.1.4 Pore Size Analysis *via* N_2 Sorption

The N_2 sorption isotherms of the binary and ternary mixed oxides were also analyzed. The N_2 sorption isotherms displayed type IV isotherms for both binary and ternary support oxides, which are characteristic for mesoporous structures (Figure 15a and 15b). Moreover, the BJH pore size distribution analysis of these corresponding materials exhibited a narrow distribution centered at 11 nm and 4 nm for the binary and ternary oxide system; respectively (Figure 15c and 15d). These results are also in perfect agreement with the previous XRD data and SSA values, where the presence of Al_2O_3 domains were shown to result in more disordered structures and an increase in SSA. Larger pore size for the binary oxide is consistent with the corresponding XRD results (Figure 6b), where sharp and well defined diffraction lines were observed, indicating larger particles and an ordered structure.

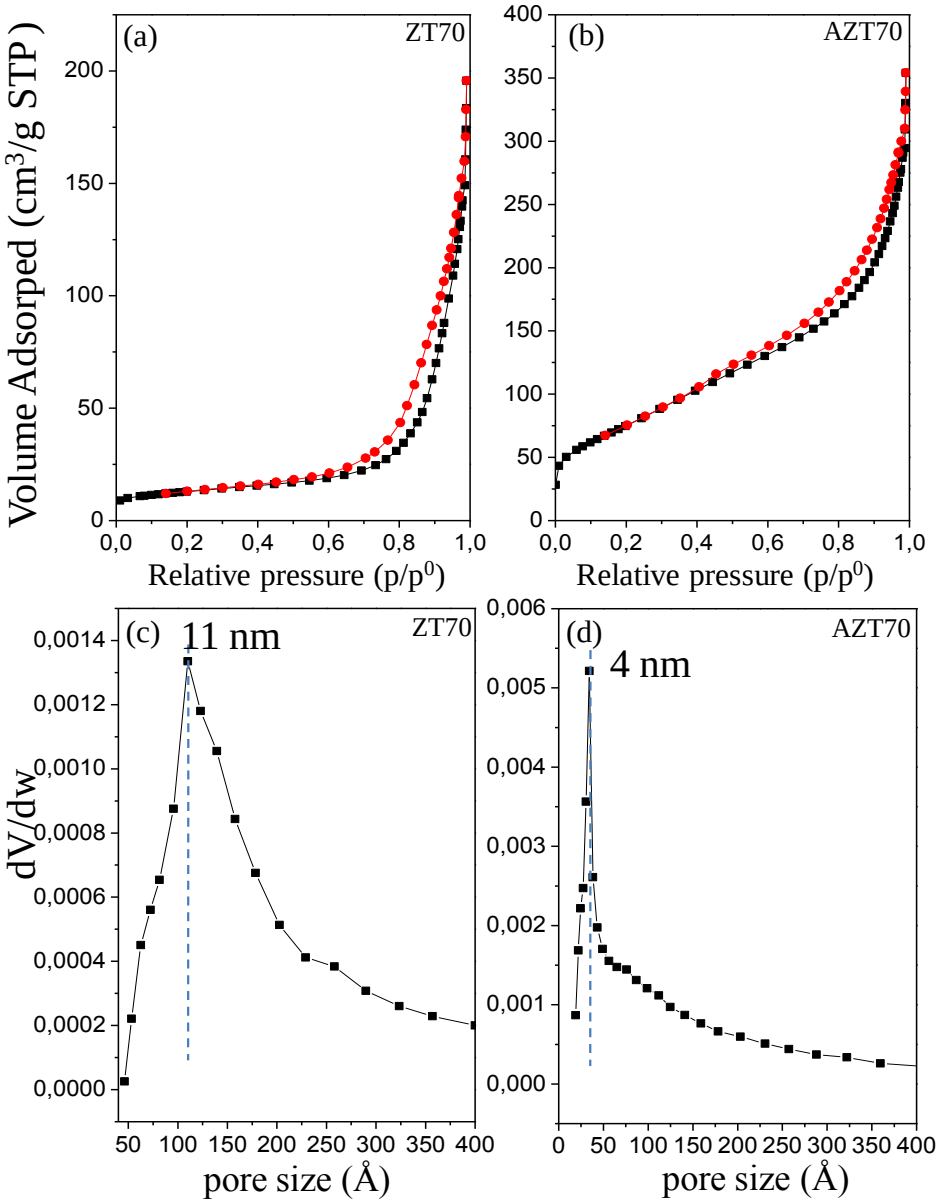

Figure 15: N_2 adsorption(black)/desorption(red) isortherms of (a) mesoporous binary and (b) mesoporous-ternary oxides and pore size distribution of corresponding metarials of (c) mesoporous binary and (d) mesoporous-ternary oxides. Both materials were calcined at 973 K for 150 min.

3.2 *in-situ* FTIR Analysis

3.2.1 NO_x Adsorption Properties

3.2.1.1 NO_x Adsorption on Binary and Ternary Support Oxides

Figure 16 represents the FTIR spectra corresponding to NO_2(g) adsorption on both of the binary and ternary oxide materials (already calcined at 973 K) at 323 K for increasing exposures. Five particular vibrational features were detected in the ZT which were located at 1644, 1578, 1550, 1280 and 1209 cm^{-1} as illustrated in Figure 16a. The spectral region between 1700 and 1200 cm^{-1} is characteristic for the nitrate and nitrite species coordinated to TiO_2 and ZrO_2[95]–[97].

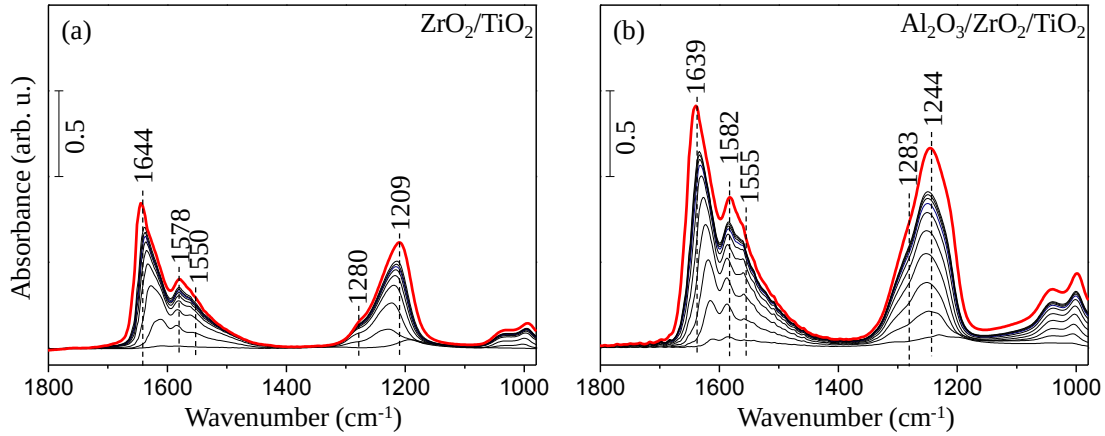

Figure 16: FTIR spectra corresponding to the stepwise NO_2(g) adsorption at 323 K on (a) ZT and (b) AZT surfaces. The bold (red) spectrum in each panel corresponds to the NO_x-saturated (5.0 Torr NO_2(g) for 10 min. at 323 K) surface. Copyright 2014 Elsevier B.V. [67].

The observed frequencies at 1644 and 1209 cm^{-1} can be attributed to bridging nitrates, while the features at 1578, 1550 and 1280 cm^{-1} can be assigned to bidentate nitrates [23], [98]. Similar absorption features also appeared for the AZTternary oxide system as shown in Figure 16b. However, the position of bridging nitrates (1639 and 1244 cm^{-1}) on the AZT ternary oxide is different when compared to the

ZT binary oxide system. Probably, the most prominent aspect of Figure 16 is the dissimilarity in the relative FTIR intensities of AZT and ZT systems. It is clear that the NO_x adsorption on the AZT ternary oxide is significantly higher than that of the ZT binary oxide due to a ten-fold higher specific surface area and the significantly greater IR absorption intensity upon NO_x adsorption of the former surface at 973 K.

3.2.1.2 NO_x Adsorption on Pt-Supported Binary and Ternary Oxides

The effect of Pt incorporation on NO_x adsorption geometry and storage capacity was also investigated *via* in-situ FTIR spectroscopy as shown in Figure 17. FTIR studies involving NO_x adsorption experiments on $Pt/ZrO_2/TiO_2$ and $Pt/Al_2O_3/ZrO_2/TiO_2$ lead us to conclude that the presence of Pt has no significant influence on the NO_x adsorption geometries.

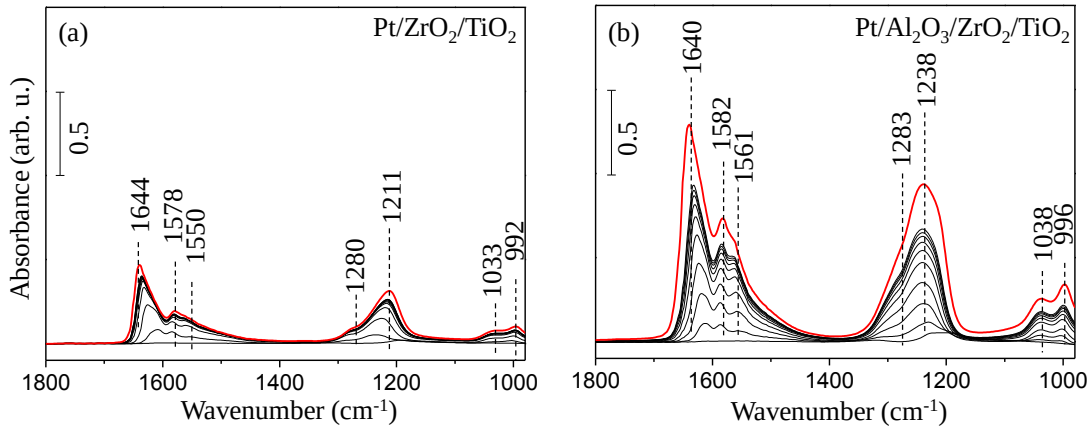

Figure 17: FTIR spectra corresponding to the stepwise NO_2(g) adsorption at 323 K on (a) Pt/ZT and (b) Pt/AZT surfaces. The bold (red) spectrum in each panel corresponds to the NO_x-saturated (5.0 Torr NO_2(g) for 10 min. at 323 K) surface.

3.2.1.3 NO_x Adsorption on Pt-Supported NSR/LNT Catalyst with Basic Storage Domains

Figure 18 illustrates the in-situ FTIR spectra corresponding to NO_2(g) adsorption on (a) Pt/AZT, (b) Pt/8BaOAZT, (c) Pt/20BaO/AZT and (d) Pt/20BaO/Al_2O_3 from low pressures up to saturation (5.0 Torr NO_2 for 10 min) level at 323 K. Each material exhibits highly convoluted features in the spectral range of 1800-1000 cm^{-1} including well-known oxide coordinated nitrite and nitrate functional groups reported in literature as well as in our former studies [22], [23], [26], [67], [96], [97], [99], [100].

In Figure 17a, there are five main vibrational stretchings located at 1640, 1582, 1561, 1283 and 1238 cm^{-1} on BaO-free Pt/AZT material. While features at 1640 and 1238 cm^{-1} can be attributed to bridging type of nitrates, other three frequencies at 1582/1283 and 1561 cm^{-1} are known as bidentate and monodentate nitrates; respectively [25], [67]. It is worth mentioning that highly convoluted spectral line characteristics renders proper assignment of nitrate/nitrite features rather difficult. On the other hand, incorporation of BaO domains leads to a different spectral line shape upon NO_x adsorption as demonstrated in Figures 18b and 18c for Pt/8BaO/AZT and Pt/20BaO/AZT; respectively. As illustrated in Figures 18b-18d, NO_x interaction of each material generates six main vibrations located at *ca.* 1628, 1570, 1480, 1436, 1324 and 1234 cm^{-1}. In addition to the surface nitrate/nitrite groups, formation of bulk/ionic type of nitrate groups which are apparent by the features located at 1480, 1437 and 1322 $cm^{-1}$are observed as well.

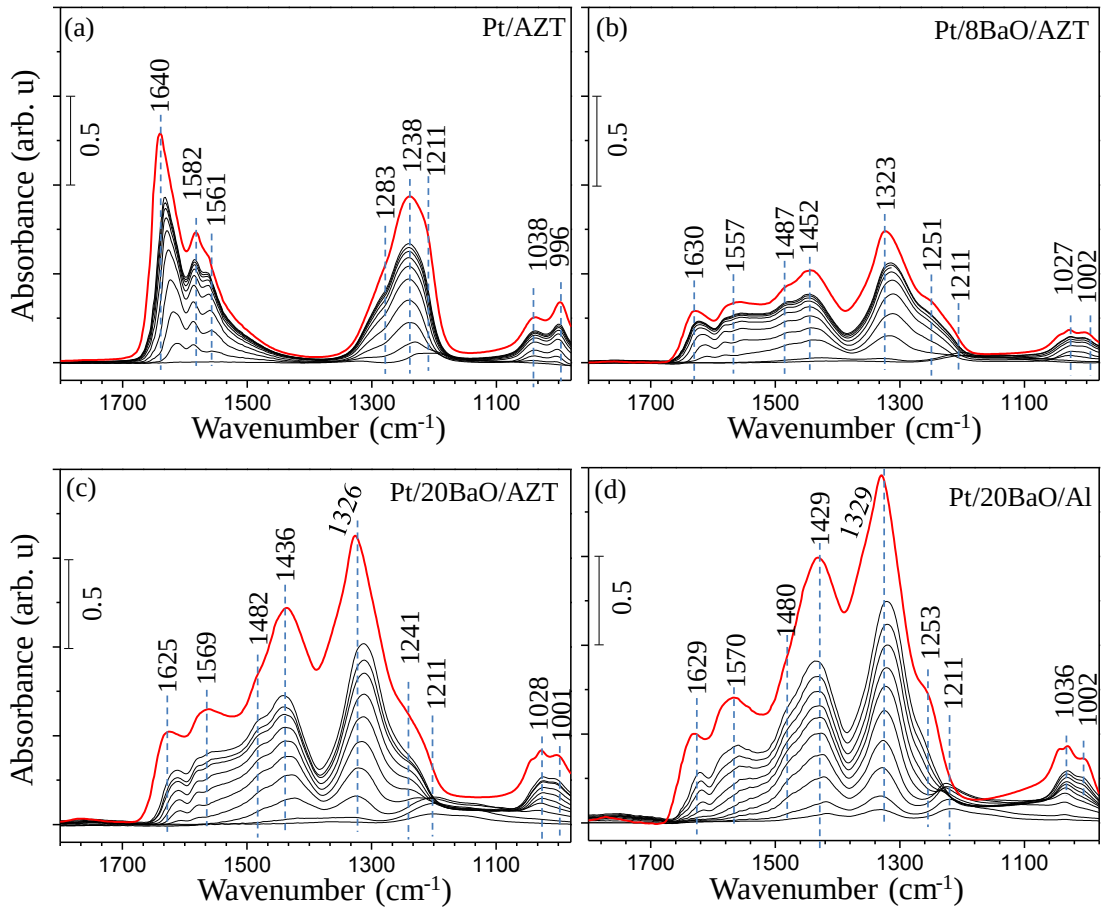

Figure 18: FTIR spectra corresponding to the stepwise NO_2(g) adsorption at 323 K on (a) Pt/AZT, (b) Pt/8BaO/AZT, (c) Pt/20BaO/AZTand Pt/20BaO/Al_2O_3surfaces. The bold (red) spectrum in each panel corresponds to the NO_x-saturated (5.0 Torr NO_2(g) for 10 min. at 323 K) surface.

Irrespective of the presence of BaO domains, a detailed and stepwise analysis of the in-situ spectroscopic data yields the possible adsorption routes regarding how NO_2 molecules are initially adsorbed as nitrites (i.e. features located at 1211 cm^{-1}) and are subsequently oxidized to nitrate functional groups.

On the other hand, absorbance intensity of the spectrum corresponding to NO_x-saturated Pt/20BaO/AZT (top-most red spectra in Figure 18c) is clearly higher than that of Pt/8BaO/AZT (Figure 18b). These findings imply a higher amount of NO_x adsorption on Pt/20BaO/AZT as compared to Pt/AZT and Pt/8BaO/AZT at 323 K.

However, it is not quite accurate to gather quantitative information from solely FTIR absorption intensities. More accurate quantitative comparison of NSC was also performed *via* flow-mode reactor studies that will be described in the upcoming sections.

Although Pt/8BaO/AZT and Pt/20BaO/AZT samples revealed efficient NO_x storage at 573 K, their storage ability at 673 K is not that effective as compared to that of Pt/20BaO/Al_2O_3 benchmark catalyst. Therefore, AZT-supported NSR/LNT materials need to be improved further in terms of their high-temperature NO_x storage capacities [95], [101], [102]. Along these lines, identical set of NO_x adsorption experiments were also conducted for K_2O-incorporated materials.

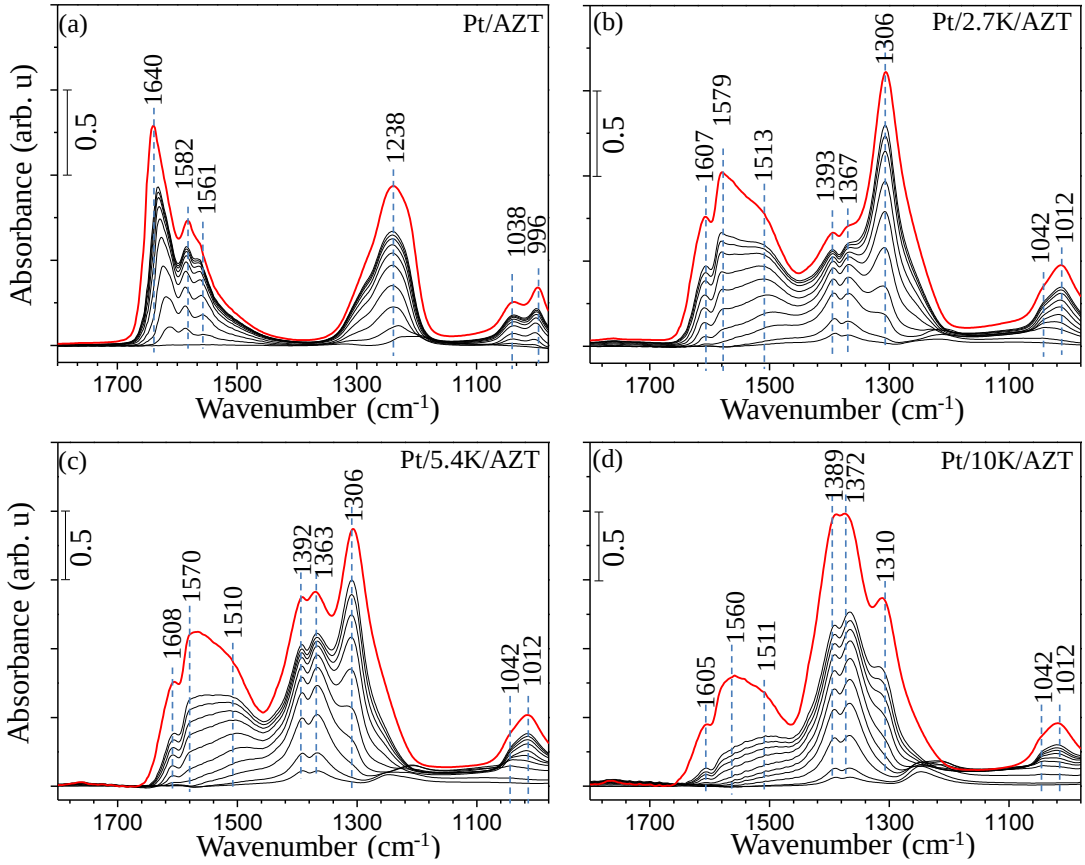

Figure 19: FTIR spectra corresponding to the stepwise NO_2(g) adsorption at 323 K on (a) Pt/AZT, (b) Pt/2.7K_2O/AZT, (c) Pt/5.4K_2O/AZT and (d) Pt/10K_2O/AZTsurfaces. The bold (red) spectrum in each panel corresponds to the NO_x-saturated (5.0 Torr NO_2(g) for 10 min. at 323 K) surface.

Figure 19 illustrates the in-situ FTIR spectra corresponding to incremental NO_2(g) adsorption on (a) Pt/AZT, (b) Pt/2.7K_2O/AZT, (c) Pt/5.4K_2O/AZT and (d) Pt/10K_2O/AZT from low pressures up to saturation (5.0 Torr NO_2 for 10 min) at 323 K. These materials contained 2.7 and 5.4 wt. % K_2O where molar amount of K_2O was comparable to that of 8 and 20 wt. % BaO in Pt/8BaO/AZT and Pt/20BaO/AZT used in the previous studies [103].

As illustrated in Figure 19a, the NO_x adsorption profile of Pt/AZT material is shown here once again in order to have a clear comparison with its K_2O-containing counterparts. NO_x exposure on K_2O-based materials revealed eight major vibrational features located at *ca.* 1608, 1570, 1511, 1392, 1369, 1306, 1042 and 1020 cm^{-1}. Among these stretchings, 1608 and 1570 cm^{-1} can be assigned to surface bridging and bidentate type of nitrates; respectively. Another set of features at 1510 and 1306 cm^{-1} can be assigned for monodentate type of surface nitrates on potassium oxide. In addition to these, features at 1392 and 1369 cm^{-1} correspond to ionic/bulk like potassium nitrates [33], [101], [104].

It is observed that increase in K_2O loading leads to an increase in the formation of ionic/bulk like nitrate (*i.e.* 1392/1369cm^{-1}) features together with the suppression of surface nitrates. These results are in good agreement with the literature data regarding the effect of K_2O loading on the nature of the adsorbed nitrate species on Pt/K_2O/TiO_2 and Pt/K_2O/Al_2O_3 [29], [105]–[107]. Thus, it is apparent that, AZT support sites and K_2O domains can simultaneously take significant part in the NO_x adsorption processes on Pt/2.7K_2O/AZT. However, NO_x species preferentially accumulates on K_2O domains, particularly for materials with higher K_2O loadings (*i.e.* Pt/5.4K_2O/AZT and Pt/10K_2O/AZT). Increase in the K_2O

loading also results in the growth of the K_2O particle size and formation of 3D agglomerates, enabling the adsorption of NO_x in the form of bulk-like nitrates. Moreover, as in the case of BaO-based materials, K_2O-based materials also contain similar type of nitrate species such as ionic/bulk and surface nitrates. Hence, their adsorption mechanisms are likely to be similar [15], [108], [109]. Therefore, based on the previous literature data, increase in NSC at higher K_2O loadings can be associated to the extent of bulk-like potassium nitrate formation.

3.2.2 NO_x Reduction *via* H_2(g)

After the analysis of NO_x adsorption characteristics of the investigated materials were completed, their NO_x reduction/regeneration/removal performances under reducing/rich conditions were also studied. Thermal stabilities of nitrate/nitrite species in the presence of an external reducing agent as well as their reduction mechanisms were investigated by means of FTIR spectroscopy.

3.2.2.1 NO_x Reduction *via* H_2(g) on Binary and Ternary Support Oxides

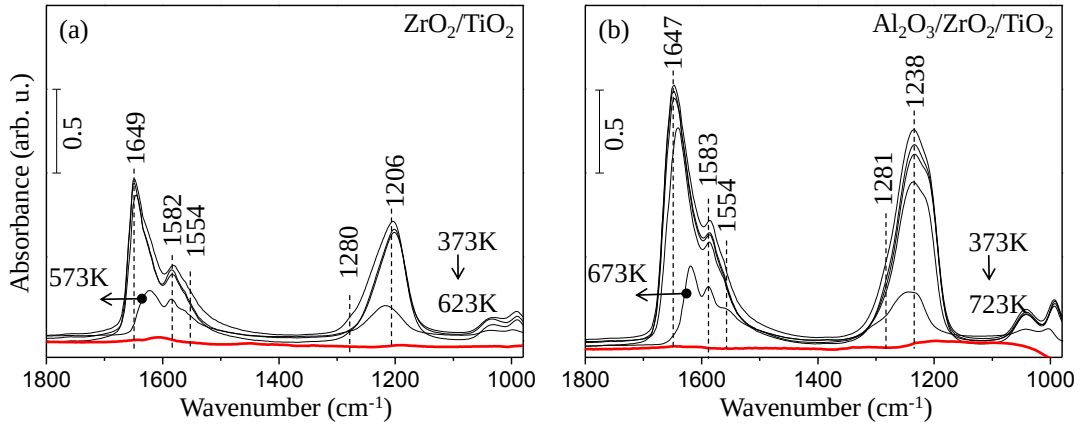

Figure 20: FTIR spectra corresponding to the temperature-dependent nitrate reduction *via* 15.0 Torr of H_2(g) on (a) ZT and (b) AZT surfaces. The topmost spectrum in each panel corresponds to the NO_x-saturated (5.0 Torr NO_2(g) for 10 min. at 323 K) surface. The series of black spectra in each panel were collected at different temperatures within 323-723 K. The bottommost (red) spectrum in each panel corresponds to the highest reduction temperature exploited (i.e. 623 K for ZT and 723 K for AZT). Copyright 2014 Elsevier B.V.[67].

Figure 20a and 20b illustrates the temperature-dependent nitrate reduction of Pt-free binary and ternary mixed oxides; respectively. Prior to nitrate reduction, the material surfaces were saturated with 5.0 Torr NO_2(g) for 10 min at 323 K. These

saturated material surfaces were then treated with 15.0 Torr of H_2(g) exposure at 323 K. A series of FTIR spectra were recorded as a function of temperature after annealing the NO_x-saturated surfaces at 373, 473, 573, 623, 673, 723 K in the presence of H_2(g). Adsorbed nitrate/nitrite functional groups on ZT (Figure 19a) were found to be highly stable in the presence of external H_2 up to 473 K with only minor IR intensity changes. However, nitrate/nitrite features significantly eliminated from the ZT material surface at 573 K which can be followed by the decrease in IR absorbance intensities (Figure 20a). It is also worth mentioning that bidentate nitrates (1580 cm^{-1}) had relatively higher thermal stability compared to bridging nitrates (1649 cm^{-1}) under reducing conditions on the binary ZrO_2/TiO_2 oxide system. Finally, the bottommost red spectrum in Figure 19a corresponds to complete removal of all of the N-related functional groups from the ZT surface under H_2(g) environment at 623 K.

Identical set of experiments were also conducted on the AZT ternary oxide system (Figure 20b). These results clearly indicate that nitrate/nitrite species have much higher thermal stabilities on the AZT surface than that of ZT binary oxide. While nitrate/nitrite groups on ZT binary oxide are mostly reduced at 573 K, they could not be eliminated at this particular temperature on AZT. FTIR analysis clearly indicated that under reducing conditions, nitrate regeneration performance of binary mixed oxide is much greater than that of the ternary mixed oxide where all of the nitrate/nitrite species on AZT can be completely reduced only at 723 K.

3.2.2.2 NO_x Reduction *via* H_2(g) on Pt-Functionalized Binary and Ternary Oxides

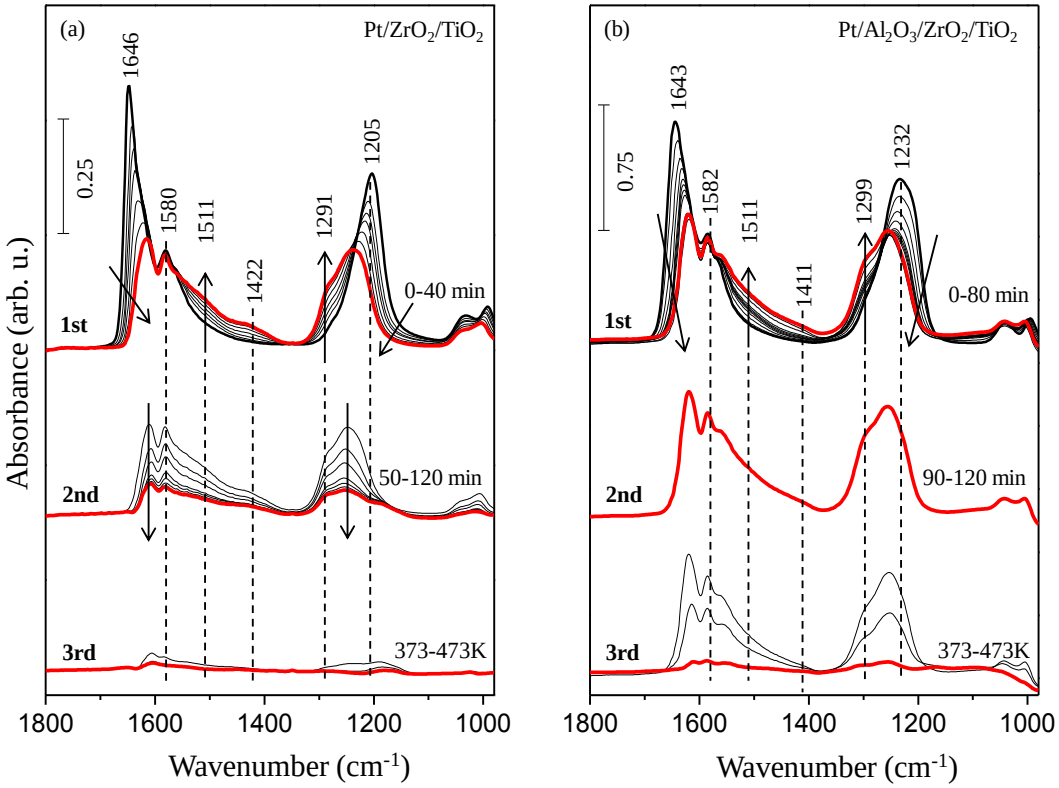

Figure 21: FTIR spectra corresponding to the temperature-dependent nitrate reduction *via* 15.0 Torr of H_2(g) on (a) AZT and (b) AZT surfaces. The topmost spectrum in each panel corresponds to the NO_x-saturated (5.0 Torr NO_2(g) for 10 min. at 323 K) surface. The series of black spectra in each panel were collected at different temperatures within 323-723 K. The bottommost (red) spectrum in each panel corresponds to the highest reduction temperature exploited (i.e. 623 K for ZT and 723 K for AZT). Copyright 2014 Elsevier B.V.[67].

In this section, nitrate reduction characteristics of Pt-functionalized ZT and AZT materials under reducing environment as a function of time and temperature is examined by means of *in-situ* FTIR technique. Since nitrate/nitrite reduction on Pt-containing materials at elevated-temperatures lead to fast reactions, it is rather difficult to follow the initial stages of the reduction process. Therefore, nitrate/nitrite reduction experiments were carried out at 323 K in order to monitor and elucidate the temporal changes in the surface functional groups on material surfaces upon reduction by H_2(g).

Series of FTIR spectra regarding the nitrate/nitrite reduction from Pt/ZT and Pt/AZT surfaces were recorded as a function of time in the presence of external reducing agent (i.e H_2). Prior to reduction process, materials were saturated with 5.0 Torr NO_x for 10 min. These NO_x-saturated materials were followed by the introduction 15.0 Torr of H_2(g) at 323 K.

Each panel in Figure 21 is divided into three different sections. Initial reduction period presented in the top section in Figure 21a illustrates the set of spectra collected in first 40 min at 323 K for Pt-functionalized binary oxide, Pt/ZT. In this first period, decrease in absorbance intensities for particular frequencies (1646 and 1205 cm^{-1}) corresponding to bridging nitrates can be simultaneously followed together with the increase in other vibrational features at 1511 and 1291 cm^{-1} corresponding to monodentate nitrate species [23], [24], [99]. Other particular vibrational features regarding the growth of nitrite species appeared at 1422 and 1291 cm^{-1} [25].

Throughout the second time interval (50-120 min.), which is presented in the middle section of Figure 21a, most (though not all) of the N-related functional

groups (*i.e.* nitrates/nitrites) were eliminated from the material surface upon H_2(g) exposure. No additional features were observed during this period of time and NO_x reduction mostly ceased after 120 min. In the third stage presented at the bottom of Figure 21a, catalyst was annealed to higher temperatures (373, 423 and 473 K) in H_2(g) environment, in order to achieve complete regeneration of the Pt/ZT surface.

These series of spectra can allow us to have a better insight regarding the initial and final stages of the nitrate/nitrite reduction mechanism on the Pt/ZT surface in the presence of an external reducing agent such as H_2(g). In this particular case, bridging type of nitrates were initially transformed into monodentate type of nitrates and nitrites, which were followed by complete regeneration at 373 K.

On the other hand, similar set of experiments were also performed for the Pt/AZT surface (Figure 21b). Introduction of reducing agent (*i.e.* H_2) over the NO_x-saturated surface caused the attenuation of the absorbance intensities of bridging nitrates (1643 and 1232 cm^{-1}) in the very early stages. This change in bridging functional groups can also be followed by formation of monodentate type of nitrates (1511 and 1299 cm^{-1}) as well as the monodentate nitrites (1411 cm^{-1}). The presence of isosbestic points in Figure 21 strongly implies a direct transformation from bridging nitrates to monodentate nitrates. A noteworthy difference between the Pt-incorporated binary and ternary systems is that N-related surface functional groups behave in a different manner in the second time interval. While nitrate/nitrite groups were continuously removed throughout the second time interval for Pt/ZT, no spectral change was observed in the second time interval of Pt/AZT. Moreover, these series of FTIR spectra revealed that absorbance intensities of N-related features on Pt/AZT was found to be much higher than that of Pt/ZT at the end of second time interval. In accordance with the previously discussed in-situ FTIR results (Figure

20), results presented in Figure 21 also clearly indicated that nitrate/nitrite groups had much higher thermal stability on ternary oxide supported systems as compared to binary oxide systems.

This finding is consistent with the temperature-dependent *in-situ* FTIR data set recorded in H_2(g) environment at different temperatures in the third interval of Figure 21b. At 373 K, while complete nitrate/nitrite regeneration was almost achieved on Pt/ZT material; there was a significant amount of N-related residues on Pt/AZT which could be eliminated at 473 K. Furthermore, it can also be concluded that Pt/AZT material had a much more efficient NO_x removal characteristics as compared to the benchmark Pt/20BaO/Al catalyst [67], and its CeO_2-modified counterpart (Pt/20BaO/20CeO_2/Al) [23].

Entire discussion regarding the reduction mechanism of nitrate/nitrite functional groups can be illustrated in scheme 7 as follows:

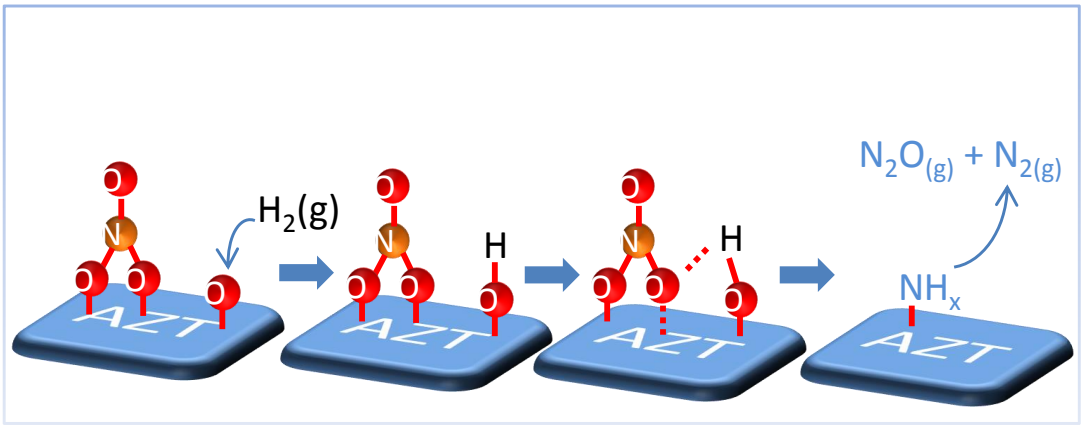

Scheme 7: Schematic illustration of nitrate reduction mechanism.

3.2.2.3 NO_x Reduction *via* H_2(g) on Pt and Basic Oxide-Functionalized AZT Catalysts

Pt-functionalized materials were further modified by the incorporation of basic storage components such as BaO or K_2O. Figure 22a-d present the time-dependent changes in the nitrate/nitrate functional groups on BaO-based materials during their interaction with excess hydrogen at 323 K for 120 min as well as thermal regeneration at various temperatures (i.e. 373, 473 and 573 K). Prior to nitrate/nitrite reduction, material surfaces were saturated by 5.0 Torr NO_x for 10 min at 323 K. Black spectra in Figure 22a-22d were recorded after NO_x saturation over fresh Pt/AZT, Pt/8BaO/AZT, Pt/20BaO/AZT and Pt/20BaO/Al; respectively. The surfaces of NO_2-saturated materials were subsequently exposed to 15 Torr of H_2(g) and series of spectra were recorded as a function of time and temperature. Each panel in Figure 22 shows two different sets of spectra. While the upper set of spectra (red, gray and black spectra) were collected as a function of time over the course of 2 h, bottom data set (blue spectra) reveal the thermal stabilities of nitrate/nitrite groups as a function of temperature (i.e. at 473 and 573 K).

In Figure 22a, during the first period, introduction of 15.0 Torr H_2(g) over NO_x saturated Pt/AZT surface causes sudden changes in vibrational frequencies. While the vibrational stretchings at 1643 and 1232 cm^{-1} (bridging nitrates) attenuate, an increase in the intensities of 1511 and 1299 cm^{-1} (monodentate nitrates) as well as 1411 cm^{-1} (nitrites) can be observed. The weak feature at 1411 cm^{-1} can be also taken in to account as bulk nitrate in the light of former studies [23], [67], [110].

Changes in the intensities of nitrate features remain invariant after 2 hours of H_2(g) exposure of Pt/AZT (gray spectrum Figure 22a). From a mechanistic point of

view, these results give us some insight regarding the reduction mechanism where bridging nitrates are transformed into monodentate nitrates and nitrite groups on Pt/AZT material. It is clear that bidentate nitrates (1582 cm^{-1}) exhibit a stable character during the reduction process where their absorbance intensities remain roughly constant for 2 h. Then, the Pt/AZT sample was gradually heated in H_2(g) to 373 and 473 K in order to accelerate the nitrate reduction process (Figure 22a).

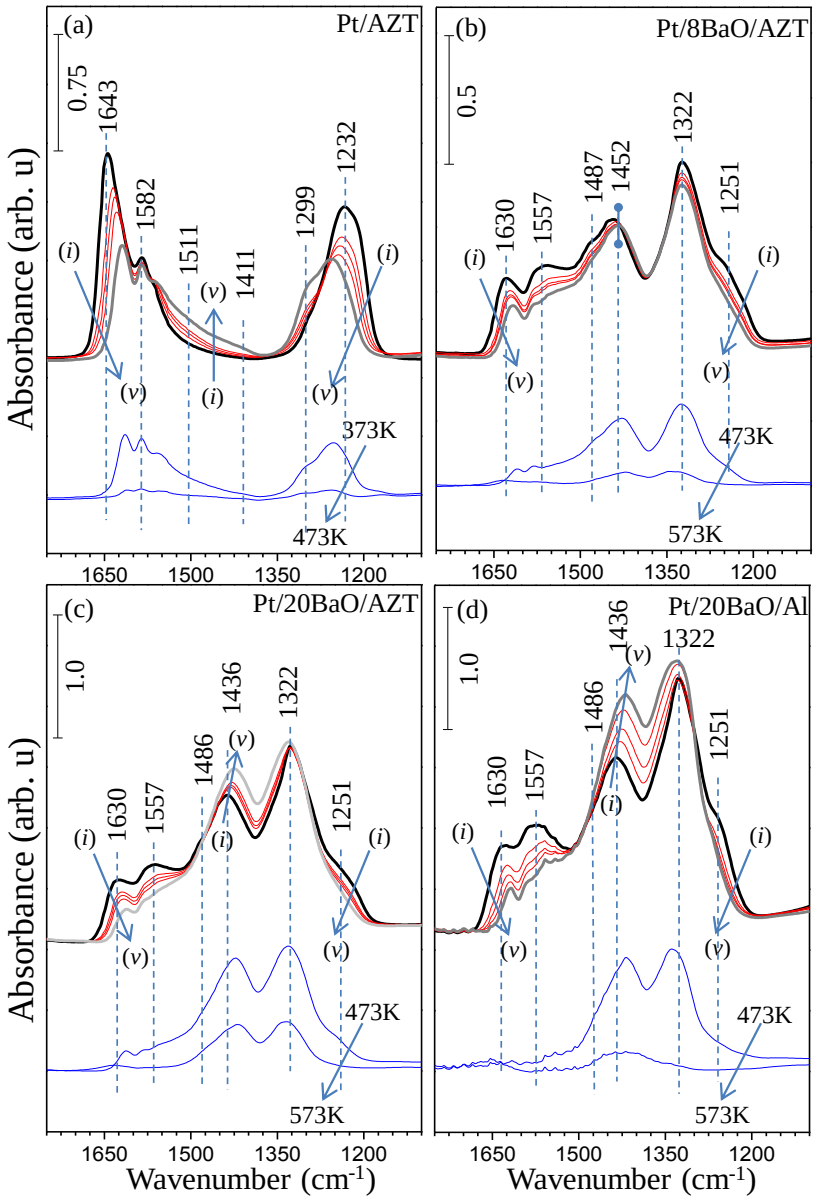

Figure 22: FTIR spectra corresponding to the time-dependent nitrate reduction *via* 15.0 Torr of H_2(g) on Pt/AZT, (b) Pt/8BaO/AZT (c) Pt/20BaO/AZT and (d) Pt/20BaO/Al surfaces. The topmost spectrum (*i*) in each panel corresponds to the NO_x-saturated (5.0 Torr NO_2(g) for 10 min. at 323 K) surface. The series of spectra *(ii), (iii), (iv) and (v)* were collected as a function of time at 3th, 10th, 30th and 120th min of reduction at 323 K; respectively. The bottom set of FTIR spectra in each panel were collected after the initial 120 min reduction at 323 K by increasing to temperature to 373, 423 and 473 K in the presence of H_2(g).

FTIR spectra recorded at those two temperatures are illustrated in the bottom set of (blue) spectra given in Figure 22a, indicating that the complete nitrate removal was achieved at 473 K.

An identical experimental procedure was also applied to Pt/8BaO/AZT catalyst as illustrated in Figure 22b. Throughout the initial period of 120 min, surface nitrate functional groups (1630, 1557 and 1251 cm^{-1}) of the Pt/8BaO/AZT material were gradually eliminated upon H_2(g) exposure. Meanwhile, absorbance intensities of bulk/ionic type of nitrates (1487, 1452 and 1322 cm^{-1}) did not change significantly and stayed intact during the hydrogen regeneration.

Nitrate groups on Pt/20BaO/AZT and Pt/20BaO/Al_2O_3, however revealed relatively different characteristics towards H_2(g) interaction, especially for bulk/ionic like nitrates as shown in Figure 22c and Figure 22d; respectively. It is apparent that FTIR spectra obtained after H_2(g) exposure demonstrated an immediate increase in the absorbance intensity of bulk-like nitrates (*ca.* 1436 cm^{-1}) together with the elimination of surface nitrates (*ca.* 1630, 1557 and 1251 cm^{-1}) as a function of time from Pt/20BaO/AZT and Pt/20BaO/Al_2O_3 materials.

Surface and bulk-like nitrates on Pt/8BaO/AZT, Pt/20BaO/AZT and Pt/20BaO/Al_2O_3 materials became invariant at the end of 2 hours reduction process at 323 K. Blue spectra given at the bottom of Figure 22b-d are recorded at 473 and 573 K in hydrogen atmosphere. These results revealed that while nitrates were completely reduced at 573 K on Pt/AZT and Pt/8BaO/AZT, there were still detectable amounts of NO_x remaining on Pt/20BaO/AZT and Pt/20BaO/Al.

Formation of bulk/ionic nitrates in the presence of H_2(g) atmosphere can be indirectly linked to –OH functional groups present on the catalyst surfaces. Figure 23 demonstrates the changes in the –OH spectral region (3800-3000 cm^{-1}) of the materials represented in Figure 22 during 120 min reduction at 323 K. These findings are in excellent agreement with the literature. For instance, Olsson *et al.* [111] illustrated that Pt particles can be oxidized to PtO_x upon NO_x exposure on Pt/Al_2O_3 or $Pt/BaO/Al_2O_3$ catalysts. Then PtO_x species can interact with the surface –OH groups (3540 cm^{-1}) generated *via* H_2 exposure as illustrated in the –OH spectral region (Figure 23). The interaction between PtO_x and –OH groups leads to the H_2O generation on surface which facilitates the formation of bulk/ionic nitrates during the early stages of nitrate reduction mechanism [25].

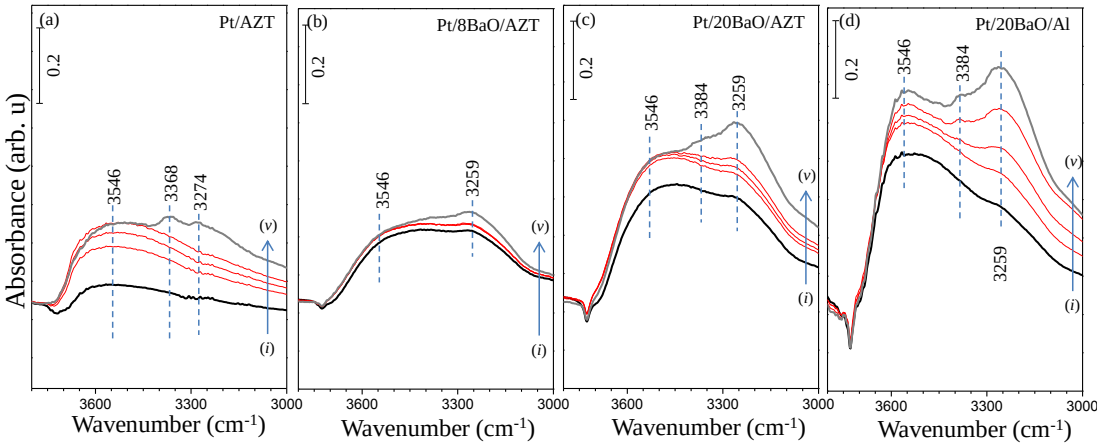

Figure 23: –OH/–NH stretching region of the in-situ FTIR spectra corresponding to NO_2 saturation *(i)* (5.0 Torr NO_2(g) for 10 min. at 323 K) followed by subsequent reduction with 15.0 Torr of H_2(g) on (a) Pt/AZT, (b) Pt/8BaO/AZT, (c) Pt/20BaO/AZT and (d) $Pt/20BaO/Al_2O_3$ at 323 K. The series of spectra *(ii), (iii), (iv) and (v)* were collected as a function of time at 3th, 10th, 30th and 120th min of reduction at 323 K; respectively.

As illustrated in Figure 23b, the absorbance intensity of vibrational feature at 3540 cm^{-1} does not change significantly for Pt/8BaO/AZT as compared to other Ba-containing samples namely, Pt/20BaO/AZT (Figure 23c) and Pt/20BaO/Al_2O_3 (Figure 23d). Therefore, this may imply that the formation of bulk nitrates upon H_2 exposure is facilitated at higher BaO surface coverages (*i.e.* wt. % BaO loading). Moreover, Kim *et al.* [100] performed solid state magic angle spinning (MAS) NMR spectroscopic experiments supporting the significant role of water on the formation of bulk $Ba(NO_3)_2$ species.

Further insight regarding this nitrate reduction process *via* H_2(g) can be obtained by investigating the features located at 3384 and 3252 cm^{-1}. These poorly resolved and convoluted features can be correlated to the presence of N-H stretching modes associated with $–NH_2$, $–NH_3$, $–OH\cdots NH_x$ or $–OH\cdots NO_x$ species [23], [67], [89].

Finally, in the case of BaO-containing materials, it can be argued that reduction *via* H_2 may lead to the following routes:

$$Ba(NO_3)_2 + 5H_2 \Leftrightarrow Ba(OH)_2 + N_2 + 4H_2O \qquad 3.2$$

$$Ba(NO_3)_2 + 5H_2 \Leftrightarrow BaO + N_2 + 5H_2O \qquad 3.3$$

Among these possible reactions, the first pathway involving the formation of $Ba(OH)_2$ is consistent with the formation of surface hydroxyl groups on Pt/20BaO/AZT and Pt/20BaO/Al materials as illustrated in Figure 23c and Figure 23d. The second reduction pathway is also a likely pathway, particularly for the Pt/8BaO/AZT catalyst which lacked a significant amount of surface -OH functionalities. These arguments are also consistent with literature reporting the

immediate formation of N_2 and H_2O upon switching from lean to rich cycle at 573 K in the absence of CO_2 and H_2O in the feed stream [112]. On the other hand, other possible nitrate reduction products such as N_2O and NH_3 should not be disregarded which are consistent with the formation of surface -NH_x species observed in Figure 23a-d. Depending on these findings, an alternative reduction pathway can also be considered:

$$Ba(NO_3)_2 + 13/2\ H_2 \Leftrightarrow Ba(OH)_2 + 1/2\ N_2 + NH_3 + 4H_2O \qquad 3.4$$

Similar nitrate/nitrite reduction experiments were also carried out for K_2O-based materials under identical experimental conditions. After the saturation of the surfaces with NO_x was complete, materials were exposed to 15.0 torr H_2(g) and series of spectra were collected as a function of time at 323 K followed by the regeneration at various temperatures (*i.e.* 473 and 573 K). Figure 24a-d demonstrate the corresponding changes in the surface functional groups on Pt/AZT, Pt/2.7K_2O/AZT, Pt/5.4K_2O/AZT and Pt/10K_2O/AZT; respectively. In Figure 24, each panel is divided into two different sets of spectra for clarity. While the upper set of data (red spectra and gray spectrum) were collected as a function of reduction time during the first 120 min of hydrogen exposure at 323 K, bottom data set (blue spectra) correspond to the gradual reduction of the nitrate/nitrite groups in the presence of hydrogen at elevated temperatures (i.e. 473 and 573 K). The initial stages of nitrate reduction process at 323 K for Pt/2.7K_2O/AZT and Pt/5.4K_2O/AZT takes place *via* simultaneous decrease in the absolute IR intensities of bridging (1608 cm^{-1}), bidentate (1579 cm^{-1}) and monodentate (1507 cm^{-1}) type of nitrates. However, when the relative changes of the IR signals corresponding to different types of nitrates are analyzed, it can be seen that the relative signal intensity of monodentate

nitrates (1507 cm^{-1}) decreased less than that of bridging and bidentate nitrates at the end of 120^{th} minute of reduction process. These findings can lead us to deduce such a basic knowledge regarding the nitrate reduction mechanism on these particular materials. Here, one can readily state that nitrate reduction pathway initially takes place through the transformation of bridging and bidentate type of nitrates into monodentate nitrates. In other words, monodentate type of nitrates (and their protonated forms, i.e. HNO_3 coordinated to the surface) might have relatively higher stability as compared to other surface species acting as an intermediate in the nitrate reduction process. Upon interaction with H_2(g), it is clear that absorbance intensities of vibrational frequencies located at 1392/1369cm^{-1} visibly increased for higher K_2O loadings (*i.e.* Pt/5.4K_2O/AZT and Pt/10K_2O/AZT), revealing the formation bulk-like nitrates during the reduction process. However, the formation of bulk-like nitrate species is less significant for lower K_2O loading of Pt/2.7K_2O/AZT as shown in Figure 24b; indicating a smaller K_2O particle size and higher dispersion at lower basic oxide surface coverages.

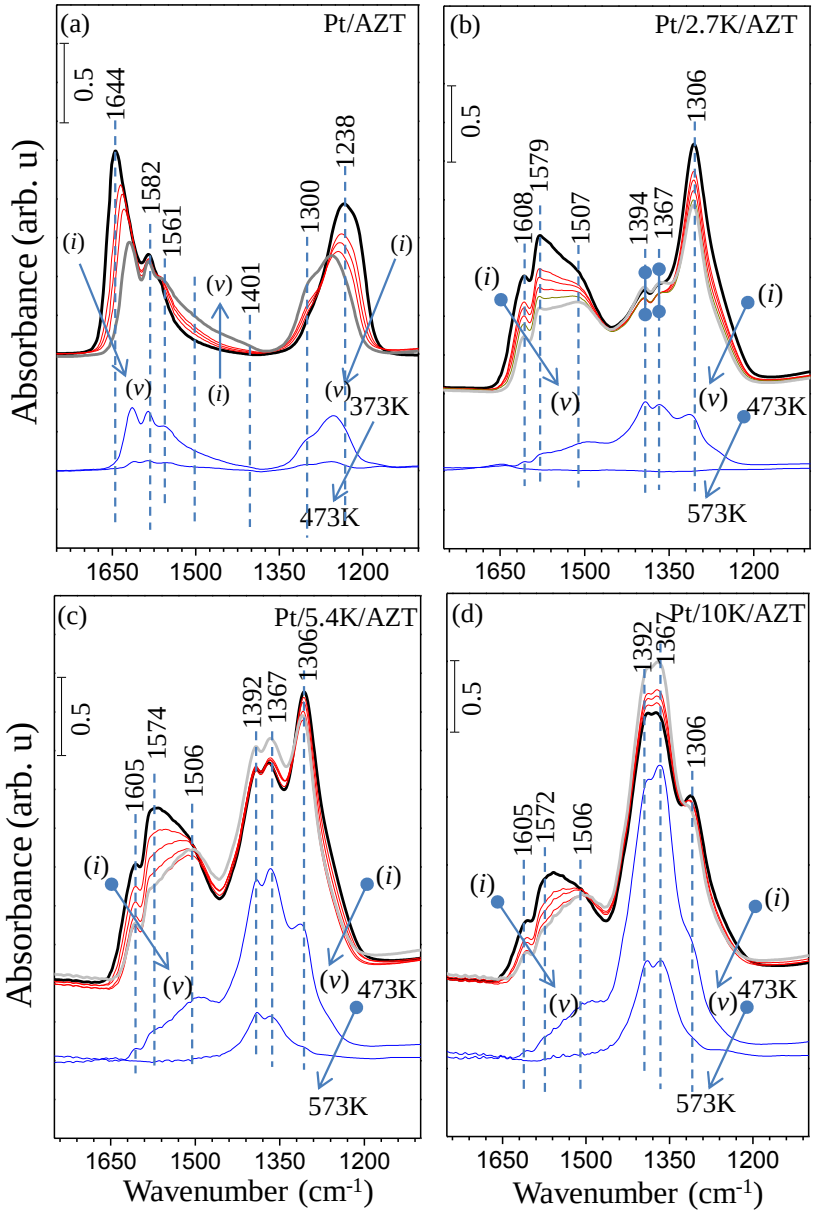

Figure 24: FTIR spectra corresponding to the time-dependent nitrate reduction *via* 15.0 Torr of H_2(g) on (a) Pt/AZT, (b) Pt/2.7K_2O/AZT (c) Pt/5.4K_2O/AZT and (d) Pt/10K_2O/AZT surfaces. The topmost spectrum (*i*) in each panel corresponds to the NO_x-saturated (5.0 Torr NO_2(g) for 10 min. at 323 K) surface. The series of spectra *(ii), (iii), (iv) and (v)* were collected as a function of time at 3th, 10th, 30th and 120th min of reduction at 323 K; respectively. The bottom set of FTIR spectra in each panel were collected after the initial 120 min reduction at 323 K followed by increasing to temperature to 473 and 573 K in the presence of H_2(g).

Although IR intensities of surface and bulk-like nitrates on Pt/2.7K_2O/AZT, Pt/5.4K_2O/AZT and Pt/10K_2O/AZT became invariant at the end of 2 h of reduction at 323 K, they started to change upon heating upon H_2(g) exposure at elevated temperatures (blue colored bottom set of spectra in Figure 24b-d). While surface nitrate groups on Pt/2.7K_2O/AZT were mostly eliminated at 473 K, bulk/ionic type nitrates kept their relative presence at 473 K and the complete elimination of the latter species required a higher reduction temperature of 573 K. Materials with higher K_2O loadings (*i.e.* Pt/5.4K_2O/AZT and Pt/10K_2O/AZT) exhibited different behavior upon temperature-dependent reduction as illustrated in Figure 24c and Figure 24d. Nitrates on these materials were relatively more stable as compared to Pt/2.7K_2O/AZT (Figure 24b). In other words, these more stable bulk/ionic nitrates which were found to be more abundant on the catalysts with high K_2O loadings, were also relatively more resilient towards reduction requiring higher temperatures (573 K) for complete elimination. Thus, it can be argued that while Pt/2.7K_2O/AZT sample exhibited a noticeably higher NSC than that of K_2O-free Pt/AZT catalyst, former catalyst also revealed a comparable NO_x reduction/regeneration performance. This important finding indicates that modest K_2O loadings can enhance NSC without a significant compromise in the NO_x regeneration/reduction capability. On the other hand, NO_x regeneration/reduction characteristic of materials with higher K_2O loadings (*i.e.* Pt/5.4K_2O/AZT and Pt/10K_2O/AZT) are parallel to that of Pt/8BaO/Al and Pt/20BaO/Al, which are incapable of compete NO_x regeneration/reduction at 573 K. Consequently, we can rank the relative NO_x reduction/regeneration performances of the investigated catalysts in the following order: Pt/AZT ~ Pt/2.7K_2O/AZT> Pt/8BaO/AZT > Pt/20BaO/Al > Pt/20BaO/AZT > Pt/5.4K_2O/AZT> Pt/10K_2O/AZT.

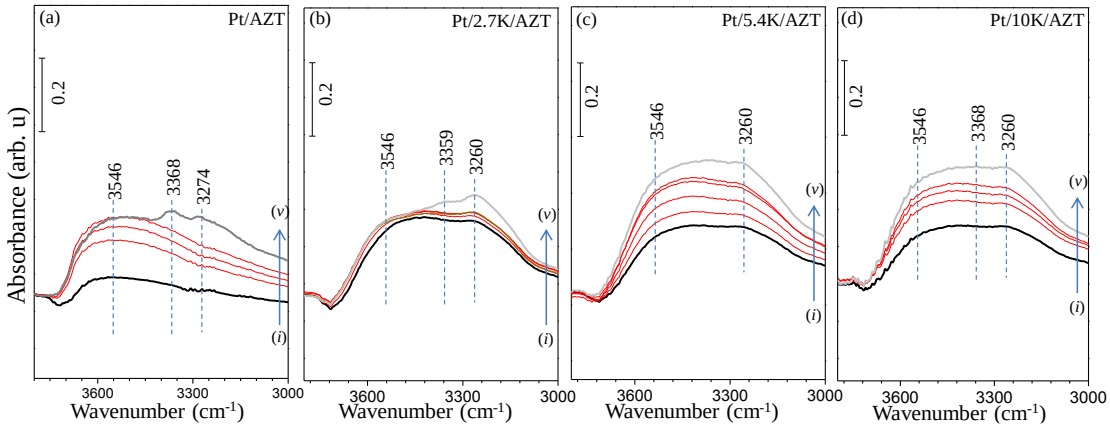

Figure 25: –OH/–NH stretching region of the in-situ FTIR spectra corresponding to NO_2 saturation *(i)* (5.0 Torr NO_2(g) for 10 min. at 323 K) followed by subsequent reduction with 15.0 Torr of H_2(g) on (a) Pt/AZT, (b) Pt/2.7K_2O/AZT, (c) Pt/5.4K_2O/AZT and (d) Pt/10K_2O/AZT at 323 K. The series of spectra *(ii), (iii), (iv) and (v)* were collected as a function of time at 3th, 10th, 30th and 120th min of reduction at 323 K; respectively.

As in the case of BaO-based AZT catalysts, correlation between the formation of bulk-like nitrate species and the generation of surface hydroxyl groups upon hydrogen reduction also exists over the K_2O-containing AZT systems. While the increase in the IR absorbance signals, regarding the surface hydroxyl groups, is quite limited for Pt/2.7K_2O/AZT, such bands are much more pronounced for the materials with higher K_2O-loading as shown in Figure 25c and Figure 25d.

Further insight regarding the nitrate reduction process in the presence of H_2(g) can be clarified by investigation of additional less-prominent features located at *ca.* 3384 and 3252 cm^{-1}. These poorly resolved and convoluted features can be attributed to the presence of –NH stretching modes associated with $–NH_2$, $–NH_3$, $–OH\cdots NH_x$ or $–OH\cdots NO_x$ species [23], [67], [89].

Aforementioned results regarding the formation of –OH and $–NH_x$ species may allow us to suggest an overall reduction pathway for the complete nitrate reduction *via* H_2(g) on Pt/5.4K_2O/AZT and Pt/10K_2O/AZT possesing relatively higher K_2O-loadings:

$$2KNO_3 + 5H_2 \Leftrightarrow N_2 + 2KOH + 4H_2O \qquad 3.5$$

Moreover, we should not disregard the re-formation of K_2O species on Pt/2.7K_2O/AZT in the absence of surface hydroxyl groups. Along these lines, an alternative overall reaction pathway for the complete nitrate reduction on Pt/2.7K_2O/AZT could be:

$$2KNO_3 + 5H_2 \Leftrightarrow N_2 + K_2O + 5H_2O \qquad 3.6$$

Finally, generation of N-H linkages on the catalyst surfaces upon nitrate reduction also indicate the presence of additional reduction products such as ammonia [113] through a general pathway given below:

$$2KNO_3 + 8H_2 \Leftrightarrow NH_3 + 2KOH + 4H_2O \qquad 3.7$$

Throughout the nitrate reduction process for all catalysts, N_2O was the only detectable gas phase feature in FTIR (*i.e.* 2225 cm^{-1}) as shown in Figure 26. However, it does not imply that N_2O is the only reduction product. NH_3 and N_2 can also be considered as other possible reduction products in the gas phase. N_2 cannot be analyzed *via* FTIR spectroscopy due to lack of a dipole moment change. On the other hand, since IR radiation passes through the air in the current experimental setup, vibration frequencies of NH_3 and H_2O in air overlap and render the detection of NH_3 rather difficult.

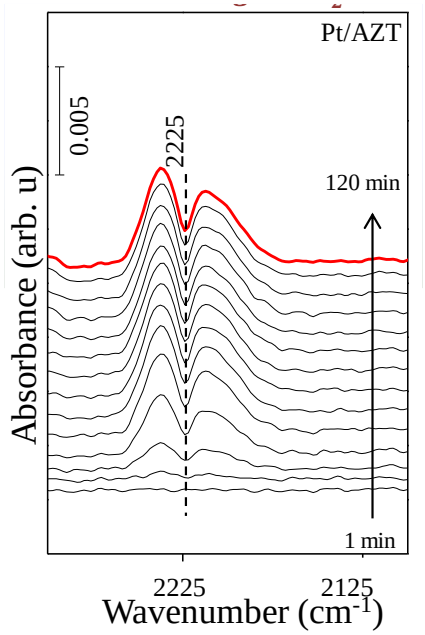

Figure 26: Time-dependent *in-situ* gas phase FTIR spectra corresponding to nitrate reduction via 15.0 Torr of H_2(g) on $Pt/Al_2O_3/ZrO_2/TiO_2$ at 323 K for 120 min. Red spectrum in each panel corresponds to the last spectrum obtained at the end of the given time interval.

Identical time-dependent series of FTIR spectra were also collected for all other synthesized materials. While N_2O formation in gas phase was obvious to follow, NH_3 and N_2 could not be detected.

3.2.3 SO_x Adsorption Properties.

In these set of experiments, SO_x adsorption characteristics of synthesized materials were studied as a function of catalyst temperature and catalyst composition by means of *in-situ* FTIR spectroscopy.

3.2.3.1 SO_x Adsorption on Binary and Ternary Support Oxides

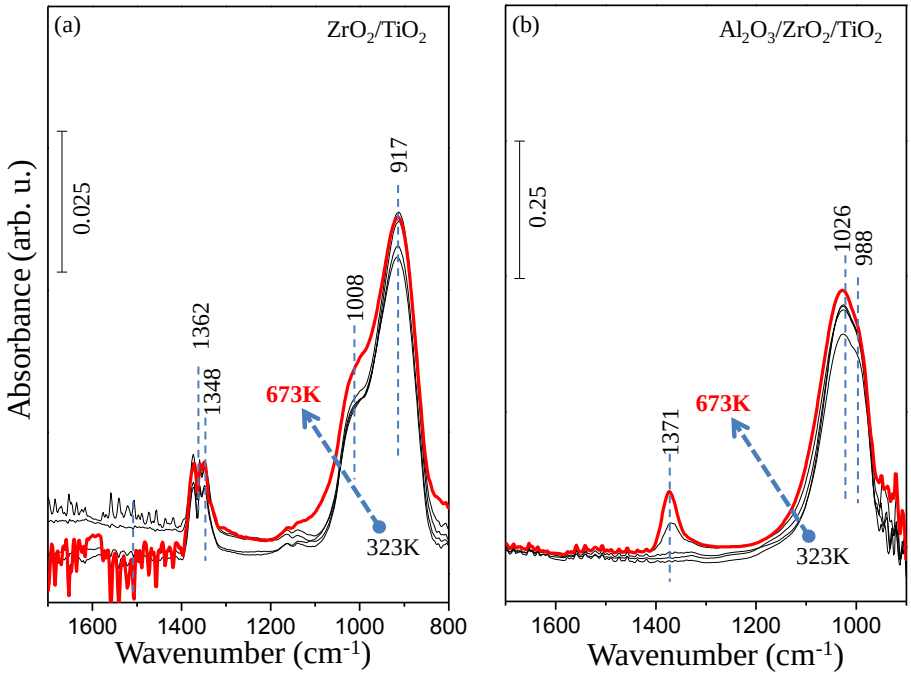

Figure 27: FTIR spectra corresponding to SO_x uptake/adsorption properties of (a) ZT and (b) AZT. Bottom black set of spectra in each panel were acquired after SO_x exposure (2.0 Torr, SO_2:O_2 = 1:10) at 323 K, followed by annealing at 373, 473, 573 K (black spectra) and 673 K (red spectra) in the SO_x gas mixture for 5 min. All spectra were recorded at 323K.

Figure 27 represents temperature-dependent SO_x adsorption experiments on ZrO_2/TiO_2 and $Al_2O_3/ZrO_2/TiO_2$material surfaces upon exposure to 2.0 Torr of SO_2+O_2 gas mixture (SO_2:O_2 = 1:10); respectively. While the black-colored spectra

in each panel correspond to the sulfation at increasing temperatures within 323 - 573 K, topmost red spectra were recorded after sulfation at 673 K. In Figure 27a, three major vibrational frequencies were observed at 1348, 1008 and 917 cm^{-1} on ZrO_2/TiO_2. While the vibrational features at 1008 and 917cm^{-1} can be attributed to surface sulfite (SO_3^{2-}) species, weak feature at 1348 cm^{-1} can be attributed to the antisymmetric stretching of surface sulfate (SO_4^{2-}) groups [114]–[118]. Since these set of spectra were recorded in the gas mixture, antisymmetric stretching of SO_2(g) molecule is also visible at 1362 cm^{-1}. The line shape of the spectrum recorded at 323 K and 673 K is almost identical to each other, indicating SO_x species were not significantly altered by the increase in temperature.

Identical set of spectra were also collected for $Al_2O_3/ZrO_2/TiO_2$ ternary mixed oxide as illustrated in Figure 27b. $Al_2O_3/ZrO_2/TiO_2$ surface reveals two major vibrational features located at 1026 and 988 cm^{-1} in the temperature range of 323-473 K which can be assigned for sulfate (SO_4^{2-}) and sulfite(SO_3^{2-}) functional groups; respectively. Absorbance intensities of these two particular vibrational frequencies are similar at low temperatures. However SO_4^{2-} species start to dominate sulfite species with increasing temperature. Thermal oxidation of sulfite species to sulfate species can also be followed by the appearance of antisymmetric stretching mode of sulfate groups located at 1371 cm^{-1}. Higher oxidation capability of the ternary oxide system can originate from the disordered and amorphous structural characteristics which lead to almost ten-fold greater SO_x IR absorbance intensities as compared to that of ZrO_2/TiO_2 given in Figure 27a.

3.2.3.2 SO_x Adsorption on Pt-functionalized Binary and Ternary Oxides

Figure 28 illustrates a series of *in-situ* FTIR spectra for Pt/ZT and Pt/AZT surfaces collected in the presence of SO_2+O_2 mixture as a function of temperature. In Figure 28a, SO_x adsorption on the Pt/ZT surface at relatively lower temperatures (i.e. 323 and 373K) reveals two main vibrational features located at 1007 and 920 cm^{-1}. As discussed in the previous section, these features are attributed to sulfate and sulfite species; respectively.

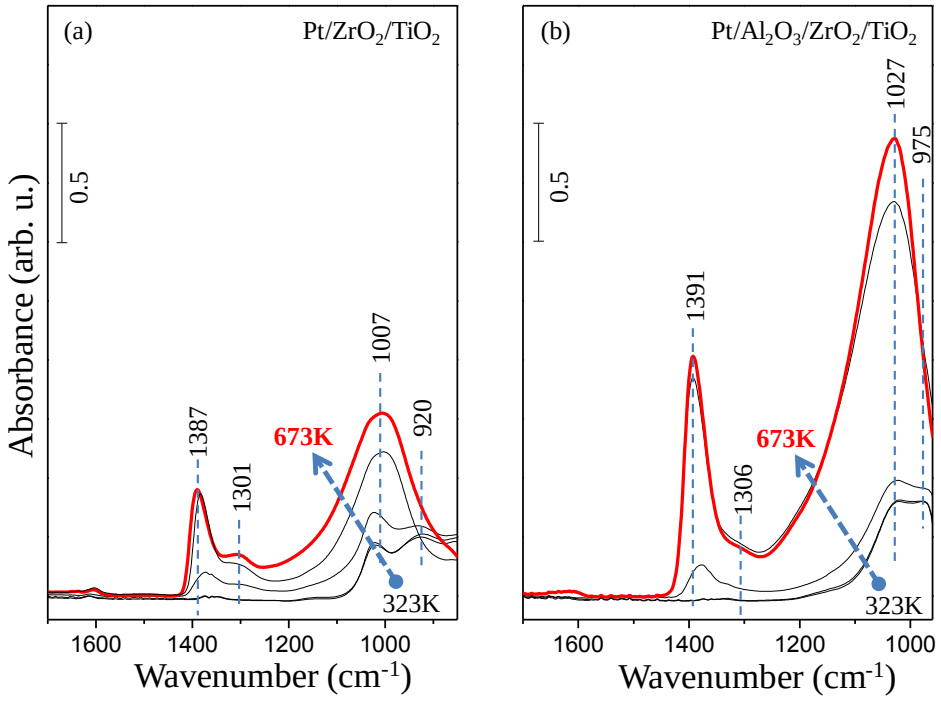

Figure 28: FTIR spectra corresponding to SO_x uptake/adsorption properties of (a) Pt/ZT and (b) Pt/AZT. Black set of spectra in each panel were acquired after SO_x exposure (2.0 Torr, SO_2:O_2 = 1:10) at 323 K, followed by annealing at 373, 473, 573 K (black spectra) and 673 K (red spectra) in the SO_x gas mixture for 5 min. All spectra were recorded at 323 K.

Relative absorbance intensities of these two features change with varying temperature, where surface sulfate (i.e. 1007 cm^{-1}) features become relatively more pronounced. Oxidation of sulfite groups into sulfate groups are also evident by the generation of additional features located at 1387 and 1301 cm^{-1} which can be assigned to bidentate and tridentate surface sulfate species; respectively. This sulfation behavior repeats itself for the Pt/AZT sample which exhibits almost identical vibrational characteristics as shown in Figure 28b.

Unlike the Pt-free ZT and AZT systems, it was observed that the SO_x oxidation capacities of Pt-containing ZT and AZT support materials are close to each other emphasizing the critical role of Pt-sites in the catalytic oxidation of SO_x species.

3.2.3.3 SO_x Adsorption on Pt-functionalized Ternary Oxides with Basic Storage Domains

Figure 29a-d present temperature-dependent SO_x adsorption (2.0 Torr of SO_2+O_2 gas mixture, SO_2:O_2 = 1:10) on Pt/AZT, Pt/8BaO/AZT, Pt/20BaO/AZT and Pt/20BaO/Al (benchmark) catalyst; respectively. While the black-colored spectra in each panel correspond to the exposures within 323 - 573 K, topmost red spectra are recorded after poisoning at 673 K. Addition of BaO basic domains onto AZT ternary oxide system results in a significantly different spectral line shape as compared to that of BaO-free samples while BaO-containing materials exhibited quite similar spectral characteristics among themselves (Figure 29b-d). Figure 29 suggests that SO_x oxidation starts to occur at T > 473 K for all of the investigated catalysts therein.

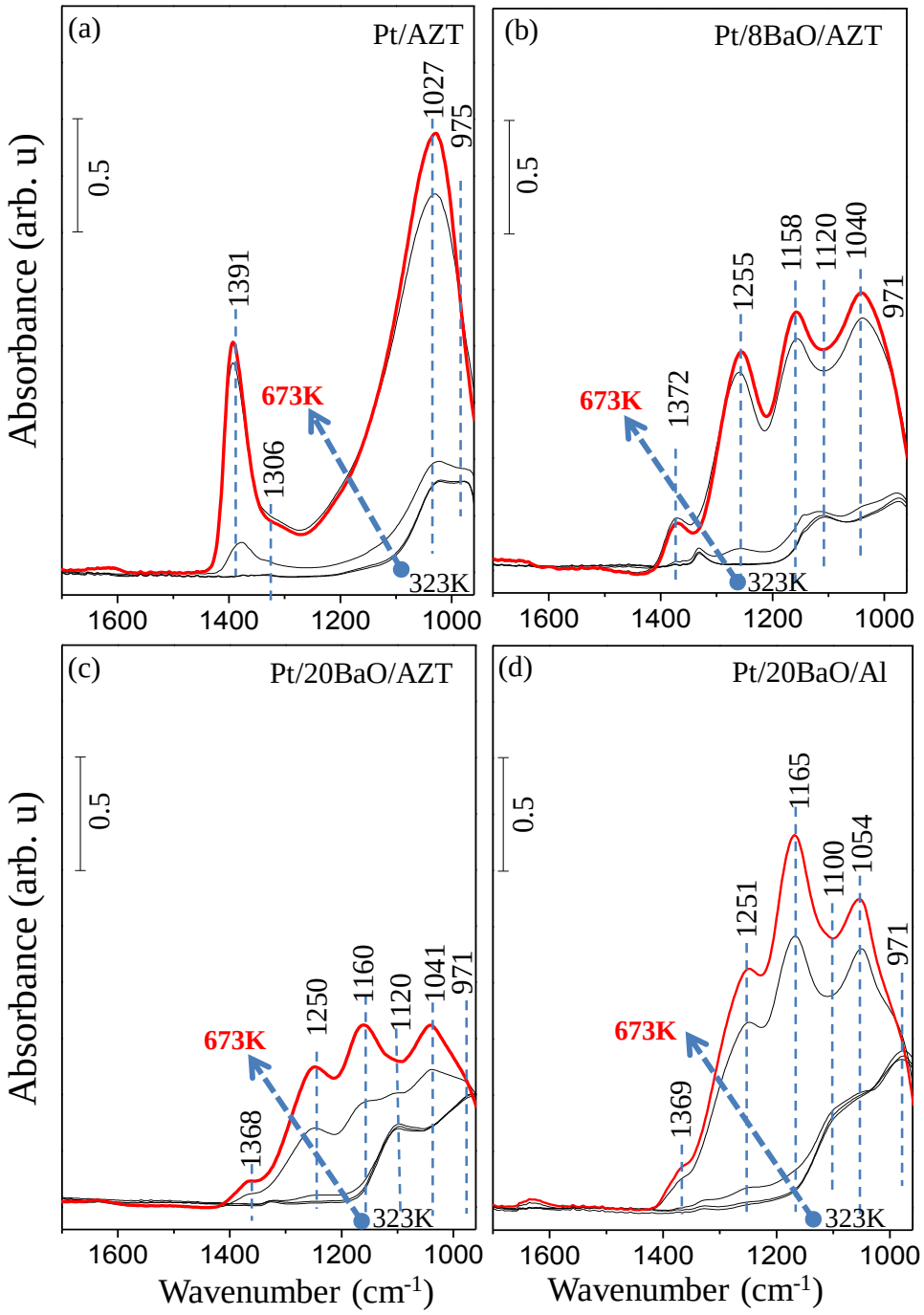

Figure 29:FTIR spectra corresponding to SO_x uptake/adsorption properties of (a) Pt/AZT, (b) Pt/8BaO/AZT, (c) Pt/20BaO/AZT and (d) Pt/20BaO/Al. Black set of spectra in each panel were acquired after SO_x exposure (2.0 Torr, SO_2:O_2 = 1:10) at 323 K**,** followed by annealing at 373, 473, 573 K (black spectra) and 673 K (red spectra) in the SO_x gas mixture for 5 min. All spectra were recorded at 323 K.

. At relatively lower temperatures (323-473K), only two main vibrational features located at 1120 and 970 cm^{-1} that is due to surface sulfates (SO_4^{2-})and sulfites (SO_3^{2-}) are visible in Figure 29 [52]. As the sulfation temperature is increased to higher temperatures (573-673 K), the adsorption of sulfate/sulfite groups change their characteristics revealing four major vibrational features at 1370, 1250, 1160 and 1040 cm^{-1} (Figure 29b-d red spectra). While the features *ca.* 1250 and 1160 cm^{-1} are attributed to bulk-like sulfates on BaO (i.e. $BaSO_4$), remaining couple of signals can be assigned to surface sulfate groups on either AZT support and/or BaO domains [24], [52], [53], [119].

It is not that much feasible to obtain quantitative poisoning information by comparing differences in integrated IR absorbance intensities. In order to have a better understanding regarding quantitative sulfur uptake, TPD experiments were performed for each sample as illustrated in the forthcoming sections.

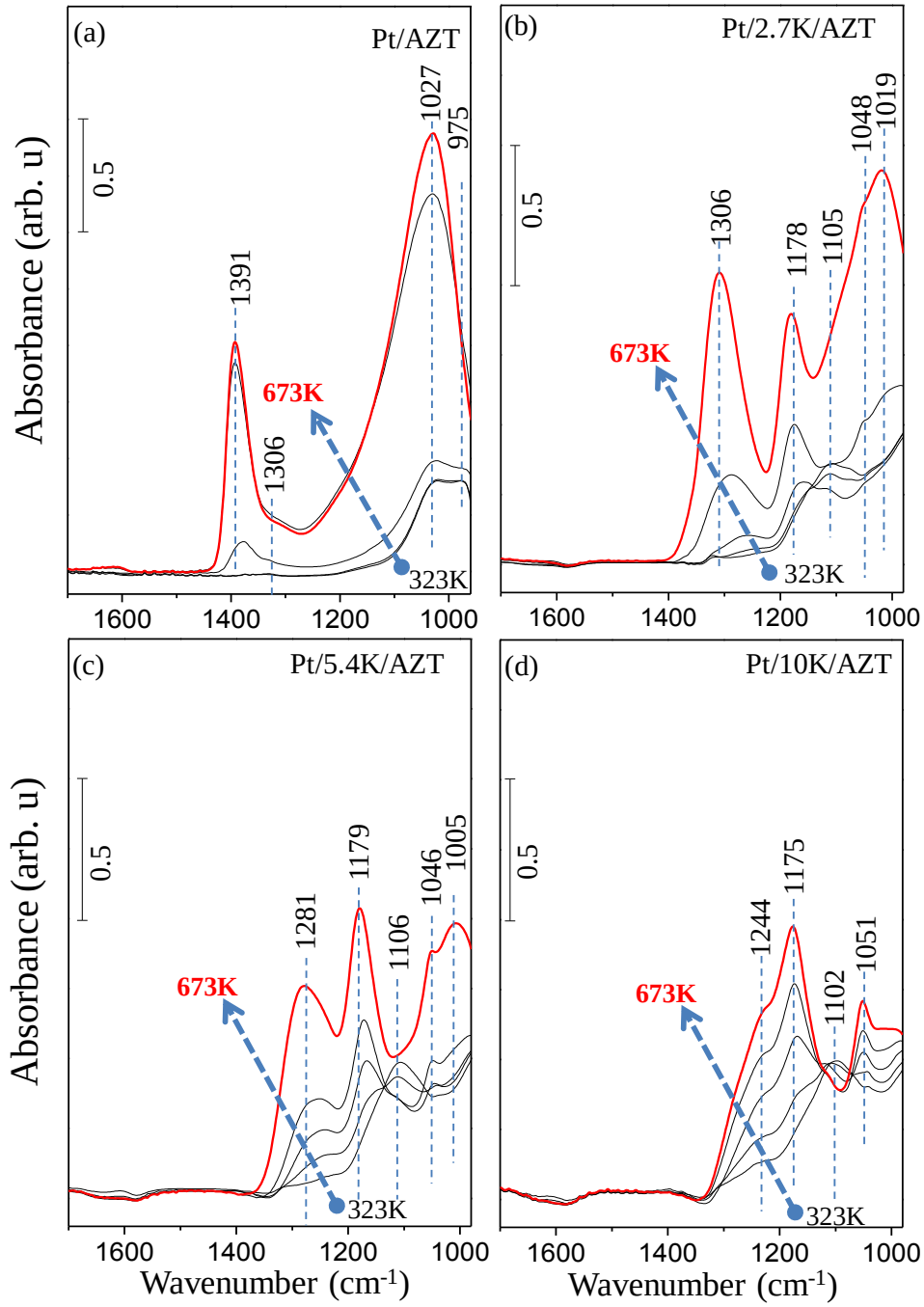

Figure 30: FTIR spectra corresponding to SO_x uptake/adsorption properties of (a) Pt/AZT, (b) Pt/2.7K_2O/AZT(c) Pt/5.4K_2O/AZT and (d) Pt/10K_2O/AZT surfaces. Black set of spectra in each panel were acquired after SO_x exposure (2.0 Torr, SO_2:O_2 = 1:10) at 323 K, followed by annealing at 373, 473, 573 K (black spectra) and 673 K (red spectra) in the SO_x gas mixture for 5 min. All spectra were recorded at 323 K.

Identical set of experiments were also carried out for K_2O-functionalized materials in order to investigate their surface characteristics during interaction with SO_x (*i.e.* sulfur poisoning). Szanyi *et al.* reported that increase in K_2O loading from 2 wt. % to 30 wt. % led to an increase in NO_x storage capacity of $Pt/K_2O/Al_2O_3$ catalysts in the temperature range of 600-800 K [107]. However, in the current study, we limited the K_2O loading of the AZT-based NSR/LNT materials to values less than 10 wt.% due to the irreversible sulfur poisoning for K_2O loadings above 10 wt. %, as will be discussed below.

Figure 30a-d illustrate the SO_x uptake of Pt/AZT, $Pt/2.7K_2O/AZT$, $Pt/5.4K_2O/AZT$ and $Pt/10K_2O/AZT$ surfaces upon exposure to 2.0 Torr of SO_2+O_2 gas mixture ($SO_2:O_2$ = 1:10), at various temperatures; respectively. $Pt/2.7K_2O/AZT$ revealed five major vibrational strechings located at *ca.* 1306, 1178, 1105, 1048 and 1019 cm^{-1}(Figure 30b). While the IR bands at 1306, 1105, 1048 and 1019 cm^{-1} can be attributed to the surface sulfate (SO_4^{2-}) groups on K_2O and/or AZT support, vibrational feature located at 1178 cm^{-1} is associated with bulk-like sulfate groups on K_2O [52], [60]. This latter feature becomes more discernible with an increase in the K_2O loading (*i.e.* 5.4 wt. % and 10 wt. %) evident by the increasing relative absorbance intensity of the 1178 cm^{-1} signal in Figures 30c and 30d. Moreover, SO_x adsorption on $Pt/5.4K_2O/AZT$ and $Pt/10K_2O/AZT$ materials at 673 K leads to vibrational features at 1281 and 1238 cm^{-1} along with the absence of any significant vibrational bands located at *ca.* >1300 cm^{-1} (Figures 30c and 30d). The vibrational signals at 1281 and 1238 cm^{-1} can be assigned to predominantly sulfates on K_2O domains [24], [52], [119].

It can be argued that with increasing K_2O loading, an increasingly larger portion of the AZT surface is covered by K_2O islands/domains, decreasing the extent

of exposed/uncovered AZT surface. It is also likely that the increase in the K_2O loading also results in the growth of the K_2O particle size and formation of 3D agglomerates, enabling the storage of SO_x in the form of bulk-like sulfates in the sub-surface of these 3D nanoparticles. Furthermore, these findings can be also supported by the absence of vibrational features located at 1391 and 1306 cm^{-1} on Pt/5.4K_2O/AZT and Pt/10K_2O/AZT which are readily observable on Pt/AZT and Pt/2.7K_2O/AZT. That is, AZT adsorption sites are significantly suppressed and highly occupied/covered by K_2O islands at high loadings.

3.2.4 SO_x Reduction Properties

As well as sulfur adsorption properties of the investigated materials, their reduction/regeneration performances also have significant influence on the catalyst life time and NO_x storage capacities. Therefore, SO_x reduction characteristics of the synthesized materials were studied as a function of the catalyst temperature by means of *in-situ* FTIR spectroscopy.

3.2.4.1 SO_x Reduction on Pt-functionalized Binary and Ternary Oxides

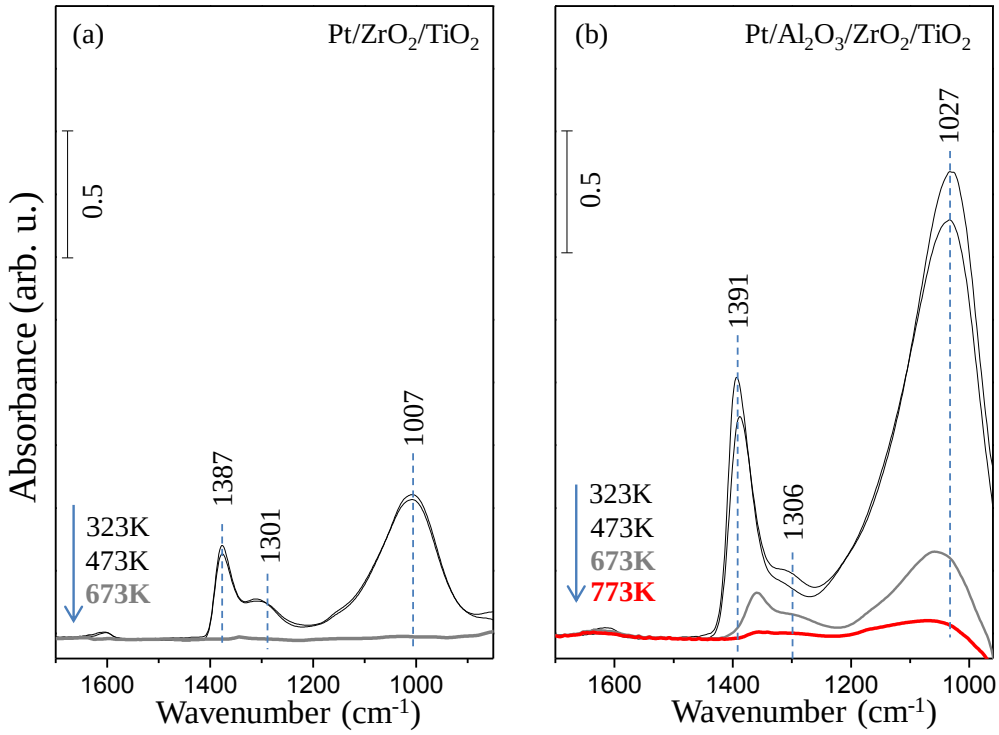

Figure 31: FTIR spectra corresponding to SO_x release/desorption properties of (a) Pt/ZT and (b) Pt/AZT. Catalystswere initially pre-sulfated (2.0 Torr, SO_2:O_2 = 1:10 for 5 min at 673 K) and then exposed to H_2(g) (15.0 Torr), at 323, 473, 673, 773 K for 5 min. All spectra were recorded at 323 K.

Figure 31a and Figure 31b illustrate a change in S-related surface functional groups on Pt/ZT and Pt/AZT catalyst surfaces as a function of temperature in between 323-773 K in the presence of an external reducing agent, H_2(g); respectively. For these set of experiments, catalysts were initially saturated with a 2.0 Torr of SO_2+O_2 gas mixture (SO_2:O_2 = 1:10) at 673 K for 5 min and then cooled to 323 K followed by the evacuation of the spectroscopic reactor, introduction of 15.0 Torr H_2(g) at 323 K and annealing in H_2(g) at the given temperatures in between 323 and 773 K. This selected temperature (*i.e.* 673 K) of sulfur adsorption was determined based not only on real NSR operational temperature, but also generation of the strongest IR absorption intensities.

In-situ FTIR spectra acquired immediately after the sulfur poisoning at 673 K (data not shown here) and after the H_2(g) introduction were identical to that of the topmost spectra given in Figure 31. In other words, H_2(g) exposure at 323 K has no detectable influence on the vibrational features of the SO_x species residing on the catalyst surfaces. In Figure 31a and Figure 31b, it is seen that at the beginning of the reduction series (*i.e.* after 323 K H_2(g) exposure) SO_x-saturated Pt/ZT and Pt/AZT ternary oxide reveals three main features roughly located at 1390, 1300 and 1020 cm^{-1}. Although these vibrational features are fairly difficult to analyze due to their highly convoluted nature, as clearly stated in previous SO_x adsorption section, they can be attributed to antisymmetric and symmetric vibration modes of surface sulfates (SO_4^{2-}); respectively [114]–[118].

As indicated in Figure 31a, no significant changes in surface functional groups on Pt/ZT surface were observed upon heating up to 473K which were then completely removed at 673K (bottom gray spectrum). These set of reduction

experiments were also carried out for Pt/AZT materials which has much higher surface area and amorphous like structure. Depending on relative absorbance intensities of both materials, we can initially deduce that Pt/AZT has much higher sulfur uptake than Pt/ZT. This result can directly be attributed to higher surface area of ternary oxide support. On the other hand, thermal stabilities of adsorbed sulfur species are much stronger on Pt/AZT. These species did not reveal any change upon heating up to 673K in H_2(g) and catalyst is completely regenerated at 773K.

3.2.4.2 SO_x Reduction on Pt-functionalized Binary and Ternary Oxides with Basic Storage Domains

Pt/AZT ternary oxide system which has limited NSR activity was modified by the incorporation of BaO domains serving as NO_x storage functionalities with different mass percentiles (*i.e.* 8 and 20 wt. % BaO) and analyzed in an analogous manner. *In-situ* FTIR spectra in Figure 32b and 32c represent SO_x reduction characteristics of the poisoned Pt/8BaO/AZT and Pt/20BaO/AZT catalysts; respectively, while Figure 32d shows the corresponding results for the conventional NSR catalyst (*i.e.* Pt/20BaO/Al) as the benchmark sample.

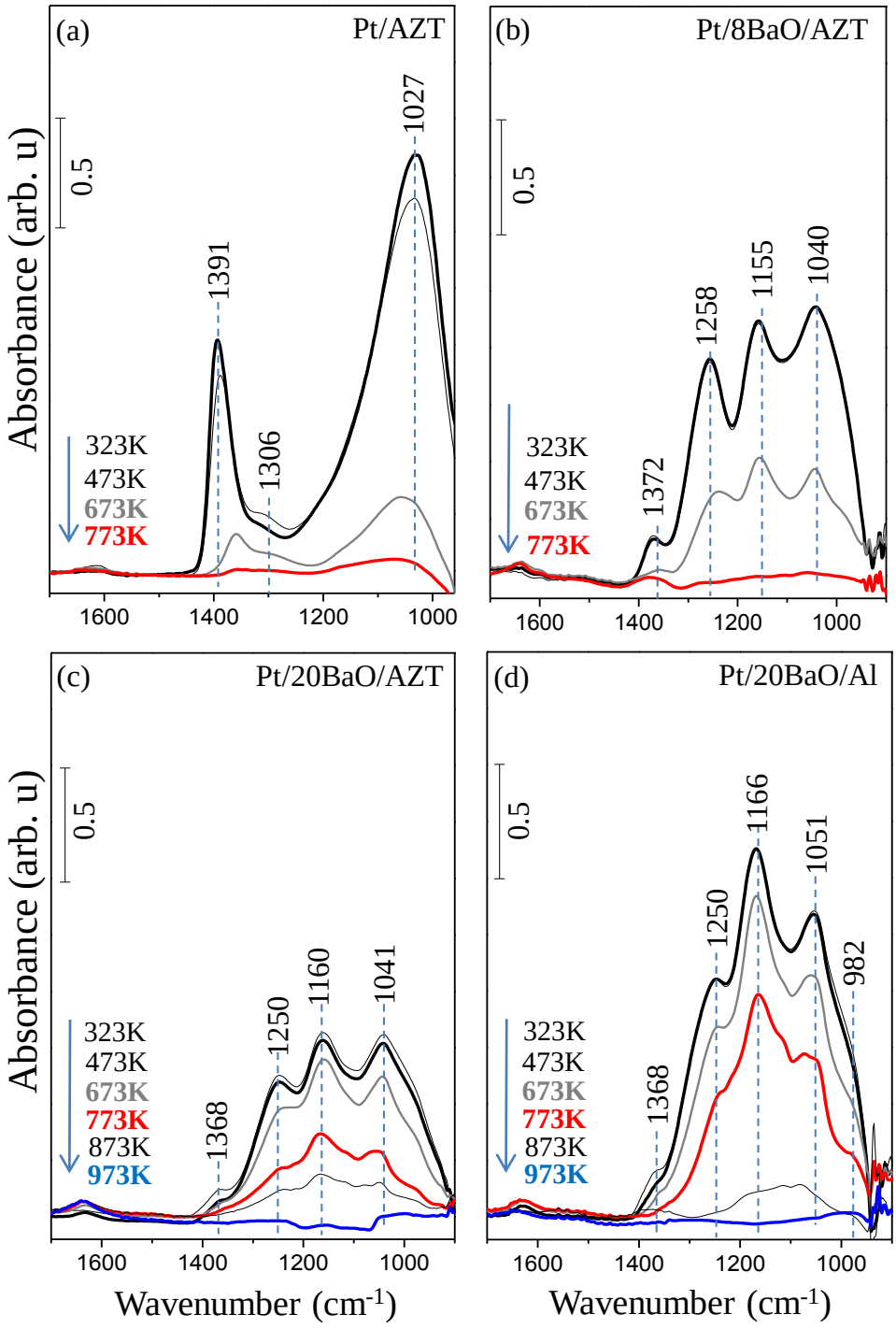

Figure 32: FTIR spectra related to SO_x release/desorption properties of (a) Pt/AZT, (b) Pt/8BaO/AZT, (c) Pt/20BaO/AZT and (d) Pt/20BaO/Al. Catalystswere initially pre-sulfated (2.0 Torr, SO_2:O_2 = 1:10 for 5 min at 673 K) and then exposed to H_2(g) (15.0 Torr), at 323, 473, 673, 773, 873 and 973 K for 5min. All spectra were recorded at 323 K.

It can be seen in Figures 32b-32d that adsorption geometries of SO_x species on poisoned BaO-containing catalysts (*i.e.* spectra corresponding to 323 K in Figures 24b-24d) are rather similar as evident by the analogous vibrational features observed for these samples. The topmost FTIR spectra displayed in Figures 32b-32d reveal four main vibrational features located at *ca.*1370, 1250, 1160 and 1040 cm^{-1}. While the vibrational signatures at 1250 and 1160 cm^{-1}can be attributed to bulk-like sulfates on BaO (*i.e.*$BaSO_4$), the remaining two features can be assigned to surface sulfate groups located on the BaO domains or residing on the support surface (*i.e.* AZT or γ-Al_2O_3). In addition to these features, rather convoluted vibrational signatures can be detected as a shoulder at 970-980 cm^{-1} corresponding to surface sulfites (SO_3^{-2}) [114]–[118].

Figure 32 suggests that within the temperature range of 323-473 K, SO_x species on the investigated catalysts are relatively stable in the presence of excess H_2(g). However, above 473 K, the sulfate/sulfite groups start to react with H_2(g), possibly forming H_2S(g). H_2S(g) evolution was reported in one of our former TPD studies on SO_x-poisoned γ-Al_2O_3, TiO_2 (anatase) as well as TiO_2/Al_2O_3 binary oxide surfaces [53]. However it is very likely that the generated H_2S(g) in the current experiments is below the detection limit of the FTIR spectroscopic analysis method.

Increasing the temperature to 673 K in the presence of H_2(g) causes a significant attenuation of all of the SO_x-related vibrational features of the Pt/AZT catalyst (Figure 32a), where the complete regeneration can be achieved at 773 K (bottommost/red spectrum in Figure 32a). Figure 32b indicates that as in the case of Pt/AZT, complete SO_x elimination from the surface can also be achieved for Pt/8BaO/AZT at $T \geq 773$ K. On the other hand, for Pt/20BaO/AZT and the

benchmark Pt/20BaO/Al catalyst, complete sulfur elimination in the presence of H_2(g) occurs only at T ≥ 973K (bottommost/blue spectra in Figures 32c and 32d). The differences in the relative thermal stabilities of the SO_x species formed on the Pt/AZT, Pt/8BaO/AZT, Pt/20/BaO/AZT and Pt/20BaO/Al catalysts will be further discussed in the next section regarding the TPD experiments under vacuum.

Figure 32 suggests that the Pt/AZT ternary oxide catalyst shows better sulfur regeneration characteristics than the conventional Pt/20BaO/Al catalyst or the Pt/8BaO/AZT and Pt/20BaO/AZT catalysts. However, it should be emphasized that Pt/AZT is not necessarily an ideal NSR catalyst, as the lack of a basic oxide component such as BaO in its formulation significantly limits the NSC of this material.

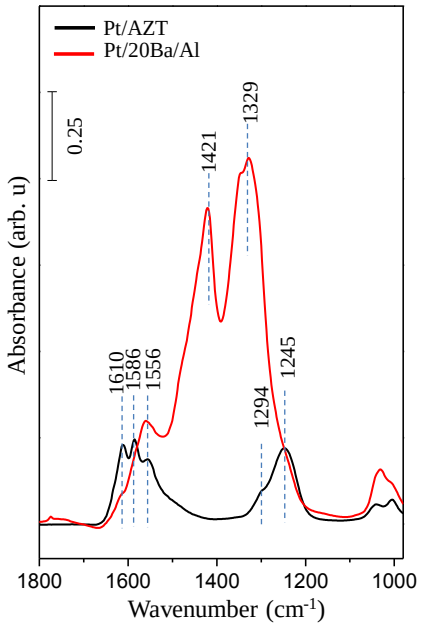

Figure 33: FTIR spectra corresponding to Pt/20BaO/Al (red spectra) and Pt/AZT (black spectra) catalysts after 5.0 Torr NO_2 exposure at 573 K for 10 min and subsequent evacuation. All spectra were recorded at 323 K.

This is illustrated in Figure 33 showing the *in-situ* FTIR spectra for the clean Pt/AZT versus Pt/20BaO/Al which were saturated with 5.0 Torr NO_2(g) at 573 K for 10 min. It is difficult to make a precise quantitative comparison of the amount of NO_x species adsorbed on Pt/AZT versus Pt/20BaO/Al solely based on the integrated FTIR intensities (due to the differences in the IR absorption cross sections of dissimilar oscillators and vibrational intensity transfer processes between oscillators [120]). However one can still qualitatively argue that Pt/AZT sample lacking any NO_x storage component (*i.e.* BaO) adsorbs a lower quantity of NO_x with respect to that of the Pt/BaO/Al benchmark catalyst during the batch-mode *in-situ* FTIR spectroscopic measurements described above.

SO_x reduction/regeneration/removal experiments were also carried out for K_2O-based materials under identical experimental conditions. Figure 34a-d demonstrates the changes in surface functional groups on Pt/AZT, (b) Pt/2.7K_2O/AZT(c) Pt/5.4K_2O/AZT and (d) Pt/10K_2O/AZT; respectively. Since the detailed analysis of S-related vibrational features on K_2O-based materials were given in previous sections, we will only focus on the thermal stabilities of SO_x groups under H_2 atmosphere in the temperature range of 323-873 K.

In the series of experiments given in Figure 34, spectral line shapes do not typically change in a noteworthy manner at reduction temperatures $\leq$ 473 K. However, increasing the reduction temperature to 673 K (gray spectra in Figures 34a-34c) leads to noticeable alterations in the FTIR spectra, where bulk and surface sulfate/sulfite species significantly attenuate for Pt/AZT, Pt/2.7K_2O/AZT and Pt/5.4K_2O/AZT.

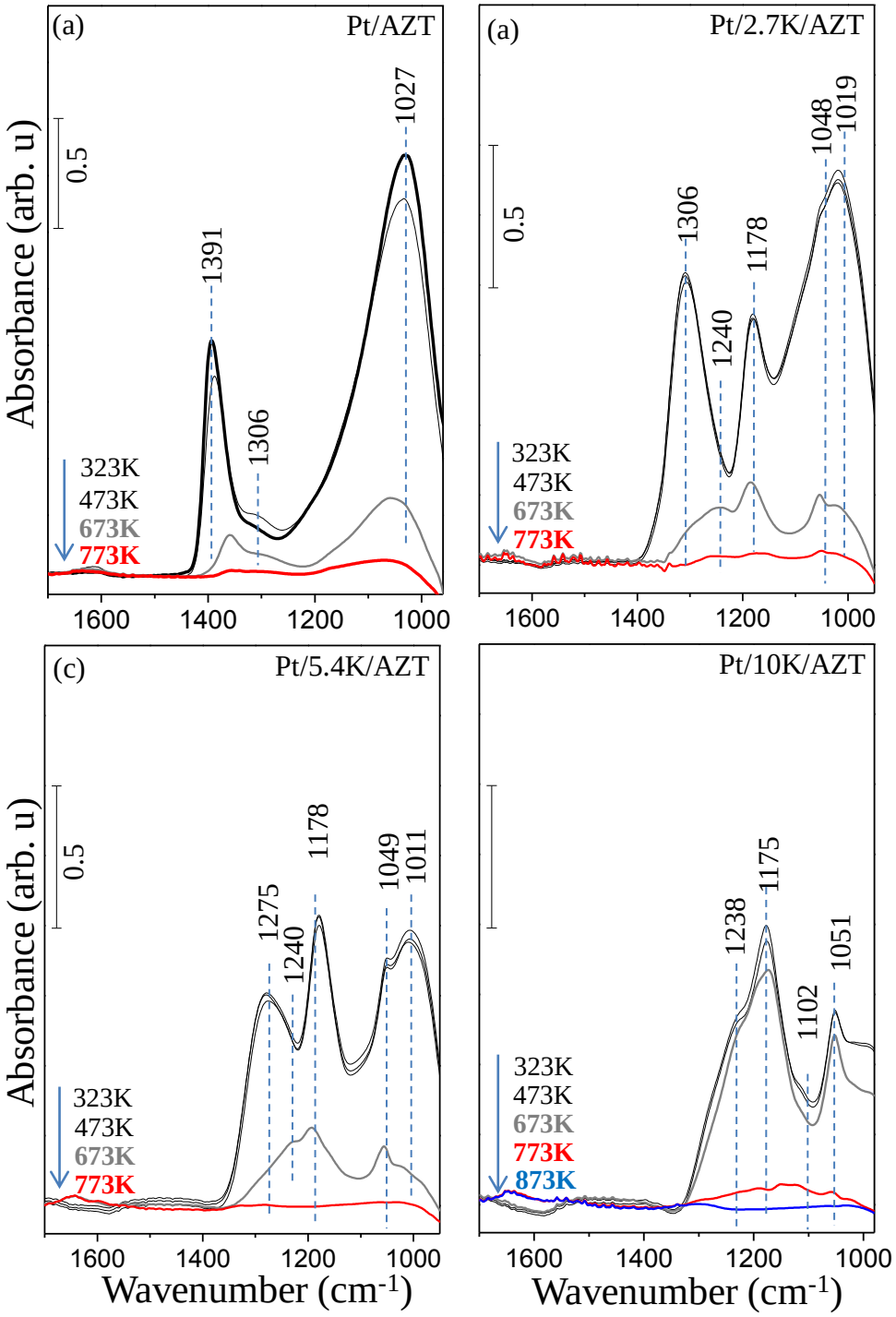

Figure 34: FTIR spectra related to SO_x release/desorption properties of (a) Pt/AZT, (b) Pt/2.7K_2O/AZT (c) Pt/5.4K_2O/AZT and (d) Pt/10K_2O/AZTmaterials. Catalystswere initially pre-sulfated (2.0 Torr, SO_2:O_2 = 1:10 for 5 min at 673 K) and then exposed to H_2(g) (15.0 Torr), at 323, 473, 673, 773, 873 and 973 K for 5 min. All spectra were recorded at 323 K.

Increasing the temperature to 773 K in the presence of H_2 leads to the complete elimination of the SO_x-related vibrational signatures on Pt/AZT, Pt/2.7K_2O/AZT and Pt/5.4K_2O/AZT surfaces (red spectra in Figures 34a-34c). However, AZT-based catalysts with the highest K_2O loading used in the current study (*i.e.* Pt/10K_2O/AZT) not only showed unique sulfur uptake characteristics as presented in Figure 30d which is dominated by bulk-like sulfates, but also revealed a fairly different SO_x-reduction profile in the presence of H_2(Figure 34d). As can be seen in Figure 34, at relatively low temperatures (i.e. $T \leq 673$ K), a significant portion of the SO_x species can already be eliminated from Pt/AZT, Pt/2.7K_2O/AZT and Pt/5.4K_2O/AZT surfaces. However, at $T \leq 673$ K, almost all of the S-related surface functional groups remain intact on Pt/10K_2O/AZT.

Here, it is worth summarizing that temperature required (*i.e.* 773 K) for complete sulfur regeneration is almost identical for the Pt/AZT, Pt/8BaO/AZT, Pt/2.7K_2O/AZT and Pt/5.4K_2O/AZT materials. However, sulfate/sulfite groups on Pt/20BaO/AZT, Pt/20BaO/Al_2O_3, and Pt/10K_2O/AZT are observed to be much more resilient against thermal annealing and require higher temperatures for complete sulfur regeneration.

3.3 Temperature Programmed Desorption (TPD) Analysis

3.3.1 NO_x Adsorption and Desorption Properties*via* TPD

3.3.1.1 NO_x TPD on Binary and Ternary Oxides

NO_x adsorption and desorption properties of synthesized materials *viain-situ* FTIR analysis yields predominantly qualitative information. In this section, FTIR experiments were combined together with TPD analysis in order to gather quantitative insight regarding the total NO_x adsorption quantities and thermal stabilities of adsorbed nitrate/nitrite species. Figure 35a and Figure 35b illustrate the TPD profiles of ZT and AZT materials after NO_2(g) saturation (5.0 Torr for 10 min) at 323 K; respectively. In comparison, NO_x desorption characteristics of ZT and AZT materials revealed completely different pathways in TPD analysis. While nitrate/nitrite groups were completely removed below 800 K, NO_x desorption from AZT surface did not cease even at 973 K. Nitrate decomposition from both materials led to a major desorption signal related to NO (*m/z*=30) together with other desorption features of N_2, O_2, N_2O and NO_2. In Figure 35a, two major NO (*m/z*=30) desorption maxima upon nitrate decomposition for the ZT sample located at 640 and 750 K were observed. For the low temperature desorption state at 640 K, nitrate decomposition from ZT surface generated simultaneous evolution of NO, O_2, N_2O and NO_2corresponding to *m/z* signals at 30, 32, 44 and 46; respectively. High temperature desorption state at 750 K, however revealed NO and N_2O signal together with lesser contributions from O_2 and NO_2.

In contrast, nitrate decomposition from AZT surface shows completely different characteristics where NO_x desorption was not completed within the temperature window of 323-973 K. Major NO (*m/z*=30) desorption line grew

continuously with increasing desorption temperature. This behavior indicates that nitrates are found in thermally more stable states on AZT as compared to that of ZT surface. This result is in good agreement with the previously discussed H_2 reduction experiments (see section 3.2.2.1) and can indirectly be correlated to the existence of a large concentration of surface defects and coordinatively unsaturated adsorption sites which are present on the disordered/poorly crystalline AZT surface revealing a higher SSA.

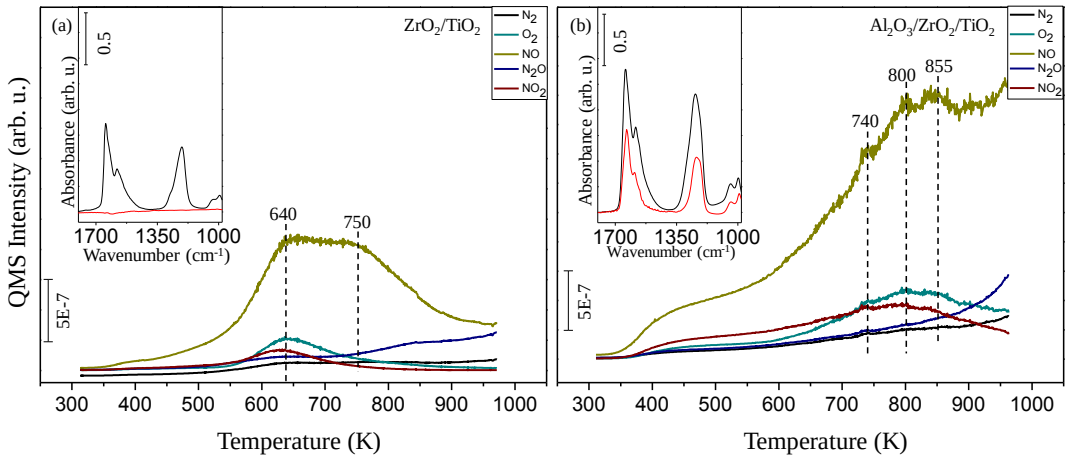

Figure 35: TPD profiles obtained from (a) ZT and (b) AZTsamples after saturation with 5 Torr NO_2(g) at 323 K for 10 min. The inset in each panel presents the FTIR spectra of the surfaces before (black) and after (red) TPD analysis. Copyright 2014 Elsevier B.V. [67].

Quantitative analysis of the integrated TPD signals were made using the corresponding mass spectroscopic fragmentation factors for some of the major gas phase species of interest namely, NO_2, NO, N_2O and N_2 [67]. For the calculation of the total integrated TPD signal of NO_2, m/z = 30 and m/z=46 channels were considered. Analysis of a pure NO_2(g) sample using the current QMS (SRS RGA 200) yields m/z = 30 to m/z=46 intensity ratio of 3.23. Hence in order to calculate the

NO_2 TPD signal before fragmentation, m/z=46 integrated signal (I46) should be multiplied by a factor of 3.23+1.00 = 4.23. This value is denoted as "λ".

For the calculation of the total integrated TPD signal of N_2O, m/z = 30 and m/z=44 channels were considered. A pure N_2O(g) sample yields a m/z = 30 to m/z= 44 intensity ratio of 0.34 upon fragmentation in the QMS. Hence in order to calculate the N_2O TPD signal before fragmentation, m/z=44 integrated signal (I44) should be multiplied by a factor of 0.34+1.00 = 1.34. This value is denoted as "α".

For the calculation of the total integrated TPD signal of NO(g), m/z = 30 channel was considered. However, m/z = 30 channel also has contributions from N_2O(g) and NO_2(g). Thus in order to calculate the net NO(g) integrated signal (β), contributions from N_2O(g) and NO_2(g) should be subtracted from the integrated m/z = 30 signal (I30). Contribution of NO_2(g) in m/z = 30 signal is 3.23 times the m/z = 46 signal, while contribution of N_2O(g) in m/z = 30 signal is 0.34 times the m/z = 44 signal.

For the calculation of the total integrated TPD signal of N_2(g) (i.e. θ), m/z = 28 channel was considered. However, m/z = 28 channel also has contributions from N_2O(g). Thus in order to calculate the net N_2(g) integrated signal (θ), contributions from N_2O(g) should be subtracted from the integrated m/z = 28 signal (I28). Contribution of N_2O(g) in m/z = 28 signal is 0.11 times the m/z = 44 signal.

$$\lambda = \text{Quantity of NO2} = \left(\int \text{I46}.\Delta\text{T}\right) \times 4.23$$

$$\alpha = \text{Quantity of N2O} = \left(\int \text{I44}.\Delta\text{T}\right) \times 1.34$$

$$\beta = \text{Quantity of NO} = \left(\int \text{I30}.\Delta\text{T}\right) - \left(\int \text{I46}.\Delta\text{T}\right) \times 3.23 - \left(\int \text{I44}.\Delta\text{T}\right) \times 0.33$$

$$\theta = Quantity\ of\ N2 = \left[\left(\int I28.\Delta T\right) - \left(\int I44.\Delta T\right) \times 0.11\right]$$

In order to calculate the total number of NO_2 molecules adsorbed on the surface, one needs to consider nitrogen mass balance. Taking account of the fact that each desorbing N_2(g) and N_2O(g) molecule originates from two nascent adsorbed NO_2(ad), while each desorbing NO(g) and NO_2(g) molecule originates from a single nascent adsorbed NO_2(ad), total amount of adsorbed NO_x species can be estimated as follows:

$$\sum NSC = \lambda + 2\alpha + \beta + 2\theta$$

In the light of these detailed calculations mentioned in above equations, comparison of the TPD signal intensities for ZT and AZT support materials reveals that the NO_x adsorption capability of the AZT ternary oxide is way larger than that of the ZT binary oxide. This direct comparison is based on the total integrated area under the N-related desorption channels (i.e. NO+NO_2+N_2+N_2O). The total NO_x adsorption capability of ternary oxide system was found to be 143 % greater than that of binary oxide system. These values obtained from TPD calculations are in perfect agreement with the FTIR data set presented in section 3.2.1.1. Moreover, residual N-related species or completion of nitrate decomposition can be followed by the surface spectra before (black spectra) and after (red spectra) TPD analysis as illustrated in the insets of Figure 35a and 35b. These insets clearly indicate that while all of the nitrate/nitrite species on ZT were completely removed, significant amount of N-related species was observed on AZT even after TPD analysis.

3.3.1.2 NO_x TPD on Pt-Functionalized Binary and Ternary Oxides

As we already stated in previous sections, presence of Pt has no influence on the adsorption geometries of nitrate/nitrite functional groups on binary and ternary mixed oxides. In this section, effect of Pt metals on relative NO_x adsorption capacity and nitrate/nitrate decomposition characteristics was investigated *via* TPD analysis complementary to the FTIR results.

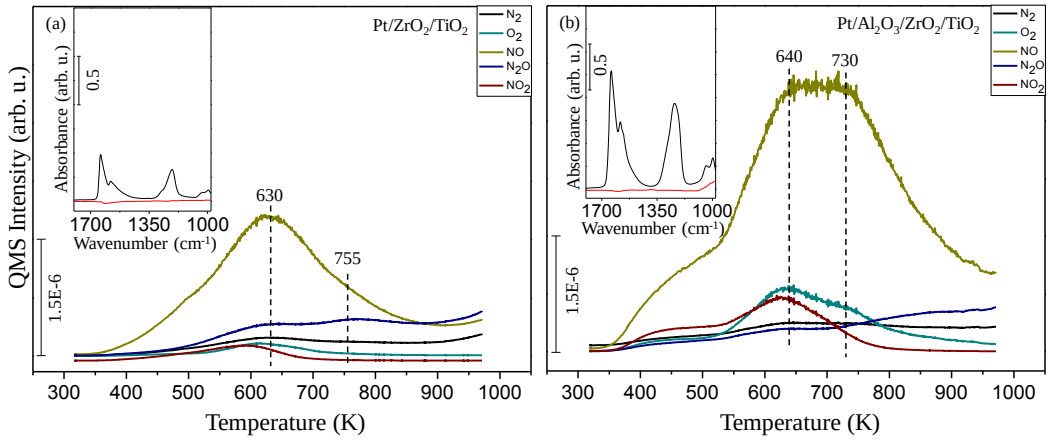

Figure 36: TPD profiles obtained from (a) Pt/ZT and (b) Pt/AZTsamples after saturation with 5 Torr NO_2(g) at 323 K for 10 min. The inset in each panel presents the FTIR spectra of the surfaces before (black) and after (red) TPD analysis. Copyright 2014 Elsevier B.V.[67].

Figure 36a and Figure 36b illustrates the nitrate/nitrite decomposition pathways obtained after NO_x saturation on both Pt/ZT and Pt/AZT at 323 K; respectively. As in the case of ZrO_2/TiO_2 (Figure 27a), NO desorption line of $Pt/ZrO_2/TiO_2$ has two temperature maxima at 630 and 755K as shown in Figure 36a. However, it is apparent that relative abundance of high temperature desorption feature at 755 K is significantly suppressed due to redox activity of platinum metal. Here, Pt sites facilitates the bond cleavage that favors the high temperature nitrate desorption temperature toward the lower states in $Pt/ZrO_2/TiO_2$.. Another influence

of the platinum is the change in relative intensities of the N_2 and N_2O desorption channels. Total integrated area under N_2 and N_2O features significantly increases upon Pt incorporation that can possibly be attributed to the Pt-catalyzed direct partial/total reduction of the adsorbed nitrates on the $Pt/ZrO_2/TiO_2$ sample. Lack of a significant O_2 desorption signal at 755 K indicates that the oxidizing species such as atomic oxygen or diatomic oxygen generated during the partial/total reduction of nitrates are possibly captured by the Pt/ZT system where they may oxidize Pt sites and/or titrate oxygen defects in the tetragonal ZrO_2 or $ZrTiO_4$ phases. On the other hand, Pt incorporation to ZrO_2/TiO_2 system significantly enhances NO_x adsorption capacity. While integrated area under NO desorption signal increases by about 32 %, total integrated NO_x adsorption capability associated with $NO+NO_2+N_2+N_2O$ desorption channels increases by about 100 %. However, it should be noted that these values do not represent the real NO_x Storage Capacity (NSC) and can only be evaluated as semi-quantitative comparison of investigated materials.

Identical set of TPD experiments were also carried out for Pt/AZT catalyst as shown in Figure 36b. This investigation clearly states that thermal decomposition of nitrate/nitrite species exhibited different desorption characteristics where incorporation of Pt metals significantly promote much lower temperature maxima (640 and 730 K, Figure 36b) for nitrate decomposition. While nitrate/nitrite decomposition at 640K takes place in the form of NO, O_2, and NO_2, anotherNO_x desorption state at 730K occurs *via* evolution of NO and O_2 only. Moreover, Pt/AZT material revealed identical NO (*m/z*=30) desorption temperature maxima as compared to those of ZT and Pt/ZT. These similarities can possibly be correlated by the redox capability of platinum metals that oxidizes the AZT surface during the calcination step leading to the formation of finely dispersed and ordered structures of

tetragonal-ZrO_2, TiO_2, $ZrTiO_4$ and Al_2O_3 which is elusive to detect *via* bulk characterization techniques such as XRD.

Since nitrate/nitrite decomposition is not complete within the temperature window of TPD analysis for AZT material, it is difficult to compare relative NO_x adsorption capabilities in between AZT and Pt/AZT. In any case, Pt incorporation to the AZT system drastically increase integrated total NO (m/z=30) signal by about 288 %, total integrated area under the N-related signals associated with $NO+NO_2+N_2+N_2O$ increases by about 50 % as well.

Furthermore, relative NO_x adsorption quantities of each material should be also evaluated by taking their specific surface area into account rather than active adsorption/storage sites. These calculations revealed that presence of the platinum in binary oxide system enhances the total integrated NO_x-adsorption/m^2 by about 41 %. However, Pt incorporation to the ternary oxide system plays much more significant role that boosts the NO_x-adsorption/m^2 by about 109 %.

Corresponding FTIR data presented as inset in Figure 36a and Figure 36b indicates the surface N-related functional groups before (black spectrum) and after (red spectrum) TPD analysis (i.e. after annealing at 973 K). We can correspondingly deduce the complete desorption for both materials as indicated in the insets in Figure 36. Here, one can readily refer to Figure 34b in order to interpret the role of Pt on the thermal stabilities of surface nitrate/nitrite groups on ternary oxide system.

3.3.1.3 NO_x TPD on Pt-functionalized Binary and Ternary Oxides with Basic Oxides

Prior to TPD experiments, materials were saturated by 5.0 Torr NO_2(g) for 10 min at 323 K, followed by vacuum annealing up to 973 K. Figure 37a-d illustrates the TPD profiles obtained after NO_2(g) adsorption over Pt/AZT, Pt/8BaO/AZT, Pt/20BaO/AZT and Pt/20BaO/Al materials; respectively. Thermal decomposition of adsorbed nitrate species on Pt/AZT and Pt/8BaO/AZT exhibits relatively similar characteristics as shown in Figure 37a and Figure 37b; respectively. It is clear that NO desorption signal (*m/z*=30) revealed two main desorption maxima at 645 and 740 K. While nitrate decomposition produces desorption channels of NO (*m/z*=30), NO_2 (*m/z*=46) and O_2 (*m/z*=32) at low temperature state (i.e. 645 K), major desorption features are primarily NO (*m/z*=30) and O_2 (*m/z*=32) for high temperature state (i.e. 740 K) with a relatively insignificant contribution from other desorption channels. Identical TPD experiments were also performed for the catalysts with higher BaO loadings (i.e. wt. % 20 BaO). Thermal decomposition of nitrate species on Pt/20BaO/AZT and Pt/20BaO/Al_2O_3 material surfaces are illustrated in Figure 37c and 37d; respectively. As compared to previous TPD results for Pt/AZT and Pt/8BaO/AZT, Figure 37c and Figure 37d obviously indicate that desorption channels related to NO (*m/z*=30) and O_2 (*m/z*=32) at the high temperature state (*i.e.* 750 K) are more pronounced with much higher QMS intensity.

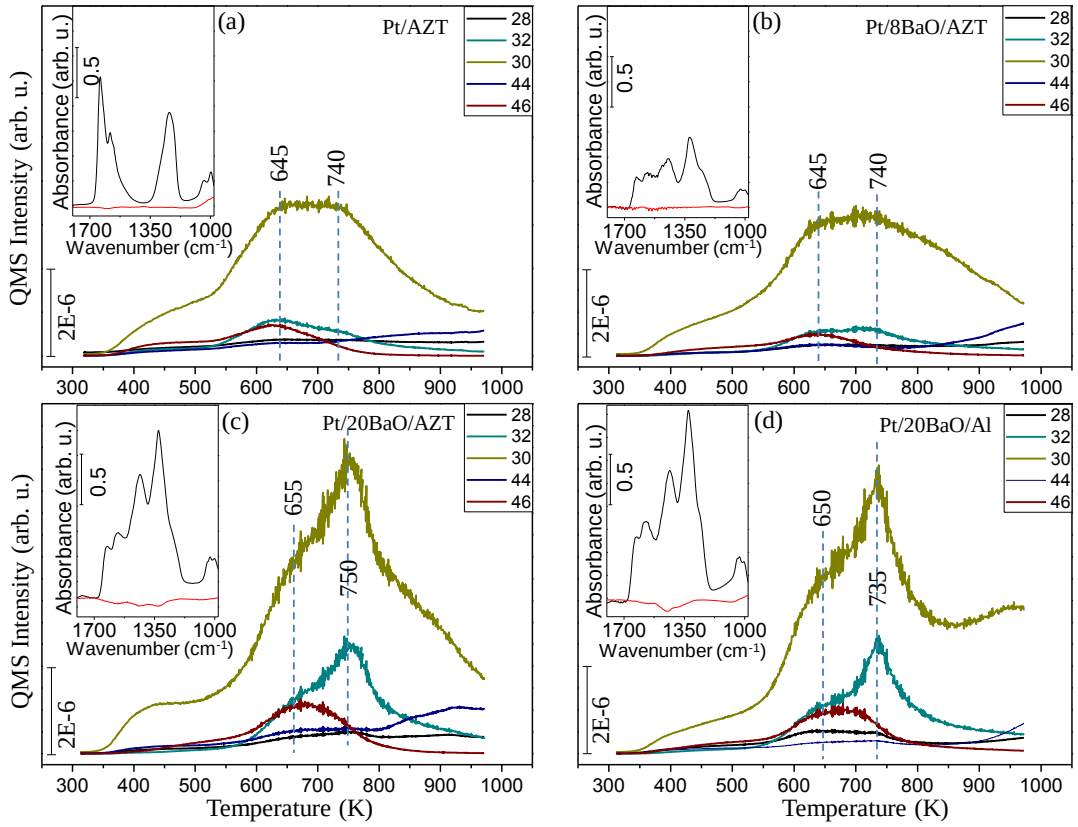

Figure 37: TPD profiles obtained from (a) Pt/AZT, (b) Pt/8BaO/AZT, (c) Pt/20BaO/AZT and (d) Pt/20BaO/Al_2O_3 samples after saturation with 5 Torr NO_2(g) at 323 K for 10 min. The inset in each panel shows the FTIR spectra of the surfaces before (black) and after (red) TPD analysis.

These findings lead us to obtain fundamental knowledge related to nitrate decomposition mechanisms on BaO-containing materials in the absence of external reducing agent which are summarized *via* following pathways:

$$Ba(NO_3)_2 \Leftrightarrow BaO + NO + NO_2 + O_2 \ (645\ K) \qquad 3.12$$

$$Ba(NO_3)_2 \Leftrightarrow BaO + 2NO + 3/2O_2 \ (740\ K) \qquad 3.13$$

Ozensoy *et al.* [121] also investigated nitrate decomposition on $BaO/Al_2O_3/NiAl(100)$ model catalyst indicating two major desorption states at 620 and 794 K, which are relatively close to our results on high surface area powder catalyst.

In addition to the mechanistic information obtained *via* TPD results, one can also readily gather more quantitative knowledge regarding the relative NO_x adsorption capability by integrating each of the N-related desorption channels (i.e $NO + NO_2 + N_2 + N_2O$) as previously mentioned in one of our most recent studies [67]. However, we should make sure that whole adsorbed NO_x species are completely desorbed from investigated surfaces at the end of TPD analysis in order to make reasonable calculations. FTIR data corresponding to surfaces before and after TPD experiments were illustrated as insets in Figure 37. These FTIR data set clearly emphasize that materials are completely regenerated after TPD (i.e. annealing under vacuum at 973 K).

Figure 38 shows the results based on the total integrated signals under TPD curves presented in Figure 37a-37d and their SSA normalized values. These values were obtained using fragmentation factors of our own QMS as stated in the previous section.

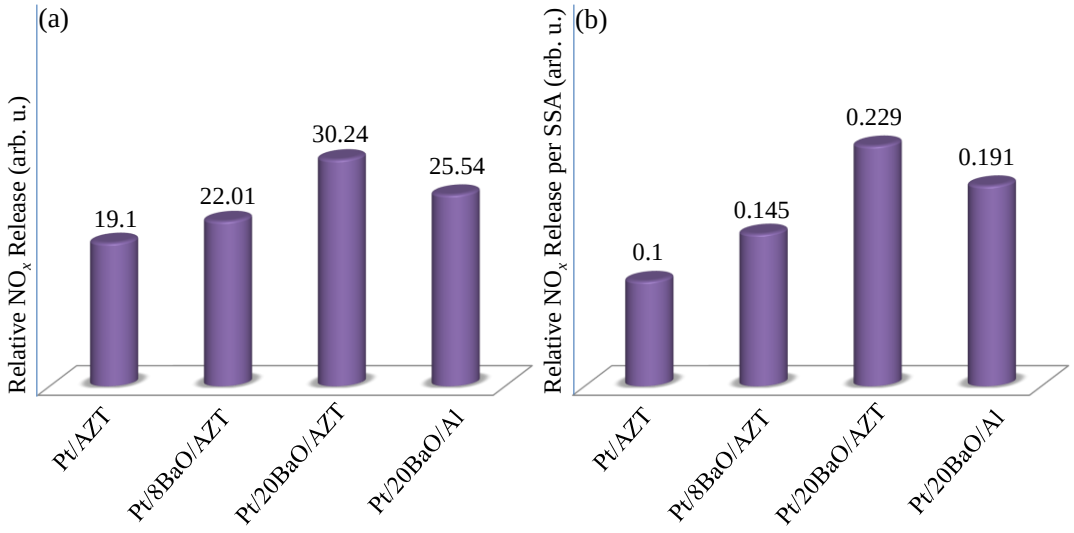

Figure 38: (a) Integrated NO_x TPD desorption signals and (b) corresponding SSA-normalized values.

Calculated numbers clearly suggest that NO_x adsorption capability of Pt/AZT is slightly affected by the addition of wt. 8 % BaO. However, higher BaO loading (*i.e.* 20 wt. %) onto Pt/AZT leads to a drastic change where total integrated area increased by about 58 %. Moreover, it was found that NO_x adsorption performance of Pt/20BaO/AZT is 19 % higher than that of benchmark NSR Pt/20BaO/Al_2O_3.

Moreover, calculated NO_x adsorption quantities should also be assessed by considering their specific surface areas (SSA). Depending on SSA normalized values, NO_x adsorption capability at 323 K can be ranked as Pt/20BaO/AZT > Pt/20BaO/Al_2O_3 > Pt/8BaO/AZT> Pt/AZT. Here, it should be mentioned once again that since these values were derived at 323 K in a batch-type reactor together with the use of NO_2(g) only, they cannot directly be correlated by the realistic NO_x storage capacities (NSC) of investigated materials.

Another series of analysis regarding K_2O-based materials were also conducted under identical experimental conditions in order to gather semi-quantitative knowledge regarding the relative NO_x-adsorption capabilities of investigated materials. Figure 39a-39d illustrates characteristics of NO_x-TPD profiles of synthesized materials with different K_2O loadings. Thermal decomposition of adsorbed nitrate/nitrite groups exhibits similar behavior for Pt/AZT and Pt/2.7K_2O/AZT as shown in Figure 39a and Figure 39b; respectively. Similar to the Pt/AZT, nitrate/nitrite decomposition from Pt/2.7K_2O/AZT yielded two main NO (*m/z*=30) desorption maxima at 645 and 715 K, having almost identical QMS intensities as shown in Figure 39b. While nitrate decomposition produces desorption channels of NO (*m/z*=30), NO_2 (*m/z*=46) and O_2 (*m/z*=32) at low temperature state (LT=645 K), major desorption features are primarily NO (*m/z*=30) and O_2 (*m/z*=32) for high temperature state (HT=715 K) with a relatively negligible contribution from other desorption channels. That is, Pt/AZT and Pt/2.7K_2O/AZT exhibit identical surface characteristics that can be expressed by the well dispersed and 2-D K_2O domains over AZT support, yielding the formation of surface like nitrate species rather than bulk like nitrates as already stated by the FTIR-NO_x adsorption experiments. In this particular loading, both K_2O domains and AZT support sites have concomitantly exposed to NO_x adsorption. On the other hand, materials with higher K_2O loading, Pt/5.4K_2O/AZT and Pt/10K_2O/AZT, were also investigated under identical conditions as illustrated in Figure 39c and Figure 39d; respectively.

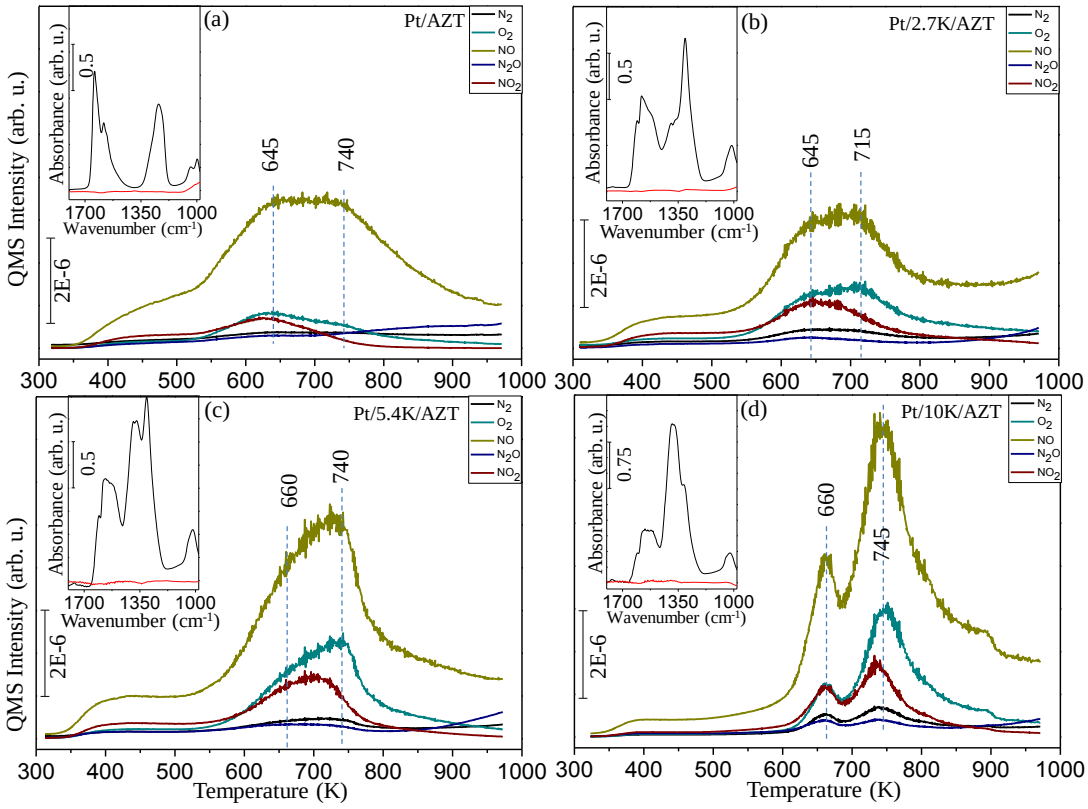

Figure 39: TPD profiles obtained from (a) Pt/AZT, (b) Pt/2.7K_2O/AZT, (c) Pt/5.4K_2O/AZT and (d) Pt/10K_2O/AZTsamples after saturation with 5 Torr NO_2(g) at 323 K for 10 min. The inset in each panel shows the FTIR spectra of the surfaces before (black) and after (red) TPD analysis.

As compared to previous TPD results for Pt/2.7K_2O/AZT catalyst, nitrate/nitrite decomposition from Pt/5.4K_2O/AZT catalyst clearly point out that desorption features associated with NO (*m/z*=30) and O_2 (*m/z*=32) at high temperature state (*i.e.* 715 K) were more pronounced together with the higher QMS intensity. Moreover, it should be noted that NO_2 (*m/z*=46) desorption feature shifted towards high temperatures. Further increase in K_2O loading revealed significantly different desorption pathways for Pt/10K_2O/AZT where low and high temperature desorption states are highly discernible at 660 and 745 K; respectively as shown in Figure 39d.

These series of results are in very good agreement with the FTIR adsorption experiments suggesting the formation of 3-D K_2O islands over AZT support and generation of bulk/ionic nitrates with increasing K_2O loading. Overall nitrate pathway on K_2O-containing materials can be envisioned as follows:

$$2KNO_3 \Leftrightarrow K_2O + NO + NO_2 + O_2 \text{ (740 K)} \qquad 3.14$$

One can readily gather quantitative knowledge regarding the relative NO_x adsorption capabilitiey by integrating N-related desorption channels (i.e $NO + NO_2 + N_2 + N_2O$) as mentioned in previous sections as well as in one of our recent studies [67]. We should however make sure that all of the adsorbed NO_x species are completely removed from the investigated surfaces at the end of TPD analysis in order to make accurate calculations. FTIR data corresponding to surfaces before and after TPD experiments were illustrated as insets in Figure 38. These FTIR data clearly emphasize that materials were completely regenerated after TPD (i.e. annealing under vacuum at 973 K). Figure 40 shows the integrated values under TPD curves presented in Figure 37d and 39a-39d and their SSA normalized values. These values are generated *via* specific series of equations described in the previous section.

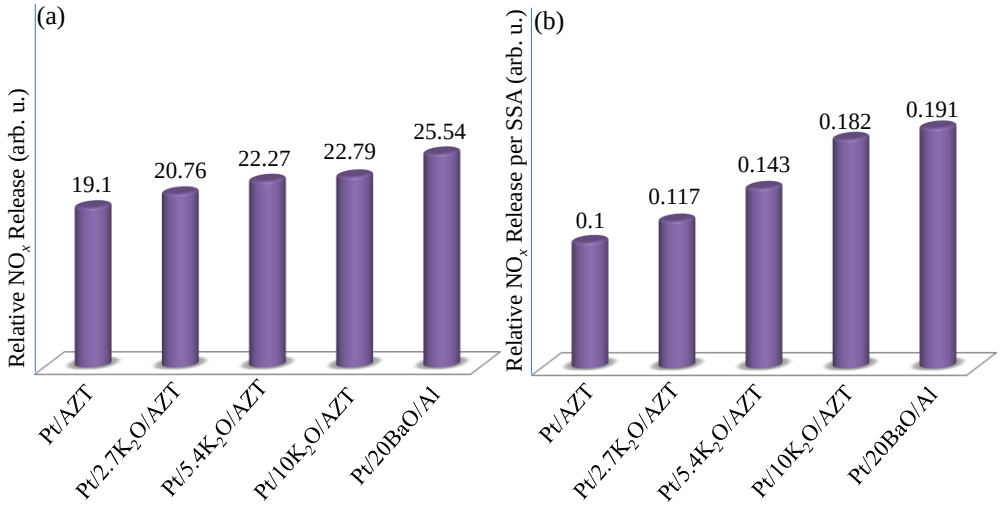

Figure 40: (a) Integrated values regarding relative NO_x adsorption capabilities derived from TPD analysis and (b) their SSA normalized values.

As can be seen in Figure 40, relative NO_x storage amounts of the AZT-based catalysts increase monotonically with increasing K_2O loading until 5.4 wt. % K_2O, after which it converges to a value that is comparable to that of the Pt/20BaO/Al benchmark catalyst. Moreover, calculated NO_x adsorption quantities should be also assessed by considering their specific surface areas (SSA). Depending on SSA normalized values, NO_x adsorption capability at 323K can be ranked as $Pt/20BaO/Al_2O_3$ > $Pt/10K_2O/AZT$> $Pt/5.4K_2O/AZT$> $Pt/2.7K_2O/AZT$> Pt/AZT.

3.3.2 SO_x Adsorption and Desorption Properties*via* TPD

3.3.2.1 SO_x TPD on Pt-functionalized Binary and Ternary Oxides

TPD experiments were carried out in vacuum in order to investigate the thermal regeneration ability of the synthesized catalysts after sulfur poisoning, as well as to compare the relative adsorption strengths of SO_x species residing on the poisoned catalyst surfaces. Prior to TPD experiments, each catalyst was exposed to 2.0 Torr SO_2+O_2 gas mixture (SO_2:O_2 = 1:10) at 673 K for 30 min.

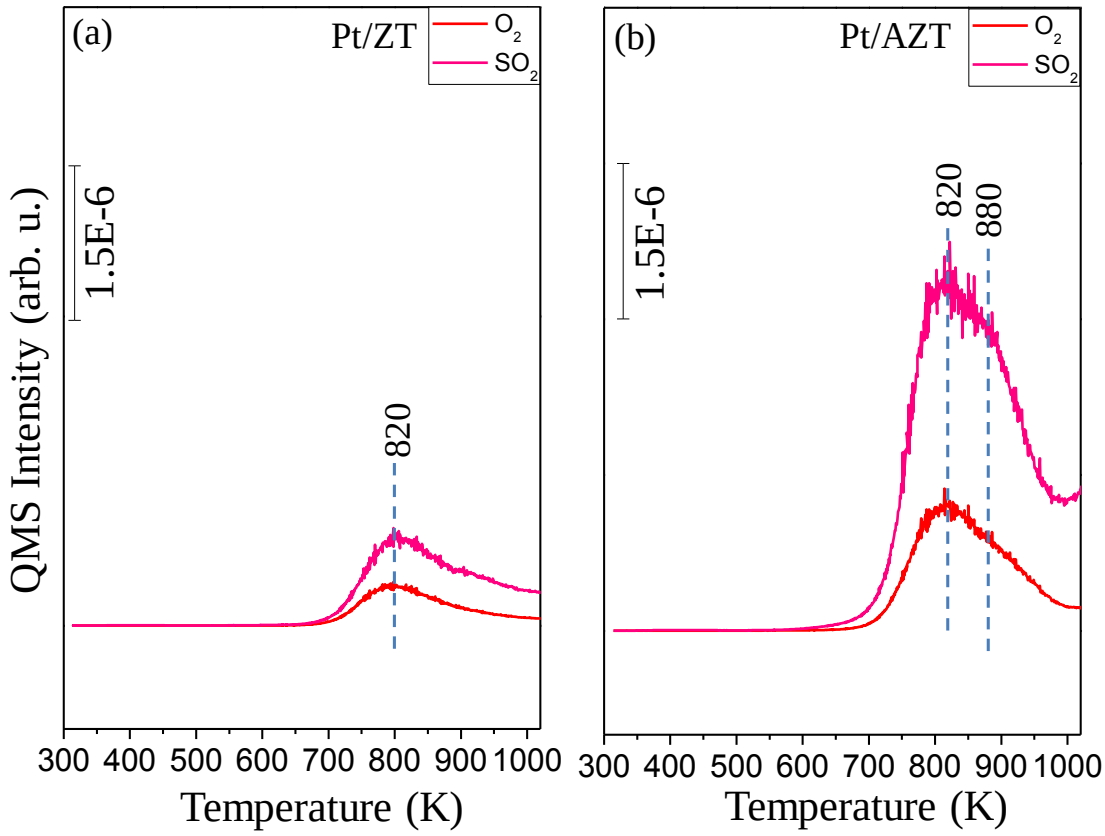

Figure 41: TPD profiles for (a) Pt/ZT and (b) Pt/AZT after 2.0 Torr SO_x (2.0 Torr SO_2+O_2, SO_2:O_2 = 1:10) adsorption at 673 K for 30 min.

Figure 41a and 41b demonstrates the TPD analysis of SO_x-poisoned Pt/ZT and Pt/AZT materials; respectively. These set of experiments reveal major decomposition products of sulfate/sulfite groups upon thermal annealing under vacuum in the temperature range of 323-1050 K (*i.e.* the highest experimentally attainable temperature in the current TPD setup). Figure 41 illustrates that decomposition of S-related species exhibits two major TPD desorption channels namely, m/z =32 and 64 corresponding to O_2 and SO_2 desorption; respectively.

In Figure 41, adsorbed SO_x species on each Pt-supported binary and ternary oxide systems are highly stable so that no desorption signals were detected until 700 K. Beyond this temperature, sulfate/sulfite groups on each catalyst started to decompose by generating major features of O_2 and SO_2 within a relatively similar temperature range (*i.e.* 800-900 K). Moreover, it is worth mentioning that generation of another major reduction product of H_2S is elusive to detect due to lack of external reducing H_2(g).

On the other hand, we can also conclude that Pt/AZT material revealed much higher QMS intensity, indicating the relatively higher sulfur uptake as compared to that of Pt/ZT which might be correlated to much higher SSA of the former material. As already emphasized throughout previous sections, despite the promising sulfur regeneration performance of BaO-free and K_2O-free materials, these materials should be further functionalized to have a delicate balance between NO_x storage capacity and sulfur regeneration performance. In the forthcoming section, relative sulfur adsorption and decomposition characteristics of BaO or K_2O-containing NSR/LNT materials will be investigated.

3.3.2.2 SO_x TPD on Pt-functionalized Ternary Oxides Containing Basic Storage Domains

Figures 42a-42d illustrate the TPD profiles corresponding to pre-sulfated Pt/AZT, Pt/8BaO/AZT, Pt/20BaO/AZT and Pt/20BaO/Al catalysts; respectively. Each panel in Figure 41 shows two major TPD desorption channels namely, m/z =32 and 64 corresponding to O_2 and SO_2 desorption; respectively. It is worth mentioning that no other desorption species such as H_2S were detectable in the TPD experiments. Figure 42 clearly shows that SO_x species adsorbed on all of the investigated catalysts have high thermal stability, evident by the lack of any SO_x desorption/decomposition signals below 700 K.

On the other hand, SO_x decomposition/desorption maxima in Figure 42 show noticeable variations as a function of catalyst composition indicating the dissimilarities in the relative thermal stabilities of SO_x species on different catalyst surfaces. For the Pt/AZT70 catalyst lacking BaO (Figure 42a), m/z =32 and 64 desorption channels reveal identical temperature maxima at 820 K. This indicates that the sulfate and sulfite species decompose and desorb from the Pt/AZT surface predominantly in the form of $SO_2(g) + O_2(g)$. Figure 42a suggests that the SO_x desorption is almost complete for the Pt/AZT sample within the thermal window of TPD analysis.

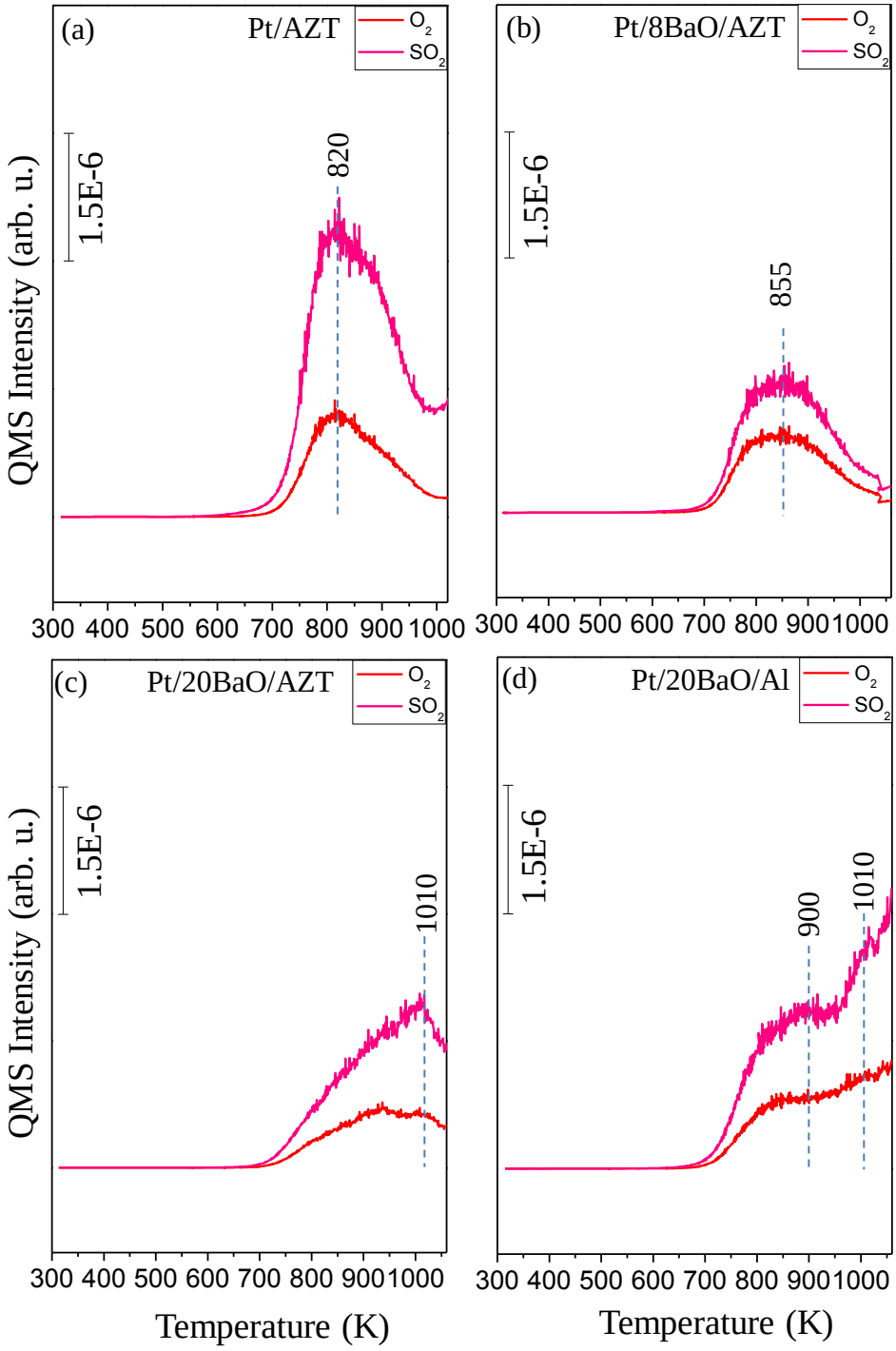

Figure 42: TPD profiles for (a) Pt/AZT, (b) Pt/8BaO/AZT, (c) Pt/20BaO/AZT and (d) Pt/20BaO/Al catalysts after 2.0 Torr SO_x (2.0 Torr SO_2+O_2, SO_2:O_2 = 1:10) adsorption at 673 K for 30 min.

In contrast, when the TPD data for Pt/AZT (Figure 42a) is compared with that of the conventional Pt/20BaO/Al benchmark catalyst (Figure 42d), it can readily be seen that, SO_x desorption maxima shift to significantly higher temperatures extending well beyond 1050 K (*i.e.* the highest experimentally attainable temperature in the current TPD setup) with incomplete desorption. This observation implies that the presence of basic BaO domains yields strong binding sites for SO_2, leading to the formation of thermally stable bulk like sulfate and sulfite species, unlike the relatively more acidic Pt/AZT surface exhibiting weaker adsorption sites for SO_x.

Figures 42b and Figure 42c corresponding to the TPD profiles of sulfur poisoned Pt/8BaO/AZT and Pt/20BaO/AZT catalysts suggest that by varying the BaO loading, one can fine-tune both the SO_x adsorption strength as well as the total amount of SO_x species adsorbed on the catalyst surfaces. Although the types of the desorbing species (*i.e.* $SO_2(g) + O_2(g)$) do not change upon BaO incorporation to the Pt/AZT structure; the desorption temperature maxima monotonically shift to higher temperatures with increasing BaO loading. It can also be realized that increasing BaO loading also increases the amount of SO_x adsorbed on the catalyst surfaces which is evident by the greater integrated TPD signals for Pt/20BaO/AZT (Figure 41c) with respect to that of Pt/8BaO/AZT (Figure 42b).

Comparison of the TPD results given in Figures 41 and Figure 42 indicates that SO_x desorption temperatures and the SO_x adsorption strength increases in the following order: Pt/ZT ~ Pt/AZT < Pt/8BaO/AZT < Pt/20BaO/AZT < Pt/20BaO/Al. Also, comparison of the BaO-containing samples reveals that the amount of adsorbed SO_x on the catalyst surfaces can be ranked as follows: Pt/8BaO/AZT < Pt/20BaO/AZT < Pt/20BaO/Al.

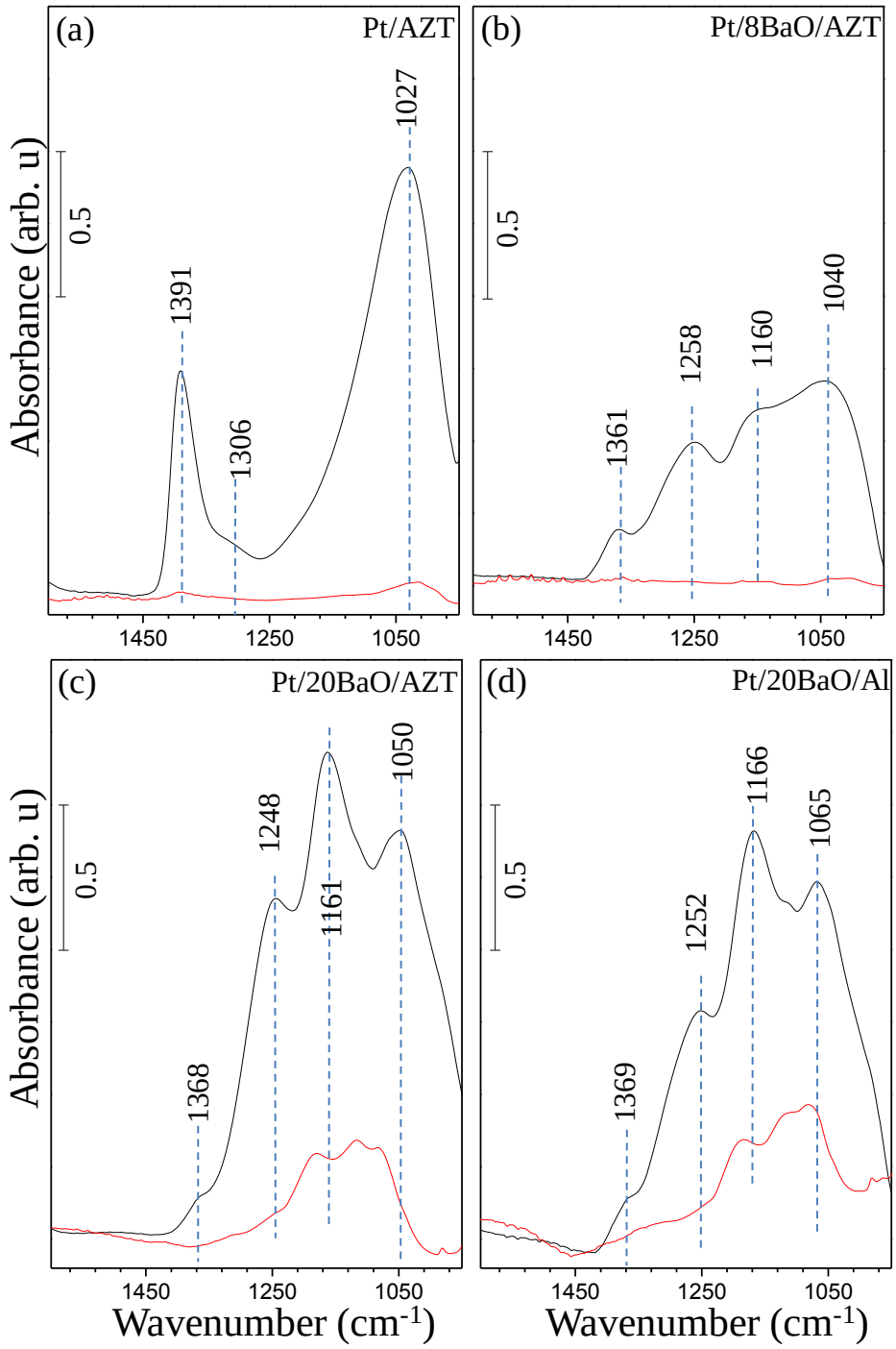

Figure 43: FTIR spectra corresponding to residual sulfur content on (a) Pt/AZT, (b) Pt/8BaO/AZT, (c) Pt/20BaO/AZT and (d) Pt/20BaO/Al catalysts before (black) and after (red) SO_x-TPD analysis.

Moreover, residual sulfur analysis of corresponding materials was also investigated by means of FTIR spectroscopy in order to have a better insight into sulfur regeneration performances. Figure 43 illustrates a set of FTIR spectra recorded before (black spectrum) and after (red spectrum) SO_x-TPD analysis of corresponding materials. While complete sulfur removal/regeneration was achieved for Pt/AZT (Figure 43a) and Pt/8BaO/AZT (Figure 43b), significant amount of sulfate/sulfite residues on Pt/20BaO/AZT (Figure 43c) and Pt/20BaO/Al (Figure 43d) were observed within the thermal window of TPD analysis.

Along the entire discussion, we comprehensively set forth the superior NSR activity of particular catalyst, Pt/8BaO/AZT, in terms of better NO_x storage capacity and excellent sulfur regeneration performance at different experimental conditions.

We also investigated the surface acid-base properties of synthesized catalysts by titrating their surface acidic sites (*i.e.*Brønsted and/or Lewis sites) with pyridine chemisorption monitored *via* in-situ FTIR spectroscopy as shown in Figure 44.

Pyridine adsorption at 298 K revealed six different vibrational features located at *c.a* 1610, 1589, 1574, 1540, 1485 and 1441 cm^{-1}. Along these vibrational bands, while 1610, 1485 and 1441 cm^{-1} can be attributed to C–C stretch of a coordinatively bonded pyridine complex indicating the presence of Lewis acid sites, 1540 cm^{-1} can be assigned for C–C stretching vibration of the pyridinium ion used for Brønsted acid sites [122]–[124]. It should also be kept in mind that feature located at 1485cm^{-1} can also be attributed to both Lewis and Brønsted acid sites, simultaneously [125]. On the other hand, two features located at 1589 and 1574 cm^{-1} can be tentatively assigned to weakly adsorbed pyridine bonded OH^- groups on support surface [126].

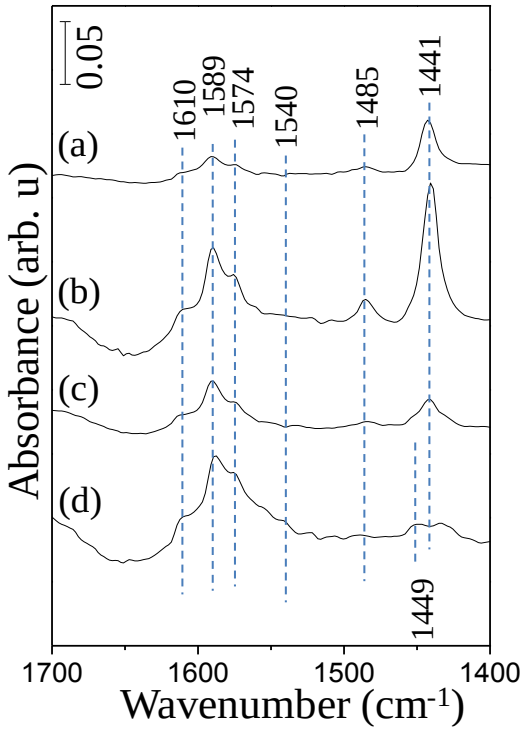

Figure 44: In-situ FTIR spectra corresponding to pyridine adsorption on (a) Pt/AZT, (b) Pt/8BaO/AZT, (c) Pt/20BaO/AZT and (d) Pt/20BaO/Al catalysts at 298 K.

In Figure 44a and 44b, incorporation of 8 wt. % BaO to Pt/AZT system causes a significant increase in the surface concentration of Lewis acid sites that can be correlated with the higher IR absorbance intensity of particular vibrational features. However, this trend did not proceed further for higher BaO loading (i.e. wt. 20 % BaO) to Pt/AZT where vibrational features were diminished due to blocking of the AZT surface. This decrease in IR intensities indicates that Pt/20BaO/AZT has a lesser number of Lewis acidic surface sites as compared to Pt/8BaO/AZT shown in Figure 44c. Furthermore, Pt/20BaO/Al benchmark catalyst exhibits almost identical surface acidity to Pt/20BaO/AZT except the presence of an additional weak shoulder at 1540 cm^{-1} assigned to Brønsted acid sites as illustrated in Figure 44d.

Depending on these findings, we can directly denote that each AZT-supported catalyst has substantial amount of Lewis acid sites rather than Brønsted sites and Pt/8BaO/AZT catalyst surface revealed the largest concentration of Lewis acidic sites among all other investigated materials. Along these lines, we can constitute a direct correlation in between superior sulfur regeneration performance of Pt/8BaO/AZT and the significant role of the concentration of Lewis acid sites.

In addition to the pyridine adsorption and in-*situ* FTIR spectroscopy, the acidic properties of the catalysts were investigated using ammonia as a probe molecule. After adsorption at 50^{o}C, physisorbed ammonia was released at low temperatures. TPD profiles of the samples are shown in Figure 45 and each TPD profile is characterized by weakly, medium and strongly bound ammonia to the catalytic surfaces.

The ammonia desorption peak with a maxima at around 400 K corresponds to AZT mixed oxides support, as well as to Al_2O_3, and it can be assigned to the ammonia desorption from the Lewis and/or Bronsted acid sites [127]–[129]. A clear difference between the AZT and Al_2O_3, is that the ammonia desorption from the AZT support is much broader with a shoulder at high temperature. These results clearly reveal the larger acidity for the AZT support. The incorporation of 8 wt. % Ba and 20 wt. % Ba; respectively, into the AZT support is evidenced by decreased ammonia storage at high temperature, especially for the high barium loaded sample. NH_3 desorption in terms of mmol/g_{cat} was also calculated and illustrated in Figure 46 for each material. These results are in a good agreement with the pyridine adsorption experiments in the former section.

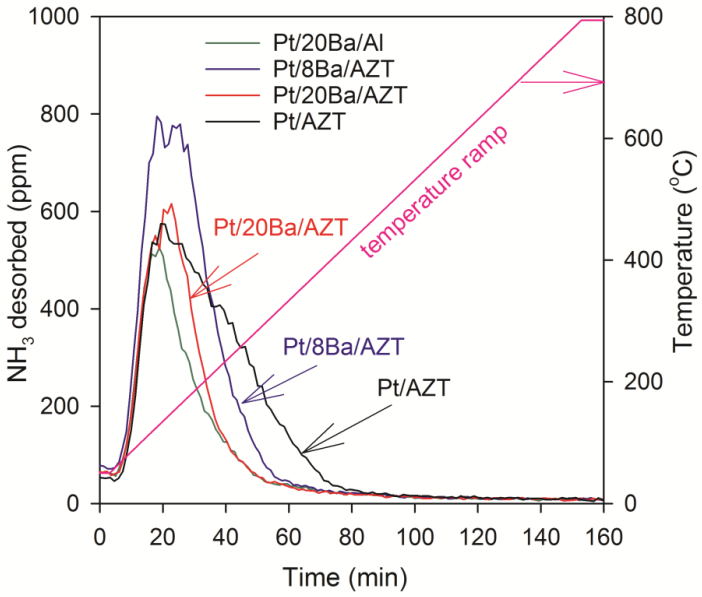

Figure 45: NH_3 TPD profiles of Pt/AZT, Pt/8BaO/AZT, Pt/20BaO/AZT and Pt/20BaO/Al catalysts. The samples were exposed to 2000 ppm NH_3 at 323 K for 8 h during adsorption. After the samples were treated with argon for 30 min, the temperature was increased to 1073 K in argon and the ammonia desorption occurs.

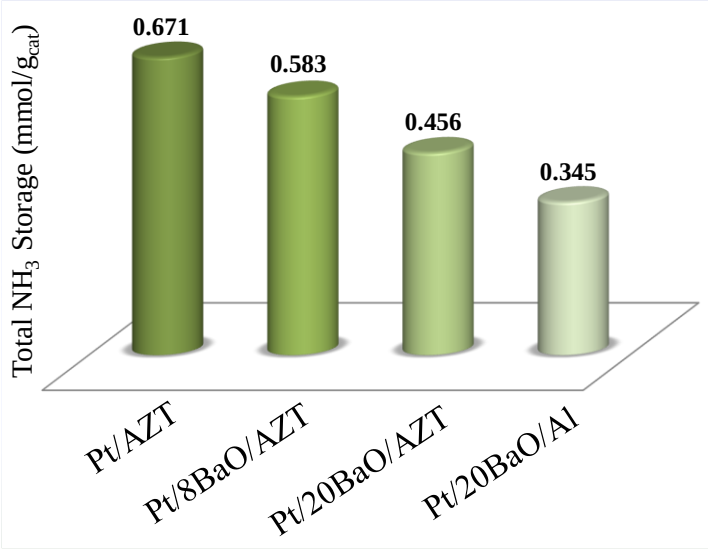

Figure 46: Integrated TPD signals obtained *via* NH_3-TPD experiments.

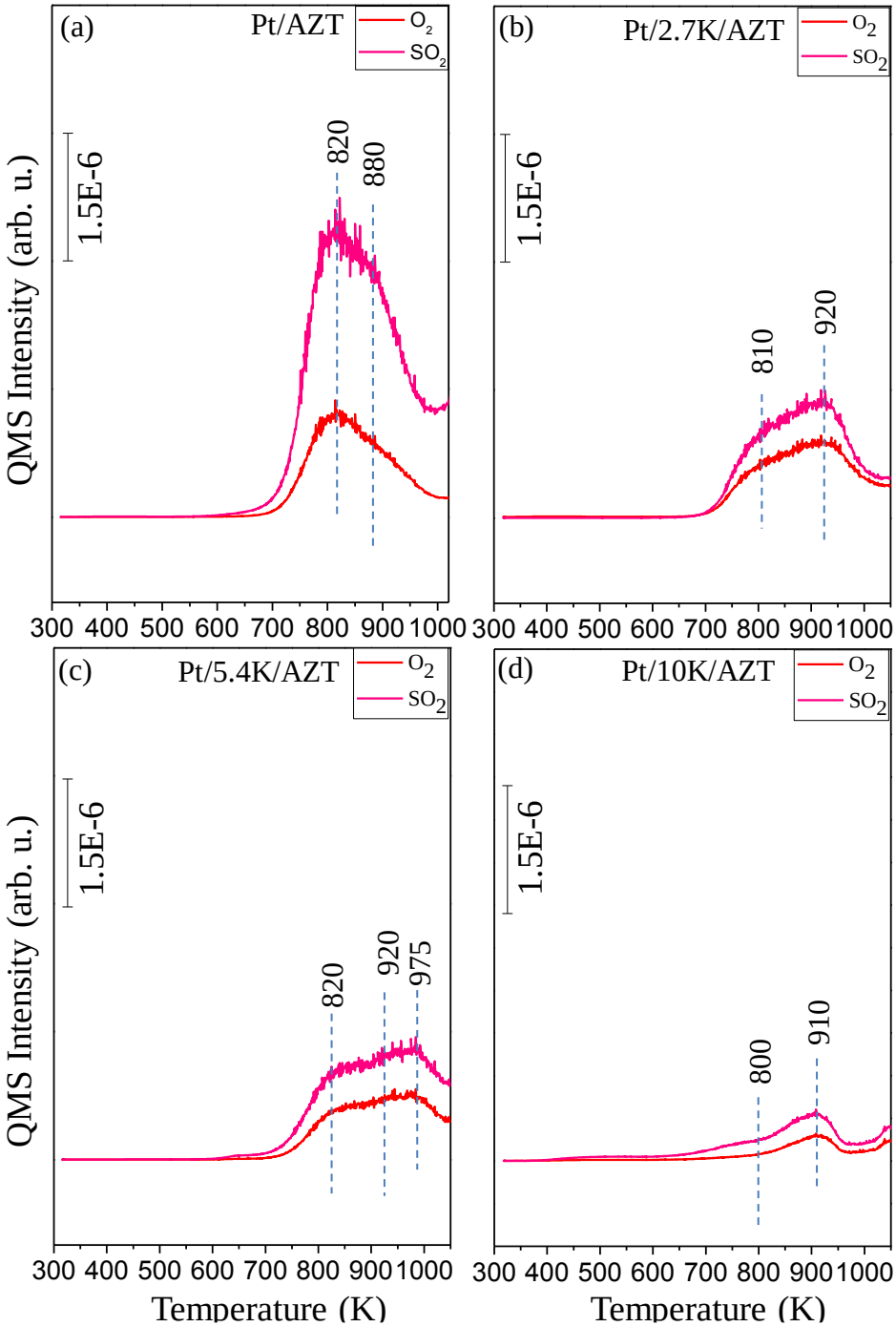

Figure 47: TPD profiles for (a) Pt/AZT, (b) Pt/2.7K_2O/AZT, (c) Pt/5.4K_2O/AZT and (d) Pt/10K_2O/AZT catalysts after 2.0 Torr SO_x (2.0 Torr SO_2+O_2, SO_2:O_2 = 1:10) adsorption at 673 K for 30 min.

Identical set of TPD experiments were also performed for K_2O-based materials in order to investigate the effect of K_2O loading on thermal stability of sulfate/sulfite groups. Figures 47a-47d demonstrates the desorbing species as a result of thermal decomposition of sulfates and sulfites from Pt/AZT, Pt/2.7K_2O/AZT, Pt/5.4K_2O/AZT and Pt/10K_2O/AZT catalysts; respectively.

Figure 47shows the TPD spectra corresponding to the thermal decomposition of sulfates and sulfites on Pt/AZT, Pt/2.7K_2O/AZT, Pt/5.4K_2O/AZT and Pt/10K_2O/AZT catalyst surfaces. In these TPD experiments, only O_2 and SO_2 desorption channels (corresponding to mass to charge ratios of *m/z* =32 and 64; respectively) revealed significant signals and other SO_x or H_2S species were not detectable. As in the case of the BaO-based conventional NSR/LNT catalyst (Figure 42d), SO_x-related species adsorbed on Pt/AZT and its K_2O-incorporated counterparts reveal high thermal stability which is evident by the appearance of SO_x desorption signals at T > 700 K.

Analysis of the general TPD line shapes given in Figures 47a-47c suggests that at least two different SO_x desorption signals exist for Pt/AZT, Pt/2.7K_2O/AZT and Pt/5.4K_2O/AZT catalysts at T <1050 K, revealing desorption maxima located at *ca*. 800-820 K and at 900-975 K. Furthermore, SO_2 desorption on these surfaces within 700-1050 K is accompanied by O_2 desorption, suggesting that sulfate/sulfite decomposition occurs in the form of simultaneous SO_2 + O_2 release. It should be noted that the contribution of the SO_2 gas to the m/z=32 signal due to electron-impact induced fragmentation of SO_2 in the QMS ionizer chamber is less than 10 %, suggesting that m/z=32 signal can be almost exclusively attributed to the evolution of O_2(g) from the catalyst surfaces.

It is visible in Figures 47a-47c that the TPD desorption maxima tend to shift towards higher temperatures with increasing K_2O loading in the catalyst formulation. It can also be noticed that with increasing K_2O loading to 5.4 wt. % (see Figure 47c), relative intensity of the 820 K desorption feature which can be mostly associated with SO_x species on AZT surface is suppressed, along with the generation of a high-temperature desorption shoulder at 975 K. This is in perfect agreement with the *in-situ* FTIR results presented in Figure 30 suggesting that with increasing K_2O surface coverage, extent of exposed (uncovered) AZT surface decreases along with an increase in the K_2O particle size, facilitating the formation of bulk-like sulfates that are also thermally more stable than that of the sulfates on AZT.

It is also important to note that the SO_x desorption is not complete in Figures 47b-47d even at 1050 K (*i.e.* the highest experimentally attainable temperature in the current TPD setup) as evident by the presence of a desorption tail at T = 1050 K which is presumably extending well-beyond this temperature (as supported by the *in-situ* FTIR results that will be provided later in the text). This observation implies that while surface sulfates/sulfites present on AZT support and K_2O domains fully decompose at temperatures below 920 K, bulk-like potassium sulfate species require higher desorption temperatures for complete thermal decomposition and desorption. In other words, presence of basic K_2O domains yields strong binding sites for SO_2, leading to the formation of thermally stable surface and bulk-like SO_x species.

On the other hand, a further increase in the K_2O loading to 10 wt. % illustrates rather different SO_x desorption characteristics (Figure 47d). It is evident that the SO_x desorption features at T < 1050 K are suppressed to a great extent, leading to a relatively minor desorption feature located at 910 K with a shoulder at

ca. 810 K. Considering the significant SO_x uptake of the Pt/10K_2O/AZT catalyst surface demonstrated by the *in-situ* FTIR data given in Figure 30d, it is clear that most of the sulfate/sulfite species on Pt/10K_2O/AZT remain intact even after vacuum annealing up to 1050 K. From quantitative point of view, comparing the integrated desorption signals regarding TPD curves given in Figures 47 indicates that the amount of adsorbed SO_x on the catalyst surfaces can be ranked as follows: Pt/2.7K_2O/AZT< Pt/5.4K_2O/AZT< Pt/10K_2O/AZT.

Identical residual sulfur analysis of corresponding materials was also investigated by means of FTIR spectroscopy in order to have much clear insight into sulfur regeneration performances. Figure 48 illustrates a set of FTIR spectra recorded before (black spectrum) and after (red spectrum) SO_x-TPD analysis of corresponding materials. While complete sulfur removal/regeneration was achieved for Pt/AZT (Figure 48a) as already shown previously, significant amount of SO_x species corresponding to bulk like sulfate/sulfite residues on Pt/2.7K_2O/AZT were observed after TPD analysis as shown in Figure 48b.

Moreover, further increase in K_2O loading causes an increase in residual sulfur content on materials surfaces within the thermal window of TPD analysis. These comprehensive results regarding K_2O-based materials allow us to conclude that materials having K_2O loading more than 5.4 wt. % cannot be used as an alternative LNT/NSR catalyst due to its poor resistance towards sulfur poisoning although it can reveal significant NSC.

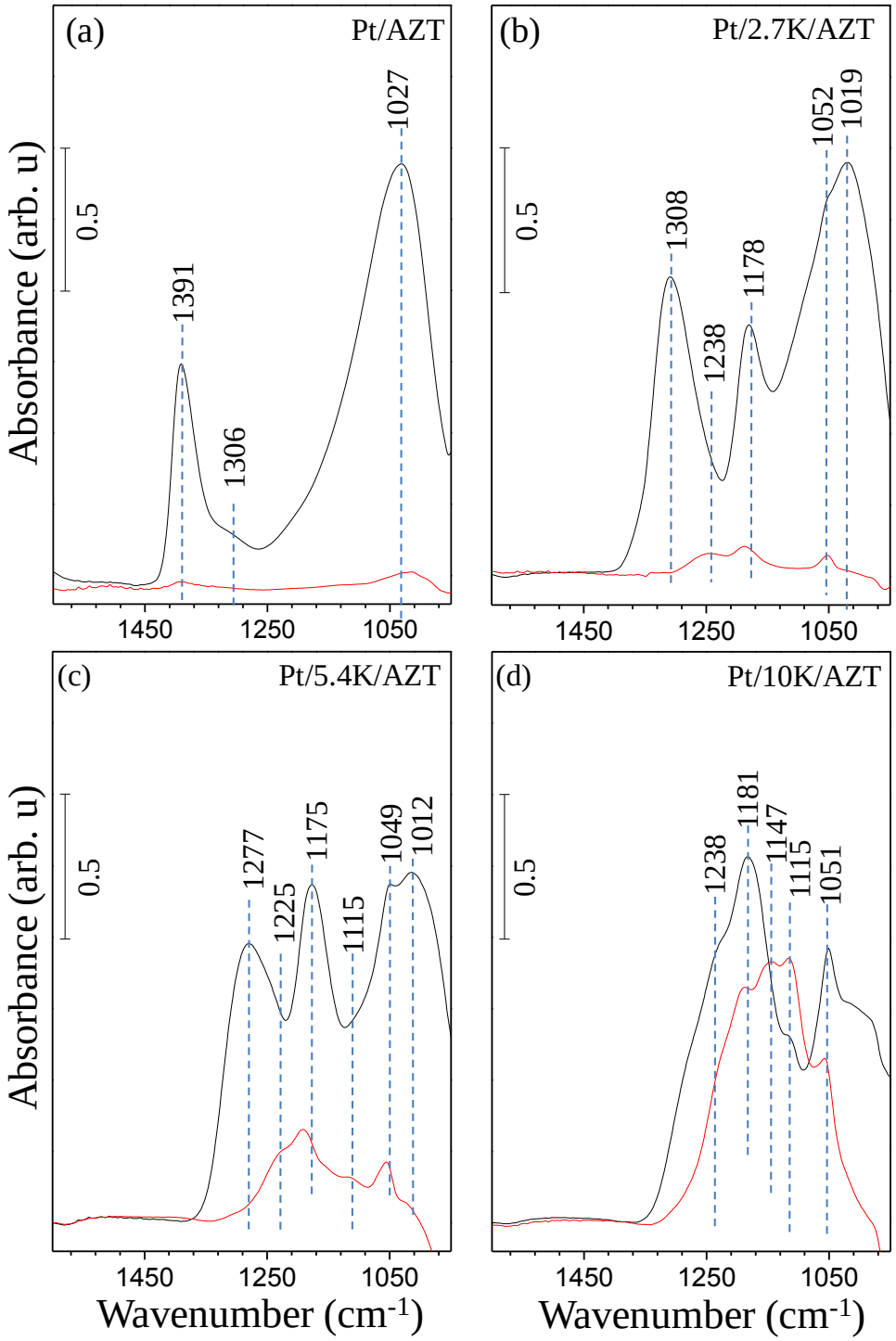

Figure 48: FTIR spectra corresponding to residual sulfur content on (a) Pt/AZT, (b) Pt/2.7K_2O/AZT, (c) Pt/5.4K_2O/AZT and (d) Pt/10K_2O/AZT catalysts before (black) and after (red) SO_x-TPD analysis.

Chapter 4

Flow Reactor Measurements

4.1 NO_x Storage Capacity of BaO-based NSR/LNT Catalysts

NO_x storage and reduction (NSR) performances of all materials were tested *via* monitoring the outlet NO_x concentrations in the course of seven lean/rich cycles.

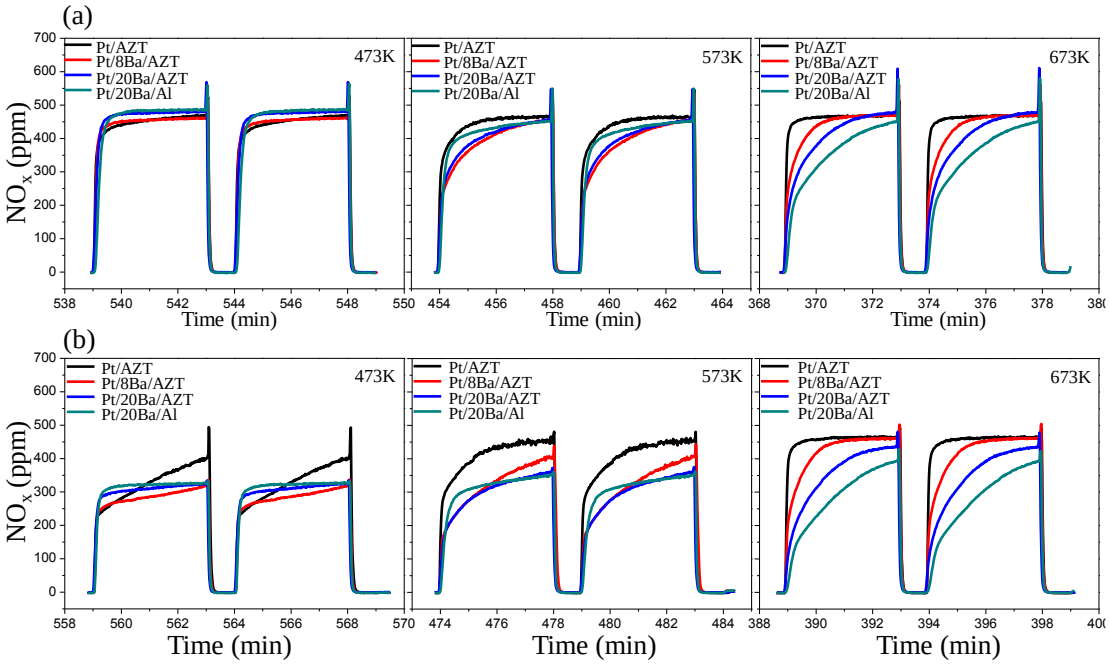

Figure 49: NO_x concentration profiles during last two lean/rich cycles over synthesized Pt-based catalysts. The samples were exposed to lean mixture of either (a) NO, CO_2, O_2 and H_2O or (b) NO_2, CO_2, O_2 and H_2O at different temperatures of 473, 573 and 673K. The experimental details are described in the experimental section.

Initially, all of the storage sites are available for NO_x capture over fresh (degreened) catalysts and therefore inlet NO (g) concentration was initially monitored as '0 ppm'. As the catalysts gradually saturate, NO (g) starts to slip over the catalysts. The increase in NO concentration finally reaches to a plateau due to the complete NO_x saturation. Then, the gas flow is switched from lean to rich regime and NO_x saturated catalyst is regenerated and adsorbed NO_x species are removed under reducing environment. NO_x analyzer starts to monitor '0 ppm' again throughout the 1 min rich regime followed by an increase in NO concentration. Figure 49 illustrates the last two lean/rich cycles regarding the wash-coated monolithic samples of Pt/AZT, Pt/8BaO/AZT, Pt/20BaO/AZT and Pt/20BaO/Al_2O_3 in two different feed gas mixtures in the temperature range of 473–673 K. While the first feed mixture (FM^1) was composed of (a) NO, O_2, CO_2, H_2O, Ar, second feed mixture (FM^2) included (b) NO_2, O_2, CO_2, H_2O, Ar.

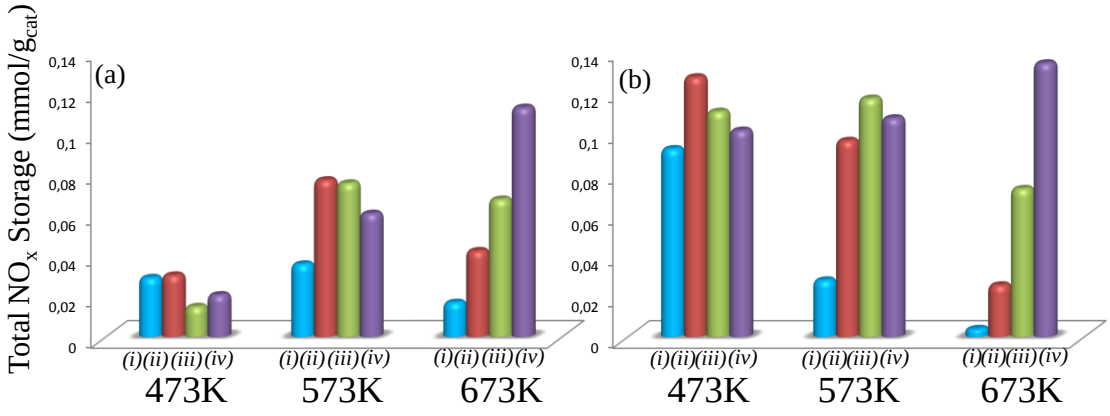

Figure 50: Total amount of NO_x stored on fresh (i) Pt/AZT, (ii) Pt/8BaO/AZT, (iii) Pt/20BaO/AZT and (iv) Pt/20BaO/Al_2O_3 catalysts obtained under lean mixture of either (a) NO, CO_2, O_2 and H_2O or (b) NO_2, CO_2, O_2 and H_2O at different temperatures of 473, 573 and 673K.

Moreover, results represented in Figure 50a and 50b correspond to total NO_x storage capacity in terms of mmol/g_{cat} in the lean gas mixture of either FM^1 or FM^2 at 473, 573 and 673 K.Although the quantities are fairly low for FM^1, Pt/AZT and Pt/8BaO/AZT material has a higher NO_x storage capacity at low temperatures (*i.e.* 473 K) as compared to that of Pt/20BaO/AZT and benchmark NSR Pt/20BaO/Al_2O_3 materials as shown in Figure 50a. However, NO_x storage capacities of all of the AZT catalysts were observed to be much larger due to better extent of NO oxidation capability at mild temperatures (*i.e.* 573 K). At this m ild conditions, Pt/8BaO/AZT and Pt/20BaO/AZT materials reveal superior performance against conventional Pt/20BaO/Al_2O_3 benchmark catalyst. Total NO_x storage quantities of Pt/8BaO/AZT and Pt/20BaO/AZT catalysts are 27 % and 24 % higher as compared to that of conventional Pt/20BaO/Al_2O_3; respectively. Pt/AZT catalyst demonstrated the lowest NO_x storage capacity at 573 K due to lack of basic BaO storage domains together with highly acidic surface hindering extent of adsorption energy. On the other hand, all AZT-supported catalysts exhibited lower NO_x storage efficiency than that of conventional Pt/20BaO/Al_2O_3 at high temperature range (*i.e.* 673K).

Identical set of flow-mode experiments were also performed under lean gas mixture of NO_2, O_2, CO_2, H_2O, Ar (FM^2) at 473, 573 and 673 K and corresponding results are illustrated in Figure 50b. In comparison to results obtained in lean mixture containing NO (g) (Figure 50a), NO_x storage quantities with NO_2(g)-containing lean mixture were found to be much higher. Although the formation of nitrates/nitrites during the reaction of NO + O_2 (FM^1) is not quite feasible at low temperatures (*i.e.* 473 K), it is highly favoured for NO_2 + O_2 feed (FM^2). Like in the case of FM^1 (Figure 50a), AZT-supported materials showed significantly superior performance

compared to the conventional Pt/20BaO/Al_2O_3 catalyst at low and mild temperature range for FM^2 (Figure 50b). For instance, Pt/8BaO/AZT and Pt/20BaO/AZT have 26 and 11 % higher NSC as compared to conventional NSR catalyst at low temperatures; respectively. On the other hand, Pt/20BaO/AZT was found to have the highest NO_x storage ability amoung all of the investigated materials at 573 K. However, NO_x trapping ability of AZT-supported materials are drastically suppressed and remain lower than conventional NSR at 673 K. The highest efficiency of conventional Pt/20BaO/Al_2O_3 catalyst towards NO_x storage can be indirectly correlated by highest surface basicity.

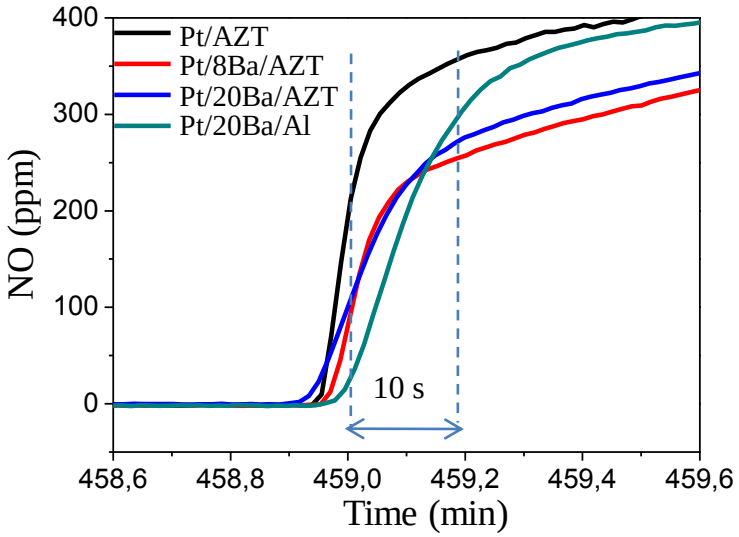

Figure 51: Initial NO_x adsorption rates for each catalyst at 573K in FM^1 mixture. This Figure was derived from the Figure 49a and also valid for all other temperatures and feed mixtures.

Figure 51 indicates an interesting kinetic phenomenon associated with the initial NO_x uptake rates of AZT-based materials versus conventional Pt/20BaO/Al catalyst. While the conventional catalyst has a higher (faster) NO_x storage characteristics in the first *ca.* 10 s, its storage rate rapidly decreases. On the other

hand, Pt/BaO/AZT catalyst reveal an initially slow NO_x uptake in the first 10 s, followed by a second sorption regime with a faster kinetics than that of Pt/20BaO/Al. This interesting discrepancy between the initial and later sorption kinetics of Pt/20BaO/Al and Pt/BaO/AZT may originate from differences in the initial NO/NO_2 oxidation over Pt sites. As reported in the previous sections, Pt is relatively poorly dispersed on Pt/BaO/AZT-based materials as compared to Pt/20BaO/Al; in accordance with greater Pt particle sizes estimated for the former system. Thus, it can be proposed that larger Pt particles on Pt/BaO/AZT lead to slow NO/NO_2 oxidation kinetics followed by the efficient (*i.e.* fast) nitrate spilover on BaO storage sites located on AZT support.

These results can lead us to conclude that AZT-supported materials can be considered as a promising candidate due to their significant NO_x trapping ability at low and mild temperatures (*i.e.* 473-573 K). However, NSC at high temperature (i.e. 673 K) was found lower than that of conventional catalyst. Therefore, activity loss at high temperature ranges were enhanced by incorporating the high temperature storage component (*i.e.* K_2O) and Pt/5.4K_2O/AZT was found to have much higher NSC at high temperature (*i.e.* 673 K) as compared to BaO-based materials together with the higher sulfur regeneration performance than that of benchmark Pt/20BaO/Al_2O_3 catalyst. Finally, optimum formulation was finalized *via* physical mixture of Pt/8BaO/AZT and Pt/5.4K_2O/AZT, indicating much higher NSC values at low and moderate temperature as compared to those of individuals.

Overall assessment regarding the sulfur adsorption and regeneration performance of AZT supported materials can be summarized as a proof of principle in scheme 8:

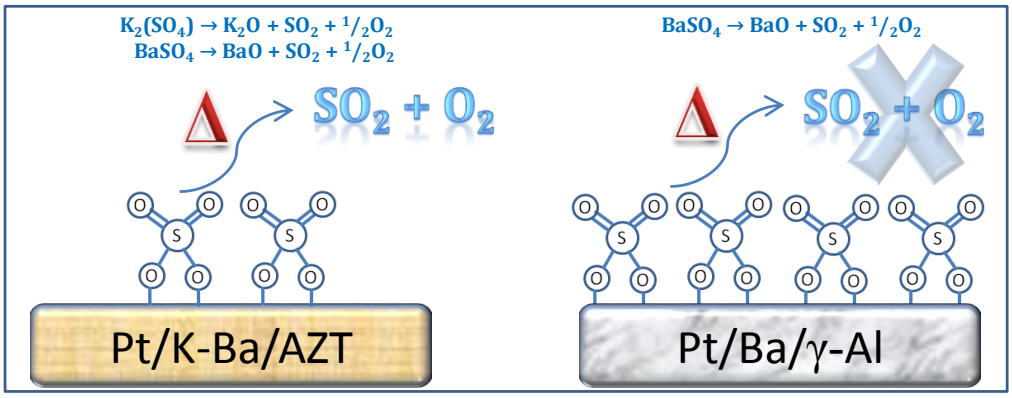

Scheme 8: Schematic illustration of sulfur adsorption desorption performance of AZT and γ-Al_2O_3 supported materials.

We can fine tune the surface characteristics of AZT-based materials via incorporating optimum loading of storage components (i.e. BaO and/or K_2O) which can exhibit superiour NSC performance and resistance against sulfur poisoning in comparison to γ-Al_2O_3 based conventional catalyst. These AZT supported materials can be considered as a promising candidate for next generation catalytic converters in exhaust pipeline. Moreover, structural integrity and resilience against thermal sintering were directly reported via benchtop structure characterization techniques.

Chapter 5

Conclusion

Experimental findings presented in the current work point to the fact that Pt/8BaO/AZT and Pt/5.4K_2O/AZT materials can be considered as two different promising candidates with higher NSC and better sulfur regeneration ability in comparison to γ-Al_2O_3-based conventional Pt/20Ba/Al NSR catalyst. Moreover, strong resistance against thermal sintering and higher surface acidities of AZT-based materials were thoroughly demonstrated. Binary and ternary oxide materials, ZrO_2/TiO_2 (ZT) and Al_2O_3/ZrO_2/TiO_2 (AZT),as well as their Pt-functionalized counterparts were synthesized by the sol-gel method. In addition to these materials, their BaO and K_2O-modified counterparts were also synthesized *via* impregnation method in the form of Pt/8BaO/AZT, Pt/20BaO/AZT, Pt/2.7K_2O/AZT, Pt/5.4K_2O/AZT and Pt/10K_2O/AZT, in comparison to Pt/20BaO/Al conventional NSR catalyst. Each material is structurally characterized by means of XRD, Raman spectroscopy and BET techniques.

NO_x adsorption capabilities as well as NOx adsorption geometries were investigated by means of in-*situ* FTIR spectroscopy. These adsorption experiments were subsequently followed by the reduction of adsorbed NO_x species where behavior of surface nitrate functional groups upon H_2(g) interaction was monitored*via* in-*situ* FTIR and TPD analysis in comparison to benchmark Pt/BaO/Al_2O_3.

In addition to NO_x adsorption/desorption experiments, *in-situ* FTIR spectroscopy and TPD technique were also applied for the analysis of the interaction between SO_2(g) and synthesized materials. Investigation of SO_xadsorption geometries as a function of temperature and their stabilities under H_2(g) and vacuum conditions were monitored.

Moreover, NO_x storage capabilities of synthesized materials were quantitatively determined under flow reactor measurements within a catalytically relevant temperature window.NSC of these catalysts was also measured under realistic flow reactor measurements after sulfur poisoning and subsequent regeneration.Main conclusions regarding structural characterization and molecular level spectroscopic investigations can be summarized as follows:

- In the ZT binary oxide system, a strong interaction between TiO_2 and ZrO_2 domains were observed at high temperatures (>973 K), which resulted in the formation of a highly ordered crystalline $ZrTiO_4$ phase and a low specific surface area (i.e. 26 m^2/g at 973 K).
- Incorporation of Al_2O_3 in the AZT structure renders the material highly resilient towards crystallization and ordering where AZT material was found to be amorphous even at 1173 K. Moreover, alumina acts as a diffusion barrier in the AZT structure, preventing the formation of $ZrTiO_4$ and leading to a very high specific surface area (i.e. 264 m^2/g at 973 K).
- NO_x adsorption capability of the AZT ternary oxide system was found to be significantly greater than that of ZT, in line with the almost ten-fold greater SSA of the former surface.

- Interaction of NO_2(g) with ZT and AZT surfaces revealed adsorbed surface nitrate species with similar geometries. While Pt incorporation did not alter the type of the adsorbed surface nitrate species, it significantly boosted the NO_x adsorption amount on both Pt/ZT and Pt/AZT systems.
- Thermal stability of nitrates was higher on the AZT compared to ZT, most likely due to the defective structure and the presence of coordinatively unsaturated sites on the former surface.
- Pt sites were found to assist the partial ordering/crystallization of the AZT system. Pt sites were also observed to facilitate the decomposition of nitrates in the absence of an external reducing agent by shifting the decomposition temperatures to lower values and by boosting the formation of N_2 and N_2O.
- In the presence of H_2(g), the complete reduction of surface nitrates was achieved at 623 K on ZT, while this was achieved at 723 K for AZT.
- Nitrate reduction over Pt/ZT and Pt/AZT *via* H_2(g) under mild conditions initially leads to the conversion of bridging nitrates into monodentate nitrates and nitrites together with the formation of surface –OH and $–NH_x$ functionalities. N_2O(g) was also observed in the very early stages of the reduction process as an initial intermediate/byproduct.
- NO_2(g) adsorption revealed the formation of bridging, bidentate and monodentate type of surface nitrates on Pt/AZT catalyst. However,

BaO-including NSR catalysts exhibited formation of bulk/ionic like nitrates on BaO domains in addition to surface nitrates.

- Increase in BaO loading leads to increase in the formation of bulk-like nitrates.
- Pt/20BaO/AZT and Pt/20BaO/Al_2O_3 has almost identical surface characteristics towards NO_2(g) interaction which are different than those of Pt/AZT and Pt/8BaO/AZT.
- Nitrate reduction pathways of both Pt/20BaO/AZT and Pt/20BaO/Al_2O_3 exhibited similar characteristics where the removal of surface nitrates are followed by the formation of bulk/ionic like nitrates together with the formation of surface -OH and NH_x groups.
- However, bulk/ionic like nitrates are not formed in the course of nitrate reduction on Pt/8BaO/AZT material together with the absence of –OH generation.
- Formation of bulk/ionic nitrates upon H_2(g) reduction can be correlated with the generation of surface –OH functionalities.
- Complete reduction was achieved at relatively lower temperature (*i.e.* 473K) on Pt/AZT as compared to those of BaO-containing NSR materials (*i.e.* 573K) in the presence of H_2(g).
- SSA-normalized total NO_x adsorption capabilities of investigated materials were found decrease in the following order: Pt/20BaO/AZT > Pt/8BaO/AZT > Pt/20BaO/Al_2O_3> Pt/AZT at 323K. It is apparent

that high BaO loadings favor higher NO_x adsorption capability on AZT-supported catalysts.

- Synthesized catalysts were quantitatively analyzed through flow reactor measurements at catalytically relevant temperatures (*i.e.* 473, 573 and 673K). These results regarding realistic flow mode experiments clearly point out that AZT-supported materials (*i.e.* Pt/8BaO/AZT and Pt/20BaO/AZT) exhibited relatively higher NO_x storage capacity at 473K and 573K under lean conditions as compared to that of benchmark conventional catalyst, $Pt/20BaO/Al_2O_3$. These findings are in very good agreement with the current TPD results.

- Unlike the conventional Pt/20BaO/Al benchmark catalyst, Pt/8BaO/AZT and Pt/20BaO/AZT catalysts revealed disordered structures lacking well-crystallized phases.

- Increasing the BaO loading in the Pt/BaO/AZT system increases the thermal stability of the generated bulk and surface sulfate/sulfite species after sulfur poisoning which in turn, leads to the requirement of higher reduction temperatures for complete sulfur elimination with $H_2(g)$.

- There seems to be a delicate trade-off between NO_x Storage Capacity (NSC) and sulfur uptake/poisoning which is strongly governed by the BaO loading/dispersion as well as the surface structure of the support material. It is apparent that although high BaO loadings favor higher NSC, they also render the NSR/LNT catalyst to be more prone

towards sulfur poisoning. Thus, by designing a catalyst with a proper support material (*e.g.* AZT) that is functionalized with intermediate BaO loadings (*i.e.* 8 wt. % BaO), a sulfur-tolerant NSR/LNT system with satisfactory NSC was achieved.

- Synthesized materials were further tested in flow reactor measurements performed under realistic catalytic conditions. Among all of the examined catalysts, Pt/8BaO/AZT showed a superior NSC at 573 K in its fresh form as well as after sulfur poisoning/subsequent sulfur regeneration, which surpassed the catalytic performances of all other investigated materials including the conventional Pt/20BaO/Al benchmark catalyst.

- Superior performance of Pt/8BaO/AZT catalyst can be associated in partto its high surface acidity among all other materials including the conventional Pt/20BaO/Al benchmark catalyst.

- While Pt/AZT, Pt/2.7K_2O/AZT and Pt/5.4K_2O/AZT revealed disordered structures except the presence of Pt diffraction line, Pt/10K_2O/AZT exhibited ordered domains corresponding to tetragonal ZrO_2 phases. On the other hand, unlike the AZT-supported materials, conventional Pt/20BaO/Al benchmark catalyst is composed of other phases such as γ-Al_2O_3 and undesired $BaAl_2O_4$.

- Increasing the K_2O loading in the Pt/K_2O/AZT system leads to an increase in the abundance of bulk-like sulfite functional groups which require higher temperature for complete sulfur elimination with H_2(g).

- The formation of K_2O-based bulk-like nitrate species becomes more dominant as the K_2O loading increases. Increase in K_2O loading concomitantly enhances NSC up to a certain value at the expense of decreasing sulfur resistance.

- The catalyst with a proper support and optimum K_2O loading, Pt/5.4K_2O/AZT, was found to have much better sulfur regeneration performance than the conventional Pt/20BaO/Al benchmark catalyst together with a satisfactory NSC.

- Like in the case of Pt/20BaO/AZT and Pt/20BaO/Al_2O_3, nitrate reduction pathways of both Pt/5.4K_2O/AZT and Pt/10K_2O/AZT exhibited similar characteristics where the removal of surface nitrates were followed by the formation of bulk/ionic like nitrates together with the formation of surface -OH and NH_x groups.However, the formation of bulk/ionic like nitrates was not observed during the reduction period of Pt/2.7K_2O/AZT material which can be correlated to the lack of –OH generation.

References

[1] F. Klingstedt, K. Arve, K. Eränen, and D. Y. Murzin, "Toward improved catalytic low-temperature NO_x removal in diesel-powered vehicles" *Acc. Chem. Res.*, vol. 39, pp. 273–282, 2006.

[2] L. E. Venegas, N. a Mazzeo, and A. L. P. Rojas, "Evaluation of an Emission Inventory and Air Pollution in the Metropolitan Area of Buenos Aires" *Air Qual. Appl.*, pp. 261–289, 2011.

[3] W. S. Epling, L. E. Campbell, a Yezerets, N. W. Currier, and J. E. Parks, "Overview of the fundamental reactions and degradation mechanisms of NO_x storage/reduction catalysts" *Catal. Rev. Eng.*, vol. 46, no. 2, pp. 163–245, 2004.

[4] S. Matsumoto, "Catalytic Reduction of Nitrogen Oxides in Automotive Exhaust Containing Excess Oxygen by NO_x Storage-Reduction Catalyst" *CATTECH*, vol. 4, no. 2, pp. 102–109, 2000.

[5] A. Fritz and V. Pitchon, "The current state of research on automotive lean NO_x catalysis" *Appl. Catal. B Environ.*, vol. 13, no. 1, pp. 1–25, 1997.

[6] P. Bielaczyc, J. Woodburn, and A. Szczotka, "An assessment of regulated emissions and CO_2 emissions from a European light-duty CNG-fueled vehicle in the context of Euro 6 emissions regulations" *Appl. Energy*, vol. 117, pp. 134–141, 2014.

[7] K. Kato, N. Nohira, K. Nakanishi, S. Iguchi, T. Kihara, and H. Muraki, *Euro Pat. Appl.*, vol. 0,573,672, 1993.

[8] N. Myioshi, S. Matsumoto, K. Katoh, T. Tanaka, K. Harada, N. Takahashi, K. Yokota, M. Sugiura, and K. Kasahara, *SAE Tech. Pap. Ser.*, vol. No: 950809, 1995.

[9] S. Roy and A. Baiker, "NO_x Storage - Reduction Catalysis: From Mechanism and Materials Properties to Storage - Reduction Performance" vol. 109, pp. 4054–4091, 2008.

[10] W. Epling, I. Nova, J. Szanyi, and A. Yezerets, "Diesel emissions control catalysis" *Catal. Today*, vol. 151, no. 3–4, p. 201, 2010.

[11] V. Medhekar, V. Balakotaiah, and M. Harold, "TAP study of NOx storage and reduction on Pt/Al_2O_3 and $Pt/Ba/Al_2O_3$" *Catal. Today*, vol. 121, no. 3–4, pp. 226–236, 2007.

[12] L. Olsson, B. Westerberg, H. Persson, E. Fridell, M. Skoglundh, and B. Andersson, "A Kinetic Study of Oxygen Adsorption/Desorption and NO

Oxidation over Pt/Al_2O_3 Catalysts" *J. Phys. Chem. B*, vol. 103, pp. 10433–10439, 1999.

[13] P. J. Schmitz and R. J. Baird, "NO and NO_2 adsorption on barium oxide: Model study of the trapping stage of NO_x conversion via lean NO_x traps" *J. Phys. Chem. B*, vol. 106, no. 2, pp. 4172–4180, 2002.

[14] P. Forzatti, L. Castoldi, I. Nova, L. Lietti, and E. Tronconi, "NO_x removal catalysis under lean conditions" *Catal. Today*, vol. 117, no. 1–3, pp. 316–320, 2006.

[15] I. Nova, L. Castoldi, L. Lietti, E. Tronconi, P. Forzatti, F. Prinetto, and G. Ghiotti, "NO_x adsorption study over Pt-Ba/alumina catalysts: FT-IR and pulse experiments" *J. Catal.*, vol. 222, no. 2, pp. 377–388, 2004.

[16] H. Abdulhamid, E. Fridell, and M. Skoglundh, "Influence of the type of reducing agent (H_2, CO, C_3H_6 and C_3H_8) on the reduction of stored NO_x in a Pt/BaO/Al_2O_3 model catalyst" *Top. Catal.*, vol. 30/31, pp. 161–168, 2004.

[17] T. Szailer, J. H. Kwak, D. H. Kim, J. Szanyi, C. Wang, and C. H. F. Peden, "Effects of Ba loading and calcination temperature on $BaAl_2O_4$ formation for BaO/Al_2O_3 NO_x storage and reduction catalysts" *Catal. Today*, vol. 114, no. 1, pp. 86–93, 2006.

[18] L. Lietti, "NO_x Storage Reduction over Pt-Ba/γ-Al_2O_3 Catalyst" *J. Catal.*, vol. 204, no. 1, pp. 175–191, 2001.

[19] M. Piacentini, M. Maciejewski, and A. Baiker, "Pt-Ba/alumina NO_x storage-reduction catalysts: Influence of Ba loading on NO_x storage behavior" *Appl. Catal. B Environ.*, vol. 60, no. 3–4, pp. 265–275, 2005.

[20] W. S. Epling, D. Kisinger, and C. Everest, "NO_x storage/reduction catalyst performance with oxygen in the regeneration phase" *Catal. Today*, vol. 136, no. 1–2, pp. 156–163, 2008.

[21] D. H. Kim, Y. Chin, G. G. Muntean, A. Yezeretz, N. W. Currier, W. S. Epling, H. Chen, H. Hess, and C. H. F. Peden, "Relationship of Pt Particle Size to the NO x Storage Performance of Thermally Aged Pt/BaO/Al_2O_3 Lean NO_x Trap Catalysts" *Ind. Eng. Chem. Res.*, vol. 45, pp. 8815–8821, 2006.

[22] S. M. Andonova, G. S. Şentürk, E. Kayhan, and E. Ozensoy, "Nature of the Ti−Ba Interactions on the BaO/TiO_2 /Al_2O_3 NO_x Storage System" *J. Phys. Chem. C*, vol. 113, no. 25, pp. 11014–11026, 2009.

[23] Z. Say, E. I. Vovk, V. I. Bukhtiyarov, and E. Ozensoy, "Influence of ceria on the NOx reduction performance of NO_x storage reduction catalysts" *Appl. Catal. B Environ.*, vol. 142–143, pp. 89–100, 2013.

[24] Z. Say, E. I. Vovk, V. I. Bukhtiyarov, and E. Ozensoy, "Enhanced sulfur tolerance of ceria-promoted NO_x storage reduction (NSR) catalysts: Sulfur uptake, thermal regeneration and reduction with H_2(g)" *Top. Catal.*, vol. 56, no. 11, pp. 950–957, 2013.

[25] T. Szailer, J. H. Kwak, D. H. Kim, J. C. Hanson, C. H. F. Peden, and J. Szanyi, "Reduction of stored NO_x on Pt/Al_2O_3 and $Pt/BaO/Al_2O_3$ catalysts with H_2 and CO" *J. Catal.*, vol. 239, no. 1, pp. 51–64, 2006.

[26] I. S. Pieta, M. García-Diéguez, C. Herrera, M. a. Larrubia, and L. J. Alemany, "In situ DRIFT-TRM study of simultaneous NO_x and soot removal over Pt-Ba and Pt-K NSR catalysts" *J. Catal.*, vol. 270, no. 2, pp. 256–267, 2010.

[27] K. S. Kabin, P. Khanna, R. L. Muncrief, V. Medhekar, and M. P. Harold, "Monolith and TAP reactor studies of NO_x storage on $Pt/BaO/Al_2O_3$: Elucidating the mechanistic pathways and roles of Pt" *Catal. Today*, vol. 114, no. 1, pp. 72–85, 2006.

[28] S. Morandi, F. Prinetto, G. Ghiotti, L. Castoldi, L. Lietti, P. Forzatti, M. Daturi, and V. Blasin-Aubé, "The influence of CO_2 and H_2O on the storage properties of $Pt\text{-}Ba/Al_2O_3$ LNT catalyst studied by FT-IR spectroscopy and transient microreactor experiments" *Catal. Today*, vol. 231, pp. 116-124, 2014.

[29] D. H. Kim, K. Mudiyanselage, J. Szányi, H. Zhu, J. H. Kwak, and C. H. F. Peden, "Characteristics of $Pt–K/MgAl_2O_4$ lean NO_x trap catalysts" *Catal. Today*, vol. 184, no. 1, pp. 2–7, 2012.

[30] M. Takeuchi and S. Matsumoto, "NO_x storage-reduction catalysts for gasoline engines" *Top. Catal.*, vol. 28, no. 1–4, pp. 151–156, 2004.

[31] T. J. Toops, D. B. Smith, and W. P. Partridge, "NO_x adsorption on $Pt/K/Al_2O_3$" *Catal. Today*, vol. 114, pp. 112–124, 2006.

[32] J. Luo, F. Gao, D. H. Kim, and C. H. F. Peden, "Effects of potassium loading and thermal aging on $K/Pt/Al_2O_3$ high-temperature lean NO_x trap catalysts" *Catal. Today*, vol. 231, pp. 164–172, 2014.

[33] T. Lesage, J. Saussey, S. Malo, M. Hervieu, C. Hedouin, G. Blanchard, and M. Daturi, "Operando FTIR study of NO_x storage over a $Pt/K/Mn/Al_2O_3\text{-}CeO_2$ catalyst" *Appl. Catal. B Environ.*, vol. 72, no. 1–2, pp. 166–177, 2007.

[34] C. Verrier, J. H. Kwak, D. H. Kim, C. H. F. Peden, and J. Szanyi, "NO_x uptake on alkaline earth oxides (BaO, MgO, CaO and SrO) supported on γ-Al_2O_3" *Catal. Today*, vol. 136, no. 1–2, pp. 121–127, 2008.

[35] A. Yoshida, W. Shen, T. Eda, R. Watanabe, T. Ito, and S. Naito, "NO_x storage/reduction over alkali-metal-nitrate impregnated titanate nanobelt

catalysts and investigation of alkali metal cation migration using XPS" *Catal. Today*, vol. 184, no. 1, pp. 78–82, 2012.

[36] A. L. Kustov and M. Makkee, "Application of NO_x storage/release materials based on alkali-earth oxides supported on Al_2O_3 for high-temperature diesel soot oxidation" *Appl. Catal. B Environ.*, vol. 88, no. 3–4, pp. 263–271, 2009.

[37] A. Hellman and H. Grönbeck, "First-Principles Studies of NO_x Chemistry on Ag/γ-Al_2O_3" *J. Phys. Chem. C*, vol. 113, pp. 3674–3682, 2009.

[38] T. Tanaka, C. Ando, T. Hamaguchi, and Y. Ikuta, "Improved low temperature removal of NO_x from lean-burn exhaust via adsorption on TiO_2-modified Ag-alumina" *Appl. Catal. A Gen.*, vol. 464–465, pp. 296–304, 2013.

[39] S. Tamm, S. Andonova, and L. Olsson, "Silver as storage compound for NO_x at low temperatures" *Catal. Letters*, vol. 144, pp. 674–684, 2014.

[40] S. Tamm, S. Andonova, and L. Olsson, "The Effect of Hydrogen on the Storage of NO_x Over Silver, Platinum and Barium Containing NSR Catalysts" *Catal. Letters*, vol. 144, pp. 1101–1112, 2014.

[41] M. Machida, S. Ikeda, D. Kurogi, and T. Kijima, "Low temperature catalytic NO_x - H_2 reactions over Pt/TiO_2-ZrO_2 in an excess oxygen" *Appl. Catal. B Environ.*, vol. 35, no. 2, pp. 107–116, 2001.

[42] H. Abdulhamid, E. Fridell, and M. Skoglundh, "The reduction phase in NO_x storage catalysis: Effect of type of precious metal and reducing agent" *Appl. Catal. B Environ.*, vol. 62, no. 3–4, pp. 319–328, 2006.

[43] S. Andonova, V. Marchionni, M. Borelli, R. Nedyalkova, L. Lietti, and L. Olsson, "Mechanistic investigations of the promoting role of Rh on the NSR performance of NO_x storage BaO-based catalysts" *Appl. Catal. B Environ.*, vol. 132–133, pp. 266–281, 2013.

[44] S. Salasc, M. Skoglundh, and E. Fridell, "A comparison between Pt and Pd in NO_x storage catalysts" *Appl. Catal. B Environ.*, vol. 36, no. 2, pp. 145–160, 2002.

[45] Y. Su, K. S. Kabin, M. P. Harold, and M. D. Amiridis, "Reactor and in situ FTIR studies of Pt/BaO/Al_2O_3 and Pd/BaO/Al_2O_3 NO_x storage and reduction (NSR) catalysts" *Appl. Catal. B Environ.*, vol. 71, no. 3–4, pp. 207–215, 2007.

[46] T. Lesage, C. Verrier, P. Bazin, J. Saussey, S. Malo, C. Hedouin, G. Blanchard, and M. Daturi, "Comparison Between a Pt–Rh/Ba/Al_2O_3 and a Newly Formulated NO_x -Trap Catalysts Under Alternate Lean–Rich Flows" *Top. Catal.*, vol. 30/31, no. 1–4, pp. 31–36, 2004.

[47] A. Amberntsson, E. Fridell, and M. Skoglundh, "Influence of platinum and rhodium composition on the NO_x storage and sulphur tolerance of a barium

based NO_x storage catalyst" *Appl. Catal. B Environ.*, vol. 46, no. 3, pp. 429–439, 2003.

[48] J. P. Breen, R. Burch, C. Fontaine-Gautrelet, C. Hardacre, and C. Rioche, "Insight into the key aspects of the regeneration process in the NO_x storage reduction (NSR) reaction probed using fast transient kinetics coupled with isotopically labelled ^{15}NO over Pt and Rh-containing Ba/Al_2O_3 catalysts" *Appl. Catal. B Environ.*, vol. 81, no. 1–2, pp. 150–159, 2008.

[49] X. Auvray and L. Olsson, "Stability and activity of Pd-, Pt- and Pd–Pt catalysts supported on alumina for NO oxidation" *Appl. Catal. B Environ.*, vol. 168–169, pp. 342–352, 2015.

[50] M. Casapu, J. D. Grunwaldt, M. Maciejewski, M. Wittrock, U. Göbel, and A. Baiker, "Formation and stability of barium aluminate and cerate in NO_x storage-reduction catalysts" *Appl. Catal. B Environ.*, vol. 63, no. 3–4, pp. 232–242, 2006.

[51] D. H. Kim, Y. H. Chin, J. H. Kwak, J. Szanyi, and C. H. F. Peden, "Changes in Ba phases in BaO/Al_2O_3 upon thermal aging and H_2O treatment" *Catal. Letters*, vol. 105, no. 3–4, pp. 259–268, 2005.

[52] C. Sedlmair, K. Seshan, A. Jentys, and J. . Lercher, "Studies on the deactivation of NO_x storage-reduction catalysts by sulfur dioxide" *Catal. Today*, vol. 75, no. 1–4, pp. 413–419, 2002.

[53] G. S. Şentürk, E. I. Vovk, V. I. Zaikovskii, Z. Say, A. M. Soylu, V. I. Bukhtiyarov, and E. Ozensoy, "SO_x uptake and release properties of TiO_2/Al_2O_3 and $BaO/TiO_2/Al_2O_3$ mixed oxide systems as NO_x storage materials" *Catalysis Today*, vol. 184, no. 1. pp. 54–71, 2012.

[54] P. Engström, A. Amberntsson, M. Skoglundh, E. Fridell, and G. Smedler, "Sulphur dioxide interaction with NO_x storage catalysts" *Appl. Catal. B Environ.*, vol. 22, pp. 241–248, 1999.

[55] S. Elbouazzaoui, E. C. Corbos, X. Courtois, P. Marecot, and D. Duprez, "A study of the deactivation by sulfur and regeneration of a model NSR $Pt/Ba/Al_2O_3$ catalyst" *Appl. Catal. B Environ.*, vol. 61, no. 3–4, pp. 236–243, 2005.

[56] C. Courson, a. Khalfi, H. Mahzoul, S. Hodjati, N. Moral, a. Kiennemann, and P. Gilot, "Experimental study of the SO_2 removal over a NO_x trap catalyst," *Catal. Commun.*, vol. 3, no. 10, pp. 471–477, 2002.

[57] S. Poulston and R. R. Rajaram, "Regeneration of NO_x trap catalysts" *Catal. Today*, vol. 81, no. 4, pp. 603–610, 2003.

[58] Z. Liu and J. a. Anderson, “Influence of reductant on the regeneration of SO_2-poisoned Pt/Ba/Al_2O_3 NO_x storage and reduction catalyst” *J. Catal.*, vol. 228, no. 1, pp. 243–253, 2004.

[59] Y. Liu, M. Meng, Z. Q. Zou, X. G. Li, and Y. Q. Zha, “In situ DRIFTS investigation on the NOx storage mechanisms over Pt/K/TiO_2-ZrO_2 catalyst” *Catal. Commun.*, vol. 10, no. 2, pp. 173–177, 2008.

[60] Y. Liu, M. Meng, X. G. Li, L. H. Guo, and Y. Q. Zha, “NO_x storage behavior and sulfur-resisting performance of the third-generation NSR catalysts Pt/K/TiO_2-ZrO_2” *Chem. Eng. Res. Des.*, vol. 86, no. 8, pp. 932–940, 2008.

[61] N. Takahashi, A. Suda, I. Hachisuka, M. Sugiura, H. Sobukawa, and H. Shinjoh, “Sulfur durability of NO_x storage and reduction catalyst with supports of TiO2, ZrO_2 and ZrO_2-TiO_2 mixed oxides” *Appl. Catal. B Environ.*, vol. 72, no. 1–2, pp. 187–195, 2007.

[62] Z. Q. Zou, M. Meng, N. Tsubaki, J. J. He, G. Wang, X. G. Li, and X. Y. Zhou, “Influence of Co or Ce addition on the NOx storage and sulfur-resistance performance of the lean-burn NO_x trap catalyst Pt/K/TiO_2-ZrO_2” *J. Hazard. Mater.*, vol. 170, no. 1, pp. 118–126, 2009.

[63] E. Kayhan, S. M. Andonova, G. S. Senturk, C. C. Chusuei, and E. Ozensoy, “Fe Promoted NO_x Storage Materials : Structural Properties and NO_x Uptake” *J. Phys. Chem. C*, vol. 114, pp. 357–369, 2010.

[64] S. M. Andonova, G. S. Şentürk, and E. Ozensoy, “Fine-tuning the dispersion and the mobility of BaO domains on NO_x storage materials via TiO_2 anchoring sites” *J. Phys. Chem. C*, vol. 114, no. 40, pp. 17003–17016, 2010.

[65] E. Emmez, E. I. Vovk, V. I. Bukhtiyarov, and E. Ozensoy, “Direct evidence for the instability and deactivation of mixed-oxide systems: Influence of surface segregation and subsurface diffusion” *J. Phys. Chem. C*, vol. 115, no. 45, pp. 22438–22443, 2011.

[66] R. Hummatov, O. Gülseren, E. Ozensoy, D. Toffoli, and H. Üstünel, “First-principles investigation of NO_x and SO_x adsorption on anatase-supported BaO and Pt overlayers” *J. Phys. Chem. C*, vol. 116, no. 10, pp. 6191–6199, 2012.

[67] Z. Say, M. Tohumeken, and E. Ozensoy, “NO_x storage and reduction pathways on zirconia and titania functionalized binary and ternary oxides as NO_x storage and reduction (NSR) systems” *Catal. Today*, vol. 231, pp. 135–144, 2014.

[68] S. Matsumoto, Y. Ikeda, H. Suzuki, M. Ogai, and N. Miyoshi, “NO_x storage-reduction catalyst for automotive exhaust with improved tolerance against sulfur poisoning” *Appl. Catal. B Environ.*, vol. 25, no. 2–3, pp. 115–124, 2000.

[69] K. I. Hadjiivanov and D. G. Klissurski, “Surface chemistry of titania (anatase) and titania-supported catalysts” *Chem. Soc. Rev.*, vol. 25, no. 1, p. 61, 1996.

[70] H. Y. Huang, R. Q. Long, and R. T. Yang, “A highly sulfur resistant Pt-Rh/TiO_2/Al_2O_3 storage catalyst for NO_x reduction under lean-rich cycles” *Appl. Catal. B Environ.*, vol. 33, no. 2, pp. 127–136, 2001.

[71] K. Ito, S. Kakino, K. Ikeue, and M. Machida, “NO adsorption/desorption property of TiO_2-ZrO_2 having tolerance to SO_2 poisoning” *Appl. Catal. B Environ.*, vol. 74, no. 1–2, pp. 137–143, 2007.

[72] T. Kanazawa, “Development of hydrocarbon adsorbents, oxygen storage materials for three-way catalysts and NO_x storage-reduction catalyst” *Catal. Today*, vol. 96, no. 3, pp. 171–177, 2004.

[73] B. M. Reddy and A. Khan, “Recent Advances on TiO_2-ZrO_2 Mixed Oxides as Catalysts and Catalyst Supports” *Catal. Rev. Eng.*, vol. 47, no. 2, pp. 257–296, 2005.

[74] K. Arata, S. Akutagawa, and K. Tanabe, “Isomerization of 1-Methylcyclohexene Oxide over TiO_2-ZrO_2, $NiSO_4$ and $FeSO_4$” *Bull. Chem. Soc. Jpn.*, vol. 79, no. 2, pp. 390–393, 1976.

[75] I. Wang, “Nonoxidative dehydrogenation of ethylbenzene over TiO_2/ZrO_2 catalysts I. Effect of composition on surface properties and catalytic activities” *J. Catal.*, vol. 83, no. 2, pp. 428–436, 1983.

[76] T. Yamaguchi, “Application of ZrO_2 as a catalyst and a catalyst support” *Catal. Today*, vol. 20, no. 2, pp. 199–217, 1994.

[77] H. Imagawa, T. Tanaka, N. Takahashi, S. Matsunaga, A. Suda, and H. Shinjoh, “Synthesis and characterization of Al_2O_3 and ZrO_2-TiO_2 nano-composite as a support for NO_x storage-reduction catalyst” *J. Catal.*, vol. 251, no. 2, pp. 315–320, 2007.

[78] H. Imagawa, N. Takahashi, T. Tanaka, S. Matsunaga, and H. Shinjoh, “Improved NOx storage-reduction catalysts using Al_2O_3 and ZrO_2-TiO_2 nanocomposite support for thermal stability and sulfur durability” *Appl. Catal. B Environ.*, vol. 92, no. 1–2, pp. 23–29, 2009.

[79] H. Imagawa, T. Tanaka, N. Takahashi, S. Matsunaga, A. Suda, and H. Shinjoh, “Titanium-doped nanocomposite of Al_2O_3 and ZrO_2-TiO_2 as a support with high sulfur durability for NO_x storage-reduction catalyst” *Appl. Catal. B Environ.*, vol. 86, no. 1–2, pp. 63–68, 2009.

[80] N. Takahashi, A. Suda, I. Hachisuka, and M. Sugiura, “Sulfur durability of NO_x storage and reduction catalyst with” *Appl. Catal. B Environ.*, vol. 72, pp. 187–195, 2007.

[81] Z. Q. Zou, M. Meng, X. Y. Zhou, X. G. Li, and Y. Q. Zha, "The effect of Al_2O_3 doping into TiO_2-ZrO_2on the storage and sulfur-resistance performance of the NO_x trap catalyst Pt/K/TiO_2-ZrO_2" *Catal. Letters*, vol. 128, no. 3–4, pp. 475–482, 2009.

[82] X. Chen and S. S. Mao, "Titanium dioxide nanomaterials: Synthesis, properties, modifications and applications" *Chem. Rev.*, vol. 107, no. 7, pp. 2891–2959, 2007.

[83] K. M. Glassford and J. R. Chelikowsky, "Structural and electronic properties of titanium dioxide" *Phys. Rev. B*, vol. 46, no. 3, pp. 1284–1298, 1992.

[84] A. G. Evans and R. M. Cannon, "Toughening of brittle solids by martensitic transformations" *Acta Metall.*, vol. 34, no. 5, pp. 761–800, 1986.

[85] A. Earhshaw and N. Greenwood, *Chemistry of the Elements*. Elsevier, 1997.

[86] J. P. Chang, Y.-S. Lin, and K. Chu, "Rapid thermal chemical vapor deposition of zirconium oxide for metal-oxide-semiconductor field effect transistor application" *J. Vac. Sci. Technol. B Microelectron. Nanom. Struct.*, vol. 19, no. 5, p. 1782, 2001.

[87] J. Burdett, G. Price, and S. Price, "Role of the Crystal-Field Theory in Determining the Structures of Spinels" *J. Am. Chem. Soc.*, vol. 104, pp. 92–95, 1982.

[88] C. C. Addison and N. Logan, "Anhydrous Metal Nitrates" *Adv. Inorg. Chem. Radiochem.*, vol. 6, pp. 71–142, 1964.

[89] A. Davydov, *Molecular Spectroscopy of Oxide Catalyst Surfaces*. 2003.

[90] E. Kayhan, "Structure and NO_x Uptake Properties of Fe-Ba/Al_2O_3 as a Model NOx Storage Material" Bilkent University, 2009.

[91] J. W. Niemantsverdriet, *Spectroscopy in Catalysis: An Introduction: Third Edition*. 2007.

[92] M. A. Krebs and R. A. Condrate, "A Raman spectral characterization of various crystalline mixtures in the ZrO_2-TiO_2 and HfO_2-TiO_2 systems" *J. Mater. Sci. Lett.*, vol. 7, pp. 1327–1330, 1988.

[93] F. Azough, R. Freer, and J. Petselt, "A Raman spectral characterization of ceramics in the system ZrO_2-TiO_2" *J. Mater. Sci.*, vol. 28, pp. 2273–2276, 1993.

[94] C. A. Uln, J. A. De Los Reyes, J. Escobar, M. C. Barrera, and M. A. Corts-Jacome, "Mesoporous (ZrO_2/TiO_2)/Al_2O_3 ternary carriers as hydrodesulfurization catalysts support" *J. Phys. Chem. Solids*, vol. 71, no. 7, pp. 1004–1012, 2010.

[95] K. Hadjiivanov, V. Bushev, M. Kantcheva, and D. Klissurski, “Infrared spectroscopy study of the species arising during nitrogen dioxide adsorption on titania (anatase)” *Langmuir*, vol. 10, no. 2, pp. 464–471, 1994.

[96] M. Kantcheva, “FT-IR spectroscopic investigation of the reactivity of NO_x species adsorbed on Cu^{2+}/ZrO_2 and $CuSO_4/ZrO_2$ catalysts toward decane” *Appl. Catal.*, vol. 42, pp. 89–109, 2003

[97] M. Kantcheva and A. S. Vakkasoglu, “Cobalt supported on zirconia and sulfated zirconia I. FT-IR spectroscopic characterization of the NOx species formed upon NO adsorption and NO/O_2 coadsorption” *J. Catal.*, vol. 223, no. 2, pp. 352–363, 2004.

[98] M. Kantcheva, “Identification, Stability, and Reactivity of NO_x Species Adsorbed on Titania-Supported Manganese Catalysts” *J. Catal.*, vol. 204, no. 2, pp. 479–494, 2001.

[99] Z. Say, M. Dogac, E. I. Vovk, Y. E. Kalay, C. H. Kim, W. Li, and E. Ozensoy, “Palladium doped perovskite-based NO oxidation catalysts: The role of Pd and B-sites for NO_x adsorption behavior via in-situ spectroscopy” *Appl. Catal. B Environ.*, vol. 154–155, pp. 51–61, 2014.

[100] D. H. Kim, J. H. Kwak, J. Szanyi, S. D. Burton, and C. H. F. Peden, “Water-induced bulk $Ba(NO_3)_2$ formation from NO_2 exposed thermally aged BaO/Al_2O_3” *Appl. Catal. B Environ.*, vol. 72, no. 3–4, pp. 233–239, 2007.

[101] F. Prinetto, M. Manzoli, S. Morandi, F. Frola, G. Ghiotti, L. Castoldi, L. Lietti, and P. Forzatti, “P-K/Al_2O_3 NSR Catalysts : Characterization of Morphological , Structural and Surface Properties” no. 2, pp. 1127–1138, 2010.

[102] J. R. Theis and E. Gulari, “Estimating the temperatures of the NO_x storage sites in a lean NO_x trap during oxidation reactions” *Appl. Catal. B Environ.*, vol. 74, no. 1–2, pp. 40–52, 2007.

[103] L. Lietti, I. Nova, and P. Forzatti, “Role of ammonia in the reduction by hydrogen of NO_x stored over Pt-Ba/Al_2O_3 lean NO_x trap catalysts,” *J. Catal.*, vol. 257, no. 2, pp. 270–282, 2008.

[104] T. Montanari, L. Castoldi, L. Lietti, and G. Busca, “Basic catalysis and catalysis assisted by basicity: FT-IR and TPD characterization of potassium-doped alumina” *Appl. Catal. A Gen.*, vol. 400, no. 1–2, pp. 61–69, 2011.

[105] D. H. Kim, K. Mudiyanselage, J. Szanyi, J. C. Hanson, and C. H. F. Peden, “Effect of H_2O on the Morphological Changes of KNO_3 Formed on K_2O/Al_2O_3 NO_x Storage Materials: Fourier Transform Infrared and Time-Resolved X-ray Diffraction Studies” *J. Phys. Chem. C*, vol. 118, pp. 4189–4197, 2014.

[106] L. Righini, F. Gao, L. Lietti, J. Szanyi, and C. H. F. Peden, "Performance and properties of K and TiO_2 based LNT catalysts" *Appl. Catal. B Environ.*, vol. 181, pp. 862–873, 2015.

[107] D. H. Kim, K. Mudiyanselage, J. Szanyi, J. H. Kwak, H. Zhu, and C. H. F. Peden, "Effect of K loadings on nitrate formation/decomposition and on NO_x storage performance of K-based NO_x storage-reduction catalysts" *Appl. Catal. B Environ.*, vol. 142–143, pp. 472–478, 2013.

[108] L. Castoldi, L. Lietti, R. Bonzi, N. Artioli, P. Forzatti, S. Morandi, and G. Ghiotti, "The NO_x reduction by CO on a Pt-K/Al_2O_3 Lean NO_x trap catalyst" *J. Phys. Chem. C*, vol. 115, no. 4, pp. 1277–1286, 2011.

[109] J. Szanyi, J. H. Kwak, D. H. Kim, S. D. Burton, and C. H. F. Peden, "NO_2 adsorption on BaO/Al_2O_3: the nature of nitrate species" *J. Phys. Chem. B*, vol. 109, no. 1, pp. 27–29, 2005.

[110] B. Westerberg and E. Fridell, "A transient FTIR study of species formed during NO_x storage in the Pt/BaO/Al_2O_3 system," *J. Mol. Catal. A Chem.*, vol. 165, no. 1–2, pp. 249–263, 2001.

[111] L. Olsson, "The Influence of Pt Oxide Formation and Pt Dispersion on the Reactions $NO_2 \Leftrightarrow NO+1/2O_2$ over Pt/Al_2O_3 and Pt/BaO/Al_2O_3" *J. Catal.*, vol. 210, no. 2, pp. 340–353, 2002.

[112] C. M. L. Scholz, V. R. Gangwal, M. H. J. M. de Croon, and J. C. Schouten, "Influence of CO_2 and H_2O on NO_x storage and reduction on a Pt-Ba/γ-Al_2O_3 catalyst" *Appl. Catal. B Environ.*, vol. 71, pp. 143–150, 2007.

[113] L. Castoldi, L. Lietti, P. Forzatti, S. Morandi, G. Ghiotti, and F. Vindigni, "The NO_x storage-reduction on Pt/K/Al_2O_3 Lean NO_x Trap catalyst" *J. Catal.*, vol. 276, no. 2, pp. 335–350, 2010.

[114] M. Kantcheva and E. Z. Ciftlikli, "FTIR Spectroscopic Characterization of NO_x Species Adsorbed on ZrO_2 and ZrO_2 $-SO_4^{2-}$" *J. Phys. Chem. B*, vol. 106, no. 15, pp. 3941–3949, 2002.

[115] C. Chang, "Infrared studies of SO_2 on γ-Al_2O_3" *J. Catal.*, vol. 53, no. 3, pp. 374–385, 1978.

[116] M. Waqif, "Use of CeO_2-Al_2O_3 as a SO_2 sorbent" *Solid State Ionics*, vol. 95, no. 1–2, pp. 163–167, Feb. 1997.

[117] O. Saur, "The structure and stability of sulfated alumina and titania" *J. Catal.*, vol. 99, no. 1, pp. 104–110, 1986.

[118] H. Yao, "The effects of SO_2 on the oxidation of hydrocarbons and carbon monoxide over Pt/γ-Al_2O_3 catalysts" *J. Catal.*, vol. 67, no. 1, pp. 231–236, 1981.

[119] H. Abdulhamid, E. Fridell, J. Dawody, and M. Skoglundh, “In situ FTIR study of SO_2 interaction with $Pt/BaCO_3/Al_2O_3$ NO_x storage catalysts under lean and rich conditions” *J. Catal.*, vol. 241, no. 1, pp. 200–210, 2006.

[120] F. Hoffmann, “Infrared reflection-absorption spectroscopy of adsorbed molecules” *Surf. Sci. Rep.*, vol. 3, no. 2–3, p. 107, 1983.

[121] E. Ozensoy, C. Peden, and J. Szanyi, “Model NO_x storage systems: Storage capacity and thermal aging of $BaO/\theta\text{-}Al_2O_3/NiAl(100)$” *J. Catal.*, vol. 243, no. 1, pp. 149–157, 2006.

[122] M. May, J. Navarrete, M. Asomoza, and R. Gomez, “Tailored mesoporous alumina prepared from different aluminum alkoxide precursors” *J. Porous Mater.*, vol. 14, no. 2, pp. 159–164, 2007.

[123] J. a. Wang, X. Bokhimi, O. Novaro, T. Lopez, F. Tzompantzi, R. Gomez, J. Navarrete, and M. E. Llanos, “Effects of structural defects and acid – basic properties on the activity and selectivity of isopropanol decomposition on nanocrystallite sol-gel alumina catalyst” *J. Mol. Catal. A Chem.*, vol. 137, p. 239, 1999.

[124] J. Sa, X. Bokhimi, F. Herna, and I. Mexicano, “Physicochemical and Catalytic Properties of Sol-Gel Aluminas Aged under Hydrothermal Conditions” no. 25, pp. 3583–3588, 2003.

[125] A. Maijanen, E. G. Derouane, and J. B. Nagy, “FT-IR and solid-state NMR investigation of surface hydroxyl groups on dealuminated ZSM-5” *Appl. Surf. Sci.*, vol. 75, no. 1–4, pp. 204–212, Jan. 1994.

[126] S. Damyanova, P. Grange, and B. Delmon, “Surface characterization of zirconia-coated alumina and silica carriers” *J. Catal.*, vol. 168, no. 2, pp. 421–430, 1997.

[127] B. M. Reddy, G. K. Reddy, K. N. Rao, and L. Katta, “Influence of alumina and titania on the structure and catalytic properties of sulfated zirconia: Beckmann rearrangement” *J. Mol. Catal. A Chem.*, vol. 306, no. 1–2, pp. 62–68, 2009.

[128] R. Barthos, F. Lónyi, G. Onyestyák, and J. Valyon, “An NH_3-TPD and -FTIR study on the acidity of sulfated zirconia” *Solid State Ionics*, vol. 141–142, pp. 253–258, 2001.

[129] M. Łaniecki, M. Małecka-Grycz, and F. Domka, “Water–gas shift reaction over sulfided molybdenum catalysts” *Appl. Catal. A Gen.*, vol. 196, no. 2, pp. 293–303, 2000.

APPENDIX

Order Completed

Thank you very much for your order.

This is a License Agreement between Zafer Say ("You") and Springer ("Springer"). The license consists of your order details, the terms and conditions provided by Springer, and the payment terms and conditions.

Get the printable license.

License Number	3730160914424
License date	Oct 15, 2015
Licensed content publisher	Springer
Licensed content publication	CATTECH
Licensed content title	Catalytic Reduction of Nitrogen Oxides in Automotive Exhaust Containing Excess Oxygen by NOx Storage-Reduction Catalyst
Licensed content author	Shin'ichi Matsumoto
Licensed content date	Jan 1, 2000
Volume number	4
Issue number	2
Type of Use	Thesis/Dissertation
Portion	Figures/tables/illustrations
Number of figures/tables/illustrations	1
Author of this Springer article	No
Order reference number	4
Original figure numbers	Figure 1
Title of your thesis / dissertation	INVESTIGATION OF ADSORPTION/DESORPTION PROPERTIES OF NO2 AND SO2 MOLECULES
Expected completion date	Nov 2015
Estimated size(pages)	177
Customer VAT ID	TR25883061238
Total	0.00 USD

CLOSE WINDOW

Title: NOx storage and reduction pathways on zirconia and titania functionalized binary and ternary oxides as NOx storage and reduction (NSR) systems

Author: Zafer Say,Merve Tohumeken,Emrah Ozensoy

Publication: Catalysis Today

Publisher: Elsevier

Date: 1 August 2014

Order Completed

Thank you very much for your order.

This is a License Agreement between Zafer Say ("You") and Elsevier ("Elsevier"). The license consists of your order details, the terms and conditions provided by Elsevier, and the payment terms and conditions.

Get the printable license.

License Number	3730130600041
License date	Oct 15, 2015
Licensed content publisher	Elsevier
Licensed content publication	Catalysis Today
Licensed content title	NOx storage and reduction pathways on zirconia and titania functionalized binary and ternary oxides as NOx storage and reduction (NSR) systems
Licensed content author	Zafer Say,Merve Tohumeken,Emrah Ozensoy
Licensed content date	1 August 2014
Licensed content volume number	231
Licensed content issue number	n/a
Number of pages	10
Type of Use	reuse in a thesis/dissertation
Portion	figures/tables/illustrations
Number of figures/tables/illustrations	7
Format	both print and electronic
Are you the author of this Elsevier article?	Yes
Will you be translating?	No
Order reference number	67
Original figure numbers	6b, 7b, 10b, 11b, 15, 19, 20
Title of your thesis/dissertation	INVESTIGATION OF ADSORPTION/DESORPTION PROPERTIES OF NO2 AND SO2 MOLECULES

Expected completion date	Nov 2015
Estimated size (number of pages)	177
Elsevier VAT number	GB 494 6272 12
Customer Tax ID	TR25883061238
Permissions price	0.00 USD
VAT/Local Sales Tax	0.00 USD / 0.00 GBP
Total	0.00 USD

ORDER MORE... CLOSE WINDOW

Title: NOx removal catalysis under lean conditions
Author: P. Forzatti,L. Castoldi,I. Nova,L. Lietti,E. Tronconi
Publication: Catalysis Today
Publisher: Elsevier
Date: 30 September 2006

Order Completed

Thank you very much for your order.

This is a License Agreement between Zafer Say ("You") and Elsevier ("Elsevier"). The license consists of your order details, the terms and conditions provided by Elsevier, and the payment terms and conditions.

Get the printable license.

License Number	3730121199950
License date	Oct 15, 2015
Licensed content publisher	Elsevier
Licensed content publication	Catalysis Today
Licensed content title	NOx removal catalysis under lean conditions
Licensed content author	P. Forzatti,L. Castoldi,I. Nova,L. Lietti,E. Tronconi
Licensed content date	30 September 2006
Licensed content volume number	117
Licensed content issue number	1-3
Number of pages	5
Type of Use	reuse in a thesis/dissertation
Portion	figures/tables/illustrations
Number of figures/tables/illustrations	3
Format	both print and electronic
Are you the author of this Elsevier article?	No
Will you be translating?	No
Original figure numbers	Figure 3
Title of your thesis/dissertation	INVESTIGATION OF ADSORPTION/DESORPTION PROPERTIES OF NO2 AND SO2 MOLECULES
Expected completion date	Nov 2015
Estimated size (number of pages)	177
Elsevier VAT number	GB 494 6272 12
Customer Tax ID	TR25883061238
Permissions price	0.00 USD
VAT/Local Sales Tax	0.00 USD / 0.00 GBP
Total	0.00 USD

ORDER MORE... CLOSE WINDOW